Hauptreferent:
Prof. Dr.-Ing. U. Nackenhorst

Korreferent:
Prof. Dr.-Ing. Olivier Allix

Doktorand:
Dipl.-Ing. Milena Möhle

Numerical investigation on hydrogen embrittlement of metallic pipeline structures

Von der Fakultät für
Bauingenieurwesen
und Geodäsie der
Gottfried Wilhelm Leibniz
Universität Hannover

zur Erlangung des Grades
eines

Doktor-Ingenieurs

genehmigte Dissertation von

Dipl.-Ing. Milena Möhle

Hannover 2018

Tag der Einreichung:
10.01.2018
Tag der mündl. Prüfung:
16.04.2018

**Institut für
Baumechanik
und Numerische
Mechanik**

Herausgeber:
Prof. Dr.-Ing. U. Nackenhorst

Verwaltung:
Institut für Baumechanik
und Numerische Mechanik
Gottfried Wilhelm Leibniz
Universität Hannover
Appelstr. 9A
30167 Hannover
Tel.: +49 (0)511 / 762-3219
Fax.: +49 (0)511 / 762-19053

Institut für Baumechanik
und Numerische Mechanik
Gottfried Wilhelm Leibniz
Universität Hannover
Appelstr. 9A
30167 Hannover

ISBN 978-3-935732-48-2

Abstract

Motivated by shifting to renewable energy sources, the utilization of hydrogen gas as an energy carrier is discussed to account for expected irregularities in supply. Here, the construction of a new hydrogen pipeline network would be rather expensive such that the usage of the existing natural gas pipeline system is in the focus of investigation. One major problem is that hydrogen embrittles the material and can cause fatal failure especially in case of pipelines which were already damaged during their service time. At the localized stress fields around pre-existing cracks, hydrogen accumulates and converts the material response from ductile to brittle failure.

Based on experimental findings, the so-called Hydrogen Enhanced Localized Plasticity (HELP) mechanism is identified to govern hydrogen embrittlement in the prevalent case by reducing the yield stress in a continuum sense. To solve the highly coupled equations of the mechanical model and the transient hydrogen distribution model, an iterative finite element scheme is applied using a discontinuous Galerkin method for time discretisation. A continuum model of a natural gas pipeline with a radial crack is investigated. Therefore, a surrogate model using the boundary layer approach is adopted, whose results are in good agreement with a model of the full pipeline structure.

Based on the idea of the local softening effect by the HELP mechanism, three different approaches to account for hydrogen embrittlement are discussed. Firstly, the steady state hydrogen distributions in front of the crack tip are evaluated while in a next step the effect of hydrogen on the mechanical properties is discussed. When investigating the impact of different crack lengths, a notably increasing amount of hydrogen embrittlement is identified. The results highlight the importance of carefully investigating the actual conditions in the specific pipelines and adequately accounting for hydrogen embrittlement in numerical simulations as a basis for ducting hydrogen through the existing pipeline system.

Keywords: Hydrogen Embrittlement, Finite Element Method, Time Discontinuous Galerkin method, Hydrogen Enhanced Localized Plastecity (HELP) mechanism, Boundary Layer Approach, Natural Gas Pipeline System

Kurzfassung

Motiviert von der anstehenden Energiewende wird aktuell unter anderem diskutiert, ob Wasserstoffgas ein brauchbarer Energieträger ist, um erwartete Unregelmäßigkeiten in der Energieversorgung zu überbrücken. Da die Konstruktion eines neuen Rohrleitungssystems für Wasserstoff mit hohen Kosten verbunden wäre, wird untersucht, ob das existierende Erdgassystem für diese Zwecke verwendet werden kann. Hierbei erscheint besonders problematisch, dass Wasserstoffgas in das Rohrleitungsmaterial eindringen kann und dieses unter bestimmten Bedingungen versprödet. Dies kann zu fatalem Materialversagen führen, insbesondere bei bereits vorgeschädigten Rohrsegmenten. So sammelt sich an den lokalen Spannungsfeldern der Risse Wasserstoff an, der das Materialversagen von duktil zu spröde transformiert.
Basierend auf experimentellen Ergebnissen kann der so genannte Hydrogen Enhanced Localized Plasticity (HELP) Mechanismus im hier untersuchten Fall als vorherrschender Versprödungsmechanismus identifiziert und durch eine gezielte Reduktion der Fließgrenze im Rahmen des verwendeten Kontinuumsmodells berücksichtigt werden. Um das stark gekoppelte Gleichungssystem des mechanischen Modells und des transienten Wasserstoffmodells zu lösen, wird ein iterativer Finite-Element-Ansatz mit der diskontinuierlichen Galerkin Methode für die Zeitdiskretisierung genutzt.
Da insbesondere bereits beschädigte Rohre kritisch im Hinblick auf Versagen sind, wird ein Kontinuumsmodell einer Erdgasleitung mit einem radialen Riss untersucht. Hierfür kommt ein Ersatzmodel unter Berücksichtigung des "boundary layer approaches" zum Einsatz, dessen Ergebnisse gut mit denen einer Simulationen eines vollen Rohrausschnittes übereinstimmen.
Basierend auf der Idee des HELP Mechanismusses werden drei unterschiedliche Ansätze zur Berücksichtigung von Wasserstoffversprödung vorgestellt. Zunächst wird die stationäre Verteilung der Wasserstoffkonzentrationen bestimmt, woraufhin in einem weiteren Schritt der Einfluss von Wasserstoff auf die Materialeigenschaften mit einbezogen wird. Bei der numerischen Untersuchung des Einflusses verschiedener Risstiefen kann eine ansteigende Tendenz der Wasserstoffversprödung identifiziert werden. Diese Ergebnisse zeigen die Wichtigkeit einer eingehenden Untersuchung der existierenden Rohrstrukturen und die Notwendigkeit der Weiterentwicklung numerischer Methoden, um den Einfluss von Wasserstoffgas auf das Erdgassystem schlussendlich bewerten zu können.

Stichworte: Wasserstoffversprödung, Finite Elemente Methode, Zeit diskontinuierliche Galerkin Methode, Hydrogen Enhanced Localized Plastecity (HELP) Mechanismus, Boundary Layer Approach, Erdgassystem

Contents

1. Introduction

1.1. Motivation

Due to global warming and the short comings of fossil fuels, the interest in renewable energy sources consistently grew during the last decades. One of the major problems concerning most types of renewable energy sources, like for example wind turbines and solar collectors, is the fluctuation of the produced energy. To ensure a constant energy supply, the energy needs to be saved when produced in excess and returned to the system when production rates are low. To achieve this, one approach is to convert the excess energy to hydrogen gas [1].

Production methods to obtain hydrogen gas, end-user applications as well as storage technologies are well known in general. For commercial use however, these technologies need to be further developed [1]. An additional question is how the hydrogen gas can be distributed to the end-users. In Europe, a hydrogen gas network with a total pipelinie length of only $16,000\,km$ exists [2]. Compared to the natural gas pipeline system in Germany of about $505,000\,km$ the hydrogen gas pipeline network is rather small [3]. Due to its low strength steels, the operation pressure is limited and thus an effective transport for energy routing does not seem feasible [2]. The extension of this hydrogen pipeline system would be rather expensive. Furthermore, installing a new network next to the existing infrastructure would cause practical implementation space-related problems especially for end-user systems [1]. Thus, instead of constructing a new hydrogen gas pipeline system, more economic ideas are needed. While still under investigation, one of the most promising ones is to use the existing natural gas pipeline system to allocate the hydrogen gas (compare Figure 1.1).

As early as in the 1960s, hydrogen gas was already ducted through the nowadays natural gas pipeline system in form of the so called city gas, composed of about 50% carbon monoxide and 50% hydrogen gas [1]. However, this city gas composition was changed to natural gas in a rather rapid manner. As the network was subdivided into sectors, one sector after the other was changed to natural gas and end-user applications were replaced. Such a rapid procedure is not likely to happen again for replacing the natural gas with hydrogen due to numerous reasons [1]. Firstly, the pipeline network grew over the last decades to three times of its former length. Consequently, the number of end-users increased enormously such that the exchange of end-user applications nowadays would be costly as well as time consuming. In addition, problems could arise from pressure conversion. Here, compressors are used to reduce the high pressures of the transport grid to lower pressure levels in the local distribution network. As in the past no high pressure transport grids existed, the compatibility of the compressors with the hydrogen gas needs to be ensured.

Due to these developments in the last decades, it is more likely that a continuous transition from natural to hydrogen gas takes place. Therefore, in a first step, hydrogen will be mixed with the natural gas. No adjustments of the natural gas pipeline infrastructure need to be considered when adding up to $17\,vol.\%$ of hydrogen to the natural gas [1].

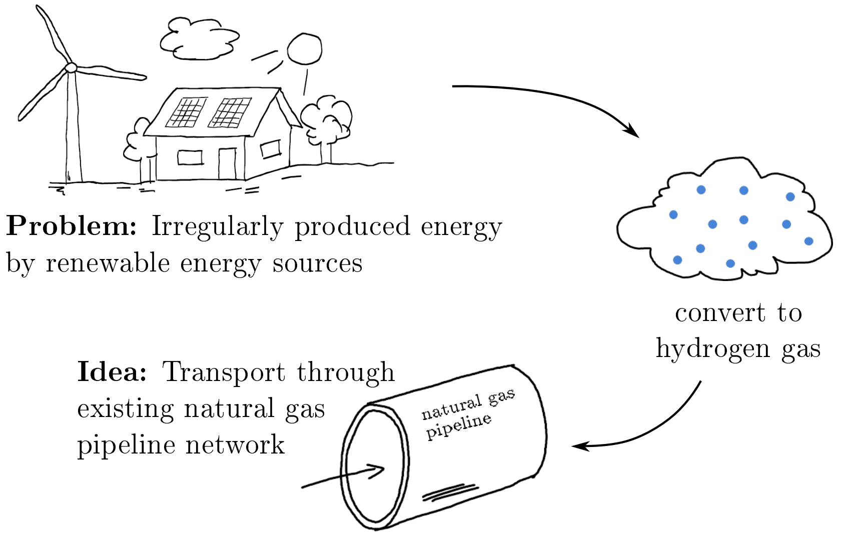

Figure 1.1.: Schematic representation of storing energy by injecting hydrogen gas into the existing gas pipeline system

Besides the bare technical supply, also the energy content of the gas and the leakage of the pipelines have to be discussed in case hydrogen gas is conducted through.

The main purpose of the natural gas pipeline system obviously is to transport gas. Hydrogen gas needs about the same pressure drop as natural gas to allow for effective transportation. Thus, no problems arise from the transportation point of view. The pipeline network is also used for short-time storage of the natural gas, which is called linepack energy. Unfortunately, the linepack energy for hydrogen is four times smaller compared to natural gas. Consequently, the provision of a sudden peak in energy demand might become critical when replacing natural gas completely with hydrogen [1]. This issue still needs to be resolved when a hydrogen based energy system is favoured.

Since the hydrogen molecules are smaller than those of natural gas, leakage could also potentially cause problems. The general leakage of hydrogen gas was determined to about 0.0005% to 0.001% of the total transported volume. Therefore, from a practical point of view, it can be judged as negligible [1].

Another major topic which needs to be addressed is the service security of the pipeline system. Hydrogen is well known to embrittle materials. Since the hydrogen atoms are comparatively small, they can enter the material lattice of the pipeline steel and change here the failure mode from ductile to brittle. Already small cracks or defects exposed to hydrogen can lead to a catastrophic event [2]. Here, especially tubes under high pressures are susceptible to hydrogen embrittlement.

A reduction of toughness due to hydrogen was already recognized in 1875 by Johnson [4]. This reversible process did not gain high attention until in World War II, the famous Liberty ships started to collapse without warning. Gerberich [5] claimed that many text books are incomplete by not mentioning the effect of hydrogen embrittlement on the ship trunks. The hydrogen, induced by welding and during the service time, caused the brittle crack growth in the ships according to a study of Zapffe and Sims [6]. Even though the hydrogen embrittlement phenomenon is known for a long time period, the actual underlying mechanism of hydrogen embrittlement is still discussed controversially.

Following the idea of replacing the natural by hydrogen gas, the process of hydrogen embrittlement consequently needs to be understood. Due to the fact that hydrogen gas would only be an economic alternative to natural gas if the hydrogen can be transported securely through the existing pipeline network. Therefore, the examination of hydrogen affecting the material properties is a major point of interest.
Within this thesis, the effect of hydrogen on the mechanical properties of the existing natural gas pipeline system is investigated numerically. To estimate the amount of hydrogen embrittlement, the hydrogen entering the material lattice needs to be quantified and its effect on the material properties calculated. As a first step, in the next chapter an overview of possible numerical procedures is given, followed by a presentation of the general structure of this work.

1.2. State of the art

The effect of hydrogen embrittlement gets most pronounced when high hydrogen concentrations are present, like at stress localizations inside the material. Thus, most numerical models in literature investigate hydrogen embrittlement at localized stress fields as in case of nanoindentation and crack tip studies.
In order to simulate the brittle effect of hydrogen on the material behaviour, several approaches are used in literature. In the following, the different realizations of hydrogen embrittlement based on an atomic model, a cohesive zone model combined with a continuum approach as well as a pure continuum model are summarized.
An atomic scale model considering molecular dynamic simulations was used to investigate the transition from ductile to brittle material behaviour in the presence of hydrogen by Wen et al. [7]. The authors put their focus on discussing changes in the dislocation behaviour in the presence of hydrogen. The numerical findings showed to be in good agreement with experimental ones obtained by Nibur et al. [8]. Nevertheless, simulations on atomic length scale are numerically rather expensive in case of large structures. Therefore, Song and Curtin [9] propose a combination of an atomic scale model in the vicinity of a crack tip and a continuum model in the far field including discrete dislocations. In this way, the brittle crack propagation in the presence of hydrogen was investigated and drawbacks of the underlying embrittlement mechanism were discussed.
Another possibility to address the topic of brittle crack propagation is a combination of a continuum model and a cohesive element layer [10, 11]. A crack is modelled with continuum elements and in front of the crack tip (in the uncracked region), a cohesive element layer with zero thickness is introduced. Here, a separation of the continuum elements is permitted which is governed by a separation law. This separation law was defined in dependency on the locally present hydrogen concentration. Doing so, the brittle crack propagation characteristic observed in experiments could be numerically reproduced. A drawback of this approach is that the crack path is artificially designed to a straight line, which does not reflect a realistic crack propagation path.
Using continuum modelling, good results could be obtained for cycling loading processes to capture the mechanical behaviour of the material in the presence of hydrogen by Bouajila et al. [12]. The fatigue loading cycles were cut into half in the presence of hydrogen, when considering high cycle fatigue loading conditions and a steady state hydrogen concentration. The authors assumed a steady state hydrogen concentration

inside the material since loading cycles are so fast that the hydrogen does not have enough time to redistribute inside the material within one loading cycle. Nevertheless, for low cycle fatigue, a transient hydrogen concentration needs to be considered and a dependency on the loading frequency on the amount of hydrogen embrittlement was determined by Kotake et al. [13]. When it comes to the existing pipeline system, pressure changes are rather small such that a cyclic loading process does not need to be considered.

However, in this study the effect of hydrogen on the material of a pipeline structure is investigated. Thus, the focus is to determine if the effect of hydrogen is critical on an existing pipeline structure and not to simulate the actual fracture process nor cyclic loading conditions. Therefore, a continuum model with a transient hydrogen concentration approach is favoured in this work.

The first proposed coupling of an elasto-plastic continuum model with a stress driven hydrogen distribution approach goes back to the work of Kitagawa et al. in 1983 [14]. Here, the hydrogen distribution was determined in dependency of the mechanical stress field. Sofronis et al. [15] adopted this idea, using a stress driven hydrogen distribution model to estimate the transient hydrogen concentration in the vicinity of a blunted crack tip. Here, it was distinguished between the accumulated hydrogen in lattice sites and the one bounded to internal lattice defects, as dislocations and grain boundaries.

In order to reflect the strain rate dependency of the transient hydrogen distribution and to overcome the effect of hydrogen generation, Krom et al. [16] proposed to add a strain rate dependent term to the transient hydrogen equation of Sofronis et al. [15]. Especially for high strain rates, the hydrogen distribution in lattice sites is reduced while hydrogen is trapped at the rapidly generated internal material defects. The use of a strain gradient plasticity model was recently proposed by Martínez-Pañeda et al. [17], leading to increased plastic deformations and thus rising hydrogen concentrations at crack tips.

To simulate the effect of hydrogen on the material properties, several approaches exist. Lufrano et al. [18] proposed that hydrogen induces a purely dilatational straining inside the material, based on the work of Peisl [19]. Liang and Sofronis [20] included a hydrogen induced strain which also affects the plastic behaviour of the material. A further idea is to include a hydrogen effect on the material yield strength for a local softening effect [15]. (For a detailed discussion of the proposed hydrogen embrittlement mechanisms and their numerical realization it is referred to chapter 3.3 and chapter 3.4, respectively.)

The simulation of hydrogen embrittlement in a real pipeline structure is rarely found in literature. In most cases, surrogate models are used where the connection between a real pipeline structure and the applied boundary conditions cannot be established in a straight forward way (compare for example [21, 22, 17]). If authors do not mention the pipeline dimensions reflected by the surrogate model, consequently no practical conclusions regarding the pipeline proportion and loading conditions can be drawn from the numerical surrogate model results.

Several studies focusing on a pipeline structure with a blunted radial crack exist, for example publications of Datfarnia et al. [23, 24] and Takayama et al. [25].

However, the effect of the determined hydrogen concentrations on the material properties is rarely investigated in a continuum sense. Here, for example Datfarnia et al. [26] analyse the effect of hydrogen on the material properties at a radially cracked pipeline specimen. The effect of hydrogen induced softening on the void growth behaviour was discussed, where solely the trapped hydrogen concentration was claimed to affect the material properties. In contrast to that, Kotake et al. [13] implied that the total hydrogen concentration, being the one in lattice and in trapping sites, affects the material properties and showed a local softening effect in front of a blunted crack under cyclic loading conditions.

The aim of this thesis is to investigate the effect of hydrogen on the material properties and discuss as well as evaluate the existing modelling approaches. To achieve this, the effect of a transient hydrogen distribution on the material properties is simulated at the example of a representative structure of the natural gas pipeline system.

1.3. Organization of work

After a recapitulation of fundamental mechanical theories in chapter 2, the phenomenon of hydrogen embrittlement is discussed in detail in chapter 3. Firstly, the general conditions in the natural gas pipeline system are presented. Then, based on a synopsis of experimental studies, the effect of hydrogen on the material behaviour is examined and the possible mechanisms of hydrogen embrittlement are evaluated. Furthermore, the mathematical description of the proposed hydrogen embrittlement mechanisms are discussed.

In chapter 4, the iterative scheme of the mechanical continuum model coupled with the transient hydrogen distribution model implemented in this thesis is presented, alongside the applied numerical schemes.

An overview of representative modelling parameters for a natural gas pipeline is given in chapter 5. Here, a full field pipeline model as well as a surrogate version are defined. After verifying compatibility of both models, the general hydrogen distribution in front of a crack tip is described while in a next step the effect of three different approaches accounting for hydrogen embrittlement is investigated in chapter 6. Subsequently, the effect of the assumed crack length is discussed qualitatively.

2. Fundamentals

In this chapter, an overview of the fundamental mechanical relations used within this thesis is given. After the basic formulations for continuum mechanics are summarized, a short overview of the micro mechanical motivation and interpretation of continuum modelling is presented. Furthermore, the applicability of the stress intensity factor is discussed.

2.1. Continuum mechanics

In this work, the effect of hydrogen on the material of the existing natural gas pipeline system is investigated by applying a continuum model. In continuum mechanics, the macroscopic behaviour of a body is investigated rather than the actions on the atomic length scale. Every point of the continuum represents the underlying micro structure in a statistical manner. The general concept of continuum mechanics is briefly summarized in the following. For a more detailed introduction it is referred to fundamental literature, like [27, 28] as well as [29] which serve as a basis for the following overview.

2.1.1. Kinematics and stress relations

In a general continuum framework every object is considered to be a body consisting of different material points. It is distinguished between the original position of a material point in a body, referred to as reference configuration B_0, and a current (moved, deformed) configuration B of a point in a continuous body which is schematically depicted in Figure 2.1. The quantities of the reference configuration are denoted by upper case letters, like the position vector $\boldsymbol{X}$ of a material point P_m and the derivative with respect to the reference configuration $Grad$. The variables of the current configuration are denoted by lower case letters, like the position vector $\boldsymbol{x}$ of a material point P_m. The reference configuration is linked with the current one by the displacement vector $\boldsymbol{u} = \boldsymbol{x} - \boldsymbol{X}$. There is always one point of the reference configuration uniquely mapping to the current configuration $\boldsymbol{x} = \phi(\boldsymbol{X})$ with the deformation gradient $\boldsymbol{F} = Grad(\boldsymbol{x}) = \boldsymbol{I} + Grad(\boldsymbol{u})$. The symbol $\boldsymbol{I}$ represents the identity matrix. The transformations of line, area and volume elements are summarized in Figure 2.1.

In case a body is deformed, a strain is induced. A definition of the strain can be derived by polar decomposition of the deformation gradient $\boldsymbol{F} = \boldsymbol{R}\boldsymbol{U} = \boldsymbol{V}\boldsymbol{R}$ with the stretch tensors $\boldsymbol{U}$ and $\boldsymbol{V}$ as well as the rotation tensor $\boldsymbol{R}$ of the body [28, 27]. Based on these stretch tensors, the right Cauchy-Green tensor $\boldsymbol{C} = \boldsymbol{U}^2 = \boldsymbol{F}^T\boldsymbol{F}$ and the left Cauchy-Green tensor $\boldsymbol{c} = \boldsymbol{V}^2 = \boldsymbol{F}\boldsymbol{F}^T$ can be defined independent of the rotation of the body. The Green-Lagrange strain tensor as well as the Euler-Almansi strain tensor are commonly used definitions of the strain in the reference and current configuration, respectively, as illustrated in Figure 2.2.

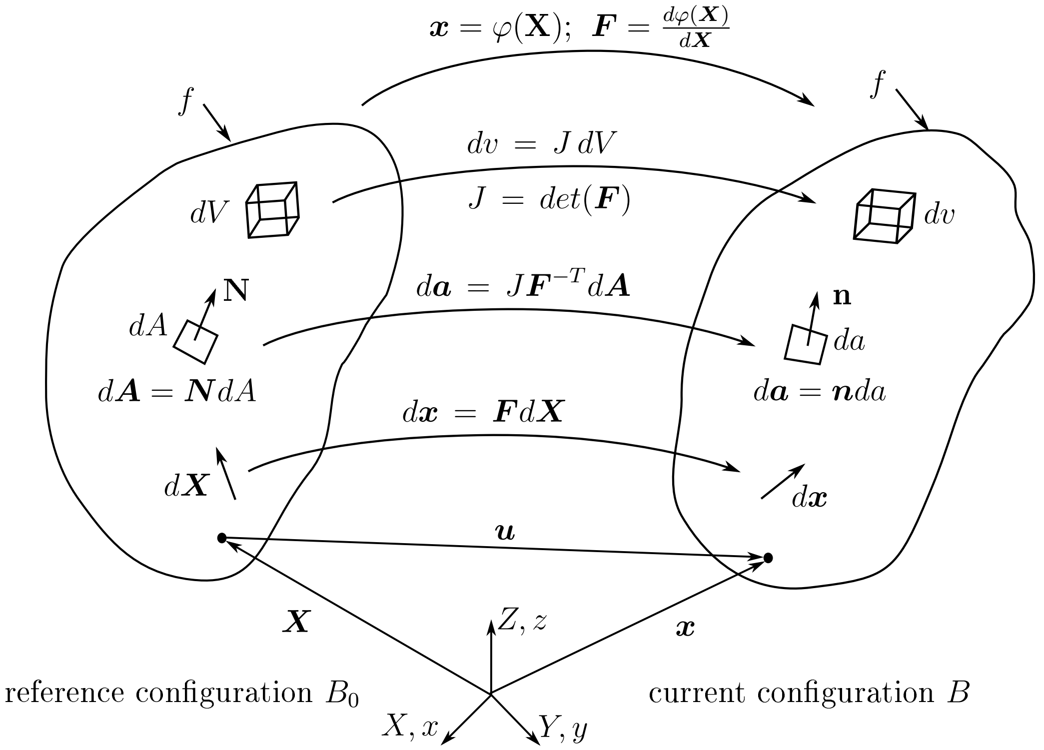

Figure 2.1.: Scheme of kinematic relations in continuum mechanics (adapted from [29])

The stress state of a body can be determined by examining a small cutting plane da in the current configuration and the according agent force $d\boldsymbol{f}$ in this cutting plane, compare Figure 2.2. Then, the associated stress vector reads $\boldsymbol{t} = \frac{d\boldsymbol{f}}{da}$ in the current configuration. Analogically, the stress vector in the reference configuration is defined as $\boldsymbol{T} = \frac{d\boldsymbol{f}}{dA}$.
The problem of this stress formulation is its dependence on the orientation of the cutting plane. An independent formulation of the cutting plane orientation can be derived by using the Cauchy theorem for the stress tensor in the current configuration $\boldsymbol{t} = \boldsymbol{\sigma} \cdot \boldsymbol{n}$ with the Cauchy stress tensor $\boldsymbol{\sigma}$ and the normal of the cutting plane $\boldsymbol{n}$.
In both configurations, the infinitesimal force $d\boldsymbol{f} = \boldsymbol{t}\,da = \boldsymbol{T}\,dA$ needs to be the same. From this relation, the stress tensor of the reference configuration can be defined independent to the orientation of the cutting plane as $\boldsymbol{T} = \boldsymbol{P}\cdot\boldsymbol{N}$ with the first Piola-Kirchhoff tensor $\boldsymbol{P}$ and the normal of the cutting plane $\boldsymbol{N}$ in the reference configuration.
The most common stress definitions are summarized in Figure 2.2 for the current and reference configuration as well as their transformation between the two configurations.

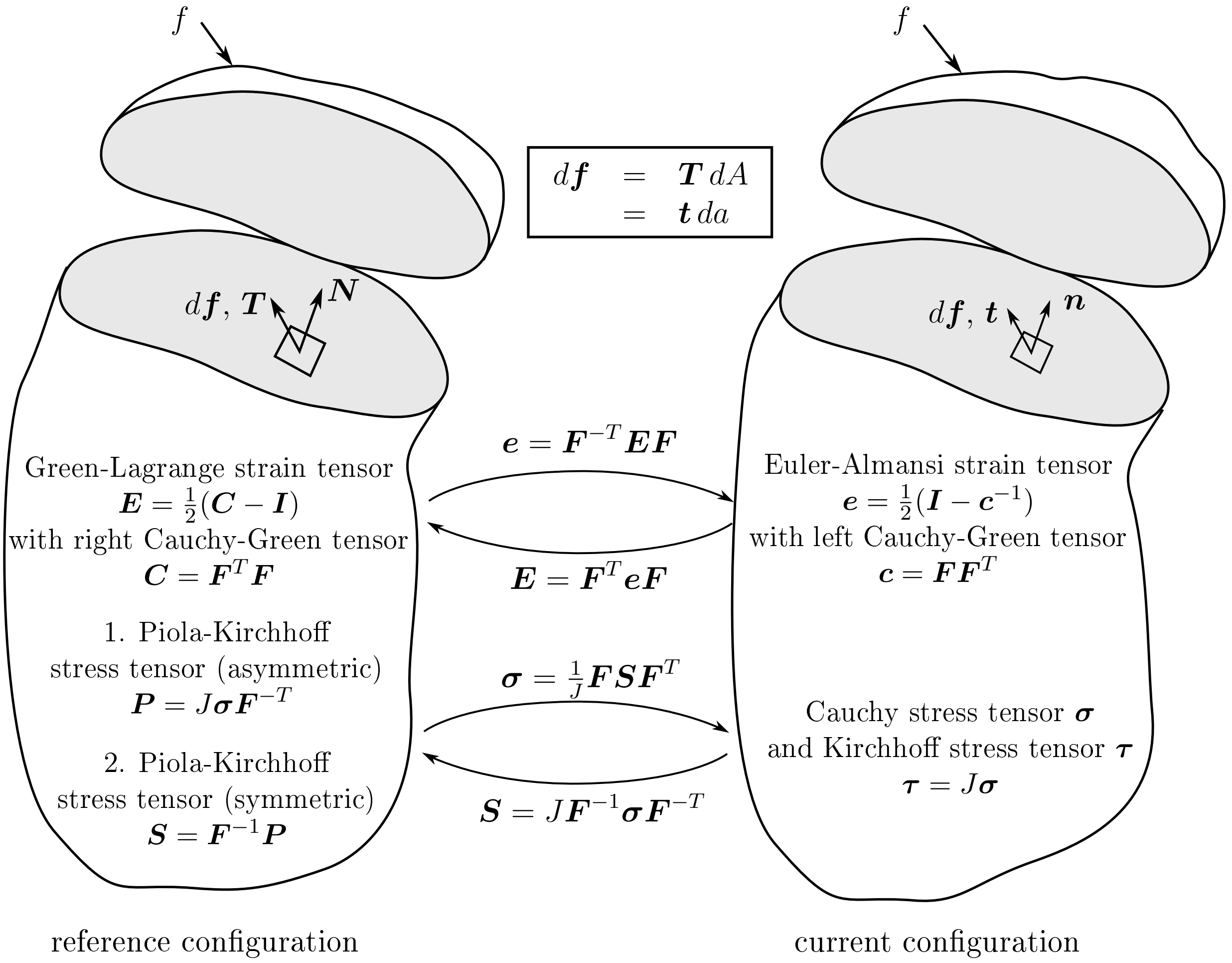

Figure 2.2.: Overview of commonly used stress and strain notation in continuum mechanics (adapted from [29])

2.1.2. Balance principles

The balance principles are physical descriptions of the behaviour of a continuum body independent from the specific material response. These mathematical formulations provide an underdetermined system of equations which needs to be complemented by material dependent relations.

To describe the general physical behaviour in continuum mechanics, balance equations are formulated, namely the balance of mass, the balance of energy (first thermodynamic law) as well as the balances of linear and angular momentum. Furthermore, the inequality of entropy (second thermodynamic law) needs to be considered.

From the balance of angular momentum, the symmetry of the stress tensor $\boldsymbol{\sigma}$ can be concluded.

The balance of energy takes into account that the change of the total energy over time in a body B is equal to the heat flow inside this body and the external power acting on it. Since the investigated natural pipeline system is considered to be isothermal in this work, the balance of energy does not need to be solved.

The entropy inequality describes the evolution of the disorder of the system and can only be positive. From this inequality, the Clausius-Duhem inequality can be derived. According to this relation the stress can be defined by a strain energy function.

The balance of mass and the balance of linear momentum shall be briefly summarized in the following to obtain the differential equations which will be solved in a weak matter in the finite element framework in chapter 4.

Balance of mass

The mass m of a body B is considered not to change over time

$$\frac{d}{dt}m = \frac{d}{dt}\int\limits_{B_t} \rho\, dv = \int\limits_{B_t} \dot{\rho} + \rho\, div(\boldsymbol{v})\, dv = 0. \tag{2.1}$$

Here, ρ is the mass density and $\dot{\rho}$ is its time derivative. The velocity of a material point is given by $\boldsymbol{v} = \frac{d\boldsymbol{u}}{dt}$. Since the relation above holds true for the entire volume and as a continuous parameter field is assumed, this condition needs to be fulfilled in every point of the volume. Thus, equation (2.1) can be formulated in the local form as

$$\dot{\rho} + \rho\, div(\boldsymbol{v}) = 0. \tag{2.2}$$

Balance of linear momentum

The linear momentum $\rho\boldsymbol{v}$ associates the mass density ρ with the local velocity of a particle $\boldsymbol{v}$. This momentum describes the kinematic state of a body. The balance of linear momentum incorporates that the time rate of the linear momentum is equal to the sum of the applied external forces. In its local form the balance equation reads

$$\rho\dot{\boldsymbol{v}} = \rho\boldsymbol{b_f} + div(\boldsymbol{\sigma}) \tag{2.3}$$

with the body forces $\boldsymbol{b_f}$.
In case of quasi-static loading the acceleration $\dot{\boldsymbol{v}}$ is considered to be zero and thus the differential equation simplifies to the equilibrium condition of surface and volume forces

$$0 = \rho\boldsymbol{b_f} + div(\boldsymbol{\sigma}). \tag{2.4}$$

2.1.3. Constitutive theory

The previously discussed balance equations describe the fundamental physics of a body. Nevertheless, the actual behaviour of a material cannot be reproduced by these equations alone. Therefore, constitutive equations are needed to relate the kinematic measures with the stress tensor. These equations capture the empirically determined characteristics of a material.
Within this work, an elastic and an elasto-plastic material model are used. The basic material descriptions are summarized in the following.

Elastic material

The stress-strain relation of a linear elastic material can be derived from an uniaxial tensile test. From this observation the free energy function ψ_e for small deformations can be postulated with the strain tensor $\boldsymbol{\varepsilon}$ and the fourth order material tensor $\mathbb{C}$ as

$$\begin{aligned}\psi_e &= \frac{1}{2}\boldsymbol{\varepsilon}\cdot\cdot(\mathbb{C}\cdot\cdot\boldsymbol{\varepsilon}) \\ &= \frac{1}{2}\kappa\, tr(\boldsymbol{\varepsilon})^2 + \mu\,\|\widetilde{\boldsymbol{\varepsilon}}\|.\end{aligned} \tag{2.5}$$

This relation can be rewritten with the trace of the strain tensor $tr(\boldsymbol{\varepsilon}) = \frac{1}{3}\varepsilon_{kk}$ as well as the deviatoric strain component $\widetilde{\boldsymbol{\varepsilon}} = \boldsymbol{\varepsilon} - tr(\boldsymbol{\varepsilon})\boldsymbol{I}$. For isotropic and homogeneous materials only two material dependent parameters need to be considered, the bulk modulus κ and the shear modulus G which is also referred to as the Lamé constant μ. These two parameters can in turn be expressed in dependence on the Young's modulus E and the Poisson's ratio ν, as follows

$$\mu = \frac{E}{2\,(1+\nu)} = G \tag{2.6}$$

$$\kappa = \frac{3\,\lambda_E + 2\,\mu}{3} \qquad \text{with } \lambda_E = \frac{\nu E}{(1+\nu)(1-2\nu)}. \tag{2.7}$$

The stress $\boldsymbol{\sigma}$ and the linear elasticity tensor $\mathbb{C}^e$ can be derived from the free energy function by

$$\boldsymbol{\sigma} = \frac{\partial\psi}{\partial\boldsymbol{\varepsilon}}, \qquad \mathbb{C}^e = \frac{\partial^2\psi}{\partial\boldsymbol{\varepsilon}\partial\boldsymbol{\varepsilon}}. \tag{2.8}$$

Then, the elastic stress can be expressed as

$$\boldsymbol{\sigma} = \kappa\, tr(\boldsymbol{\varepsilon})\,\boldsymbol{I} + 2\mu\,\boldsymbol{\varepsilon} \tag{2.9}$$

and the linear elasticity tensor results in

$$\mathbb{C}^e = \kappa\,\boldsymbol{I}\otimes\boldsymbol{I} + 2\mu\left(\mathbb{I} - \frac{1}{3}\boldsymbol{I}\otimes\boldsymbol{I}\right) \tag{2.10}$$

with the fourth order identity tensor $\mathbb{I}$.

Elasto-plastic material

The elasto-plastic material model assumes small deformations and includes hardening effects. This material model will be modified in chapter 3.4 to account for the influence of hydrogen.

For small deformations, the strain can be additively decomposed into an elastic part $\boldsymbol{\varepsilon}_e$ and a plastic part $\boldsymbol{\varepsilon}_p$,

$$\boldsymbol{\varepsilon} = \boldsymbol{\varepsilon}_e + \boldsymbol{\varepsilon}_p. \tag{2.11}$$

The plastic strain $\boldsymbol{\varepsilon}_p$ can be microscopically interpreted as the movement of dislocations and thus this strain does not induce further stresses. The plastic strain is considered to be purely deviatoric.

The free energy function ψ can also be decomposed into an elastic part ψ_e and a plastic part ψ_p

$$\psi = \psi_e(\boldsymbol{\varepsilon}_e) + \psi_p(a, \boldsymbol{b}). \tag{2.12}$$

The elastic part of the free energy function ψ_e has been already defined in equation (2.5). The plastic part of the free energy function depends on a scalar parameter a representing isotropic hardening and a tensor $\boldsymbol{b}$ expressing kinematic hardening. This relation can be defined according to Lubliner [27] like

$$\psi_p(\boldsymbol{\varepsilon}_p) = \frac{1}{2} H_{iso}\, a^2 + \frac{1}{3} H_{kin}\, \|\boldsymbol{b}\|^2 \tag{2.13}$$

with H_{iso} and H_{kin} being scalar material parameters accounting for the amount of isotropic and kinematic hardening, respectively.

The Clausius-Duhem inequality can be expressed, with the assumption that the plastic strain does not induce volumetric straining, as

$$D_{in} = \boldsymbol{\sigma} \cdot \cdot \tilde{\varepsilon}_p - \underbrace{\frac{\partial \psi}{\partial a}}_{-\alpha} \dot{a} - \underbrace{\frac{\partial \psi}{\partial \mathbf{b}}}_{-\boldsymbol{\beta}} \dot{\boldsymbol{b}} \tag{2.14}$$

with the conjugated thermodynamic forces α and $\boldsymbol{\beta}$.

The principle of maximal dissipation states that the real stress state is the stress state out of all possible ones which maximizes the inner dissipation $D_{in} \rightarrow max$ [30]. This optimization problem is confined by defining a boundary of the elastic material behaviour in form of a flow rule f. The restricted optimization problem reads

$$\mathbb{O} = -D_{in} + \lambda\, f(\widetilde{\boldsymbol{\sigma}}, a, \boldsymbol{b}). \tag{2.15}$$

The Lagrange multiplier λ has to fulfil the Kuhn-Tucker conditions ($\dot{\lambda} \geq 0,\ f \leq 0,\ \lambda f = 0$) and the flow rule f needs to be defined such that the consistency requirement ($\dot{f} = 0$, if $f = 0$) holds true.

In this work, an isotropic steel is assumed and thus the von Mises flow rule is applied. According to the assumption that hydrostatic stresses do not induce plastic deformations, the von Mises flow rule can be defined in dependency of the deviatoric part of the stress $\widetilde{\boldsymbol{\sigma}}$ to

$$f = \|\widetilde{\boldsymbol{\sigma}} - \boldsymbol{\beta}\| \; - \; \sigma_y(\sigma_{y0}, \alpha). \tag{2.16}$$

In case $f < 0$ the material behaves purely elastic, whereas $f = 0$ denotes plastic straining. Stress states resulting in $f > 0$ are invalid and need to be projected back such that $f = 0$. The function $\sigma_y(\sigma_{y0}, \alpha)$ accounts for isotropic hardening

$$\sigma_y(\sigma_{y0}, \alpha) = \sqrt{\frac{2}{3}}(\sigma_{y0} + \alpha) \tag{2.17}$$

with the yield stress σ_{y0} of the material and the isotropic hardening parameter α. The evolution equation for the plastic strain rate $\dot{\tilde{\boldsymbol{\varepsilon}}}_p$ as well as the inner hardening variables $\dot{\boldsymbol{b}}$ and $\dot{a}$ can be derived from equation (2.15) to

$$\begin{aligned} \frac{\partial \mathbb{O}}{\partial \tilde{\boldsymbol{\sigma}}} \quad &\rightarrow \quad \dot{\tilde{\boldsymbol{\varepsilon}}}_p = \quad \dot{\lambda} \frac{\partial f}{\partial \tilde{\boldsymbol{\sigma}}} = \dot{\lambda}\, \boldsymbol{n}, \\ \frac{\partial \mathbb{O}}{\partial \boldsymbol{\beta}} \quad &\rightarrow \quad \dot{\boldsymbol{b}} = \quad \dot{\lambda} \frac{\partial f}{\partial \boldsymbol{\beta}}, \\ \frac{\partial \mathbb{O}}{\partial \alpha} \quad &\rightarrow \quad \dot{a} = \quad \dot{\lambda} \frac{\partial f}{\partial \alpha}. \end{aligned} \tag{2.18}$$

The normal tensor $\boldsymbol{n} = \frac{\partial f}{\partial \tilde{\boldsymbol{\sigma}}} = \frac{\tilde{\boldsymbol{\sigma}}}{\|\tilde{\boldsymbol{\sigma}}\|}$ is the normalized deviatoric stress and is orthogonal to the yield surface in the principle stress space. This dimensionless normalized tensor defines the correction direction of the invalid stress states. From the consistency condition $\dot{f} = 0$ if $f = 0$, the rate of the plastic multiplier can be expressed as

$$\dot{\lambda} = \frac{\boldsymbol{n} \cdot \cdot \dot{\tilde{\boldsymbol{\varepsilon}}}}{1 + \frac{H_{kin} + H_{iso}}{3\mu}}. \tag{2.19}$$

The stress $\boldsymbol{\sigma}$ and the material tangent $\mathbb{C}^{ep}$ can be derived as in the elastic case from equation (2.8) to

$$\boldsymbol{\sigma} = \kappa\, tr(\boldsymbol{\varepsilon})\, \boldsymbol{I} + 2\mu \left(\widetilde{\boldsymbol{\varepsilon}} - \widetilde{\boldsymbol{\varepsilon}}_p\right) \tag{2.20}$$

and

$$\mathbb{C}^{ep} = \kappa\, \boldsymbol{I} \otimes \boldsymbol{I} + 2\mu \left(\mathbb{I} - \frac{\boldsymbol{n} \otimes \boldsymbol{n}}{1 + \frac{H_{kin} + H_{iso}}{3\mu}} \right). \tag{2.21}$$

2.2. Micro mechanical motivation of continuum mechanics

The mechanical characteristics of a given material depend on its structure and behaviour on the atomic length scale. Nevertheless, for most engineering purposes it is feasible to assume a homogeneous structure to avoid calculations of every atomic interaction. Focusing on the atomic length scale would increase the numerical calculation time immensely.

Still, to be able to find appropriate continuum models accounting for hydrogen embrittlement, in this chapter a short recall of the general behaviour of metals on atomic length scale is given. This knowledge serves as the basis to understand the link of experimental findings of hydrogen influencing material defects on meso length scale, summarized in chapter 3.2.5, and the related continuum mechanical interpretation. For detailed information on the micro structure, its formation and behaviour, it is referred to text books, as [31].

The lattice of steel is not homogeneous in general. It consists of different grains and includes further defects such as point and line defects. In the following, only defects of the lattice, which are relevant for this work, are described.

The micro structure of steel consists of different grains, which are connected by the so called grain boundaries, schematically depicted in Figure 2.3. Dislocations are line defects

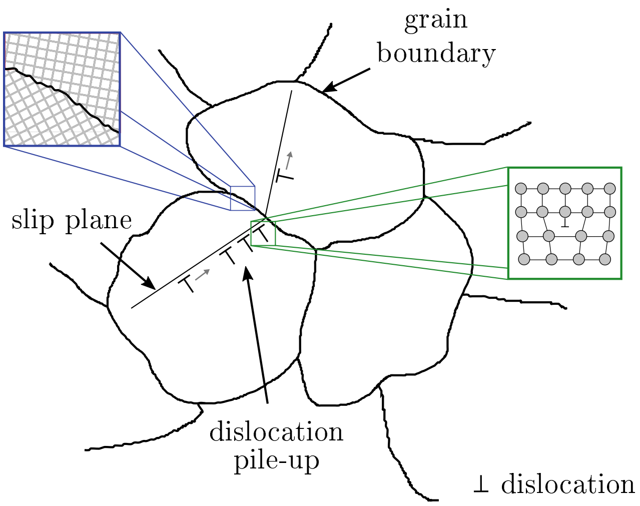

Figure 2.3.: Schematic representation of grain boundary and dislocation interaction

which can move on slip planes within a grain when a critical stress state is reached. These dislocations induce stress localizations due to the disorder of the lattice and can act as sink for smaller particles. When given dislocations arrive at a grain boundary, their motion is impeded and a dislocation pile-up forms. The stress level of the closest dislocation to the grain boundary increases while more dislocation accumulate in the pile-up. In case a critical stress state is reached, the first dislocation enters and increases here the disorder of the grain boundary. The grain boundary can also send out dislocations into a neighbouring grain. These sent out dislocations do not need to have the same (global) slip plane direction as the entering dislocations, since the neighbouring grain does not have the same grid orientation. However, not for every dislocation entering a grain boundary, another one is sent out in a neighbouring grain. Therefore, the disorder of the grain boundary generally increases with increasing dislocation interaction.

The movement of dislocation themselves is irreversible. This implies that if the loading of the body is relaxed, the dislocations remain at its current position as there is no driving force moving them back to its original position before loading. On macroscopic level, this is referred to as irreversible deformations and in continuum mechanics interpreted as plastic deformations.

The hardening effect of metals observed on macroscopic level can be explained on the meso length scale by a pile up of dislocations at grain boundaries. Here, a higher stress level than within the lattice of a grain is needed to enter the grain boundary. Thus, the material can carry more load and macroscopically hardening effects can be observed.

The same kind of hardening effect can be observed for impurities in the host metal structure. Therefore, most alloys have a higher stress resistance.

The described motivation of continuum mechanics from the micro level is important when discussing the experimental findings of hydrogen on the mesoscale in chapter 3.

2.3. Stress intensity factor

In this chapter, a brief overview on the stress intensity factor and T-stress is given.
The stress intensity factor K was first defined in linear elasto-mechanics as means to describe the stress state at a crack tip. Here, the stress intensity factor can be understood as a factor scaling the amplitude of the spatial elastic stress distribution. Accordingly, the factor depends on the applied stresses as well as the geometry of the cracked specimen. For various simple problems, analytical solutions can be found in fundamental fracture mechanics literature, as [32, 33]. For more complex structures, numerical analyses like the finite element method (FEM) are used.
Since in this thesis a rather complex structure under mode one opening condition is investigated, the stress intensity factor K_I is determined by FEM. Here, mode one opening conditions denote a pure tensile straining of a crack and the according stress intensity factor is marked with a subscript I. For a detailed discussion of different loading modes it is again referred to fracture mechanics literature [32, 33].
Once the stress state is determined by an elastic FEM calculation, the stress intensity factor can be calculated for mode one opening conditions by

$$K_I(r) = \lim_{r \to 0} \sigma_{yy}(r)\sqrt{2\pi r}, \tag{2.22}$$

with the stress σ_{yy} in y direction and the distance of the crack tip r defined in radial coordinates (as depicted in Figure 2.4).
The stress intensity factor is often used to predict crack propagation. Then, a critical value of the stress intensity factor $K_{I,C}$ is determined, in most cases on empirical basis. If the calculated value of K_I exceeds the critical one $K_{I,C}$, the crack is assumed to propagate [32, 33].
Aside from the stress intensity factor K_I another factor, namely the so-called T-stress, is used to characterize the stress state at a crack tip. The T-stress is widely referred to as the stress acting parallel to the crack tip in x-direction [34]. In literature, numerous ways are proposed to calculate the T-stress. In this thesis, the stress difference method is used

$$T = \lim_{r \to 0}(\sigma_{xx}(r) - \sigma_{yy}(r)), \tag{2.23}$$

where T denotes the difference of the stresses in x- and y-direction [34].
Nevertheless, the mathematical origin of the term T-stress is often overseen [34]. Firstly, the term T-stress was introduced by Irwin [35] as a correction term to analytically describe the stress state for uniaxial loading. The analytical equations were originally defined by Westergaard [36] for a biaxial loading state such that a stress in x-direction was calculated at the boundary edges along the axis of the crack by utilizing the equations for uniaxial loading [34]. This axis along the crack is the symmetry plane marked in Figure 2.5. This unphysical stress state for uniaxial loading was corrected by Irwin with the help of the so-called T-stress.
Further studies of Williams [37] showed that the T-stress actually exists [34]. He used eigenseries expansion of the stress field and was able to identify the T-stress as an higher order term [34]. From that time on, the term T-stress was widely interpreted as the stress acting parallel to the crack tip (in x-direction).
Since the definition of the stress intensity factor K_I and T-stress originate from linear fracture mechanics, this theory has some limitations. The valid area of this description

is limited to the vicinity of the crack tip, which is schematically illustrated in Figure 2.4. Here, a crack is depicted which is enclosed by circles with their origin in the crack tip. The marked grey area reflects the valid field of the linear theory. In case the outer boundary (marked by r_{out}) is exceeded, higher order terms of the eigenseries expansion cannot be neglected any more. Then, the linear equations discussed above are not longer valid (compare numerical example in Figure 2.5).

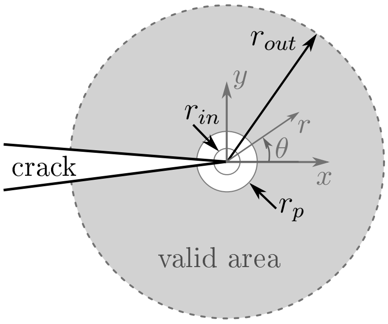

Figure 2.4.: Valid area of linear theory used for determination of K_I and T-stress (adapted from [33])

In addition to the outer boundaries, the linear theory is also not valid in the direct vicinity of the crack tip (marked with r_{in}), since here the analytical solution gives infinitely high stresses. Obviously, this unrealistic stress state needs to be excluded when evaluating the results.

Additionally, it has to be kept in mind that plastic deformations are also not considered and thus the stress state proposed by the linear elastic theory has to be judged as tendentially too high. Therefore, the valid area of the linear theory starts at the boundary of the plastic zone size r_p.

To ensure that the stress intensity factor K_I and the T-stress properly reflect the stress conditions at the crack tip, the area of unphysical stresses r_{in} and the plastic zone size r_p have to be much smaller than the valid or investigated area (r_{in}, $r_p \ll r_{out}$) [33]. This is also known as small scale yielding. The plastic zone size can be predicted by

$$r_p = \frac{1}{2\pi}\left(\frac{K}{\sigma_0}\right)^2 \tag{2.24}$$

with the yield stress σ_0.

Within this thesis, a numerical determination of K_I and T-stress is performed. Its determination scheme and the limitations of the theory are illustrated at a small example with known analytical solution: A single edged notched plate.

The plate features a sharp crack of the length $a_c = 2\,mm$ and is exposed to uniaxial loading, as depicted in Figure 2.5, left. The stress intensity factor $K_I(r)$ is calculated from linear elastic numerical calculations and is derived by equation (2.22). The results are plotted over the symmetry plane of the plate in Figure 2.5, right.

These results of the stress intensity factor can be divided into three parts: A highly non-linear part close to the crack tip, a strongly linear part and again a non-linear part far from the crack tip.

In a first step, the non-linear results close to the crack tip and far from the crack are excluded. The valid area of the linear theory is the linear part of the graph, marked in grey.

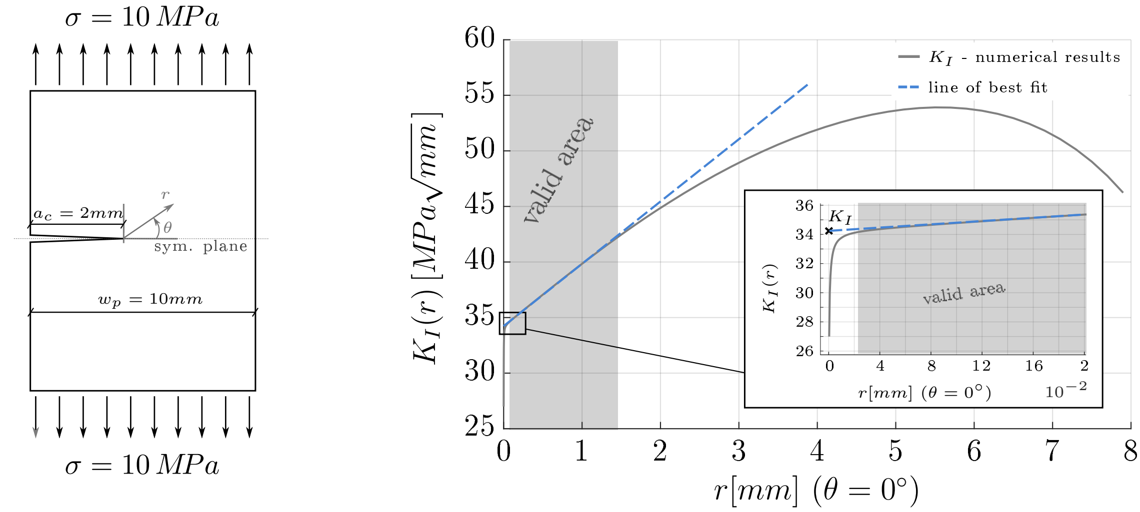

Figure 2.5.: Model of the single edged notched plate (left) and numerical determination of the stress intensity factor K_I (right)

In a second step, a line of best fit is constructed from the results of $K_I(r)$ in the grey area and the stress intensity factor is determined by linear extrapolation to the crack tip to $K_{I,n} = 34.24 MPa\sqrt{mm}$ (linear extrapolation method [38]).

This numerically determined stress intensity factor can be cross-checked with the analytical solution. An analytical solution of K_I for the example of the single edged notched plate can be determined by

$$K_I = C\,\sigma\sqrt{\pi a_c} \tag{2.25}$$

with

$$C = 1.12 - 0.231\left(\frac{a_c}{w_p}\right) + 10.55\left(\frac{a_c}{w_p}\right)^2 - 21.72\left(\frac{a_c}{w_p}\right)^3 + 30.39\left(\frac{a_c}{w_p}\right)^4 \tag{2.26}$$

up to a ratio of $a_c/w_p = 0.6$ [32]. Here, the width of the plate is represented by w_p and the crack length by a_c as depicted in Figure 2.5, left. The resulting analytical stress intensity factor is determined to $K_{I,a} = 34.36 MPa\sqrt{mm}$. When comparing $K_{I,a}$ to $K_{I,n}$, a variation of $0.3\,\%$ is considered as reasonable.

One could argue that the numerical determination of the stress intensity factor depends on the range used for the line of best fit and in turn the definition of the valid area of the linear elastic theory. Nevertheless, the resulting stress intensity factor K_I is not sensitive to slight variations of the chosen range of values for the best fit line. Therefore, the respective range marked in Figure 2.5, right, should not be understood as a precise rule for the exact calculation of K_I.

As stated above, changing the range of the so-called valid area does not have a high impact on the determined stress intensity factor. Still, when defining the range of results utilized to derive the best fit line, one needs to keep in mind the previously discussed limitations of this linear theory.

According to its similarity to the analytical solution, the linear extrapolation method is considered to be accurate to determine the stress intensity factor. The determination of the T-stress follows an analogous procedure and is therefore not discussed in detail.

As a side note, it should also be mentioned that some strategies exist to extend this linear theory to consider plastic deformations. Nevertheless, within this thesis the determined values of K_I and T are used to define the boundary conditions of a surrogate model and not to evaluate a critical stress state at the crack tip for crack propagation. Therefore, no plastic effects will be discussed at this point.

3. Hydrogen Embrittlement

The first observations of hydrogen embrittlement were made already about 140 years ago by Johnson [4], but the actual mechanism leading to the brittle response within metals is still controversially discussed within literature.

In this chapter, an overview of the conditions in the natural gas pipeline system is given and the experimental findings of how hydrogen influences the pipeline materials are summarized. On the basis of these findings, a likely mechanism for hydrogen embrittlement is investigated. Afterwards, a mathematical model accounting for this mechanism is presented.

3.1. General overview of the present natural gas pipeline systems

Within this study, the effect of hydrogen on natural gas pipeline systems is discussed. Therefore, the actual conditions within the pipeline systems need to be known before the effect of hydrogen can be accounted for.

The European gas network has been established incrementally during the last 78 years [39]. It was developed around existing national gas pipeline systems like the one in Southern France, Northern Italy, Germany and Romania. Due to its short time of existence, in most European states replacements of pipelines has not yet been required. Nevertheless, in some member states, which host the previous national pipeline systems, replacements have to be considered [39]. Due to these different conditions in local pipeline systems, it would be misleading to discuss the European natural gas pipeline system as a whole. In the following, the German pipeline system is considered in more detail.

The German gas pipeline system was formed step by step by merging local private pipeline systems over several decades [40]. This growing pipeline system, mainly in the private sector, differs significantly from the one of other European countries where the system was predominantly shaped by the government. This can be clearly seen when comparing the 16 transmission system operators in Germany with only seven in Austria and two in France [40]. Transmission system operators deliver the natural gas from the producer to local gas distribution companies. Furthermore, the German gas system, with its 700 regional gas distribution companies, is the most complex one in Europe.

Due to the fact that the German natural gas pipeline system grew together from regional ones, also different materials and conditions may be encountered. In general, mostly steel grades from S235 to S355 can be found. In the last decades also the high strength pipeline steel X70 was used in numerous projects in Germany for high pressurised gas pipelines [41]. Since there is a need of improving the strength level of the pipelines to reduce the amount of required material and thus the costs, the pipeline steel X80 was developed and the first pipeline was commissioned in Germany in 1992 [42]. As of today, this material is well established [42] while the ultra high strength pipeline steel X100 is still under investigation and is not industrially produced by now.

The dimensions and pressures vary for pipelines transmitting the gas over long distances (transmission pipeline) and the local distribution system. The pressure in a transmission pipeline is reported to be up to $100\,bar = 10\,MPa$ with diameters above $500\,mm$ [40, 39]. In local distribution systems the diameters are mostly between $225\,mm$ and $350\,mm$ at pressures from $0.1\,bar$ and $1\,bar$ [43, 44].

In the natural gas pipeline system, it is a frequent occurrence that some sections are damaged during their service life, such as by corrosion and local cracks [45]. These passages need to be monitored and partly replaced. But not every locally damaged pipeline has to be replaced immediately since the operation safety is not markedly influenced. Even when the pipeline is locally damaged and thus the material is exposed to local plastic deformations, the rest of the pipeline can still carry the load in most of the cases [45]. Nevertheless, this needs to be proven for every critical part according to the normative standard.

When following the idea of transporting hydrogen gas through the existing natural gas pipeline system, the brittle effect on the pipelines needs to be quantified. Especially the impact on already damaged pipeline segments needs to be carefully investigated since hydrogen accumulates at the local stress and strain peaks around these defects [15, 46]. This locally increased hydrogen concentration can promote brittle crack propagation which in turn leads to a brittle collapse of the whole pipeline segment.

In the following chapter, the general observed effect of hydrogen embrittlement is summarized and parameters influencing the amount of embrittlement are discussed.

3.2. Experimental investigations of hydrogen effect on metals

Within literature, a substantial amount of experimental studies investigating different aspects of hydrogen embrittlement for different materials is available. Since the influence of hydrogen is, beside other factors, scattering for different materials and since there is no standard testing procedure, the according results can very well be even contradictory [47]. An overview of test results for various materials is given by Somerday [48]. In this chapter, experimental findings for low carbon steels used typically in the natural gas pipeline system exposed to hydrogen are discussed.

First of all, the experimental observations are reviewed. Then parameters influencing the amount of hydrogen embrittlement are examined. A summary of the chemical composition of the discussed materials can be found in Table A.1 and Table A.2 in the appendix.

3.2.1. Analysis of fracture strain and fracture surface at the example of tensile tests

The brittle effect of hydrogen can be well shown by the example of tensile tests. In Figure 3.1 the stress-strain curves for two types of tensile specimens, smooth and notched, are schematically depicted.

For smooth specimens, the hydrogen influence is limited to alter the specimen's elongation in the plastic regime, as depicted in Figure 3.1, left. A pronounced effect on the yield stress σ_{y0} or the ultimate tensile strength (UTS) σ_u cannot be detected. This behaviour was recognized for various low carbon steels (A-516-USA, A-516-JAP, A-106-B, A-14, BF-5, DG-2) by Hoover at al. [49] and for a mild low carbon steel S235JR by Merson et al. [50]. The tensile specimens by Hoover et al. [49] were extracted from pipelines, which were already in service, as well as virgin materials. The tests were conducted in a high pressure

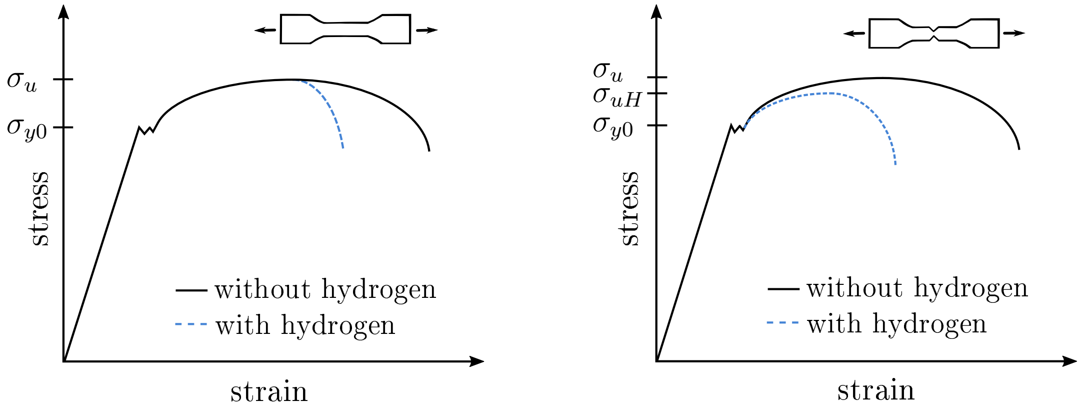

Figure 3.1.: Schematic illustration of hydrogen influence by the stress-strain curve for a smooth tensile specimen (left) and a notched one (right) (derived from the results of Hoover et al. [49])

cell with a hydrogen gas pressure of $6.9\,MPa$. The authors observed that the influence of hydrogen starts after reaching the UTS, when necking occurs. It was concluded that hydrogen embrittlement for low and high strength steel is tied to the localization of flow at the specimen neck and is independent from the base metal chemistry as well as the weld metal microstructure.

Merson et al. [50] examined an electrolytically charged flat tensile specimens of the low carbon steel S235JR and concluded all in all the same results: Hydrogen is not affecting the UTS and the yield stress, but is reducing the fracture strain. Using interrupted tensile testing for smooth specimens, Nanninga et al. [51] concluded that the crack initiation starts after reaching the UTS for high strength low carbon steel X100. Thus, hydrogen embrittlement occurs when reaching the UTS which is correlated to the surface crack initiation. Therefore, hydrogen embrittlement is tied to the formation of surface cracks which create new surfaces for an enhanced hydrogen uptake and provide localized stress fields at which hydrogen accumulates.

For a notched tensile specimen, the effect of hydrogen gets more pronounced. Besides the elongation, also the UTS is globally reduced, which is schematically marked by σ_{uH} in Figure 3.1, right. This reduction was noticed for various low carbon steels by Hoover et al. [49]. As for the smooth tensile specimens, hydrogen embrittlement was found to be insensitive to the chemistry and microstructure of the material. However, a strong dependency on the macroscopic yield stress was identified. Therefore, the elongation at the maximal applied force in the presence of hydrogen was measured by Hoover et al., named as critical elongation $\Delta l_u(H_2)$. This elongation $\Delta l_u(H_2)$ was observed to be tied to the crack initiation process at the surface of the tensile specimens. Hoover et al. surprisingly found a correlation of $\Delta l_u(H_2)$ and the yield stress, as reproduced in Figure 3.2. Furthermore, it can be seen from Figure 3.2 that high strength steels (which already tolerate only little plastic deformations in absence of hydrogen) can almost bear no plastic deformations in the presence of hydrogen.

At first sight, the observed reduction of the UTS seems to be contradictory to the results of the smooth tensile specimens. In the following, this peculiarity shall be discussed in more detail.

The reduction of the macroscopic UTS can be explained by the stress localization appearing at the notch tip of the specimen. Here, locally the yield stress is reached

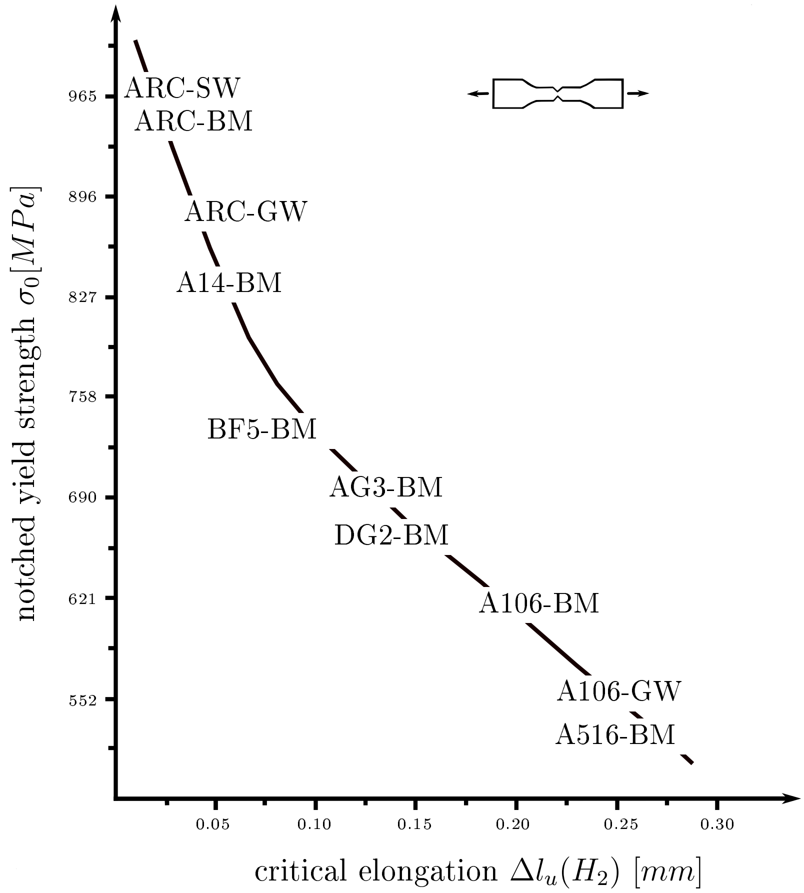

Figure 3.2.: Correlation of initial material yield strength and a critical elongation $\Delta l_u(H_2)$ in the presenence of hydrogen. The critical elongation was identified as the elongation at maximal applied load in an uniaxial tensile test with notched samples in a hydrogen atmosphere. The shortenings specify if the sample was welded: BM - base material, GW - girth weld and SW - seam weld (reproduced from [49], the units were converted from *inch* and *ksi* to *mm* and *MPa*, respectively). The chemical composition of these materials can be found in Table A.2.

earlier than the one measured on macroscopic level. Accordingly, also the UTS is reached locally prior to global detection. As hydrogen accumulates locally, the thereof provoked embrittlement initiates before the macroscopic UTS is achieved. This local embrittlement alters the globally determined UTS of the tensile specimen. In this way, the localization of the embrittlement effect explains the results of notched samples, which at the first sight seem to be in contradiction to the stress-strain curve of the smooth tensile specimens.

This explanation is backed by the results of an interrupted tensile test with a notched sample [49]. The specimens were unaffected by hydrogen until the first surface cracks were initiated closely after reaching the yield stress. The crack formation was directly correlated with the separation of the two stress-strain curves of tensile tests in air and in hydrogen gas (compare Figure 3.1). It is the same observation like for smooth samples: Hydrogen embrittlement could be observed just when surface cracks were formed, triggered by locally reaching the UTS.

Thus, it can be concluded that notched samples generally show the same behaviour as smooth ones while the globally observed reduction of the UTS can lead to a misinterpretation of results. However, to generally characterize the effect of hydrogen on the material properties, a smooth specimen is more suitable since the aforementioned localized effects are excluded, disclosing a more comprehensible material behaviour. Thus, if not indicated differently, smooth tensile specimens are investigated in the following.

Up to this point, the general effect of hydrogen embrittlement on a tensile specimen was discussed by investigating the stress-strain curve. In the following, further parameters indicating the brittle effect of hydrogen are discussed.

Reduction of Area

The reduction of fracture area (RA) of a tensile specimen is a frequently used measure to describe the ductility of materials. Here, the initial cross section of the tensile specimen is compared to the one after straining. A large RA implies large plastic deformations during necking which is characteristic for ductile materials. Consequently, a small RA is correlated to rather brittle materials. An advantage of investigating this parameter lies in its simple determination.

When comparing the RA of a hydrogen charged sample with a specimen tested in air, Hoover et al. [49] noticed that hydrogen reduces the RA, hinting at a brittle behaviour. When now comparing the RA of samples strained with and without hydrogen of the same material, the RA is about 50 % less in presence of hydrogen than the RA of equivalent specimens tested in air [49].

Fracture surface examination

With the help of surface examination also the ductility of materials can be determined. This investigation can further characterize the failure mode of the sample as a simple measure of the RA. The examination of the fracture surface of tensile specimens can give additional clues on hydrogen embrittlement.

Hoover et al. [49] investigated different low carbon steels and detected surface cracks on all samples strained within a hydrogen gas atmosphere, but the depth of material penetration differed. For the A-516 steel, no deep cracks could be recognized, whereas a complete penetration of the material was discovered for a girth welded A-106 steel. The hydrogen induced flat fracture varied from material to material. Flat fracture has the same meaning as quasi cleavage on macroscale. This term refers to a fracture surface morphology with flat areas indicating brittle failure and thus the absence of dimples which indicate ductile, plastic failure.

For low carbon steels, a general trend was noticed: The greater the post necking strain and the smaller the final fracture stress of a material, the greater is the amount of hydrogen induced flat fracture surfaces [49]. This implies that low strength materials which naturally can bear rather large plastic deformations show a quantitatively higher embrittlement effect than high strength steels. However, high strength steels in turn can generally not bear as much plastic deformations as the low strength steels. Therefore, even a slight increase (caused by hydrogen) of the anyway brittle material behaviour of high strength steels can lead to a fatale collapse of structures.

In a further fracture surface investigation, Merson et al. [50] found cracks surrounded by brittle failed material. These so called "fisheyes" were only present for samples tested in a hydrogen atmosphere and are marked in Figure 3.3.

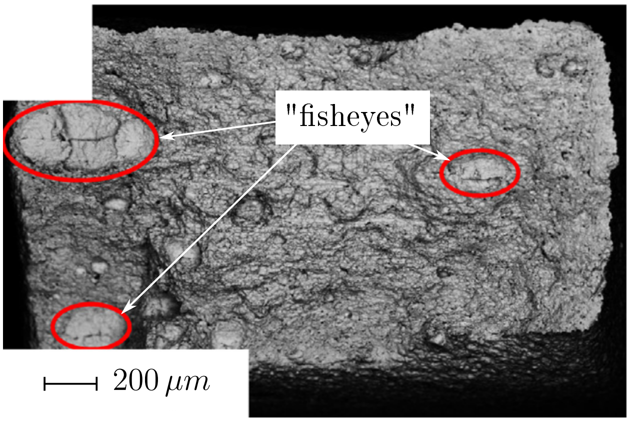

Figure 3.3.: Fracture surface of a S235 tensile specimen with the scanning electron microscope (SEM) at a charging current density of 170 mA/cm^2 [50]

In order to gain more insight on how and at which loading state the fisheyes were formed, the sample was loaded with hydrogen and subsequently unloaded by a heating procedure [50]. In this case, no fisheye defects were recognized and the original ductility was reached. Still, cracks could be detected which were not present in all samples never charged with hydrogen. Therefore, the cracks seem to originate from cathodic charging while the brittle areas of the fisheyes were formed during tensile loading in case of hydrogen charged samples. Thus, the hydrogen could enter the material over the crack surfaces and showed to embrittle the material in the vicinity of these defects.

In an additional study of visually examining the fracture surface of tensile specimens at high strain rates of 0.55 s^{-1}, Moro et al. [52] discovered that only an outer ring of the surface showed brittle failure while the rest remains in a ductile failure mode. About 90 % of the total fracture surface showed a ductile failure mode. Due to the high strain rate, the hydrogen gas, which surrounded the specimen while straining, could not be transported fast enough inside the material to cause brittle failure over the whole profile. This effect of the strain rate will be discussed in more detail in chapter 3.2.3. In the case of the precharged samples of Merson et al. [50], it would have been interesting to investigate the surface of a specimen at the same level of strain rate to examine the size of the brittle area caused by internal hydrogen.

A constant dislocation density over several grains inside the pipeline material X60 and X80 was discovered by Martin et al. [53]. This constant gradient of dislocation density gives hints of the actual underlying mechanism leading to hydrogen embrittlement. This will be discussed in detail in chapter 3.3.

To conclude, the behaviour of tensile test specimens in the presence of hydrogen was presented. For smooth samples, a brittle effect due to hydrogen could be determined after reaching the UTS, concurring with surface crack formations. Notched samples show a more pronounced embrittlement effect when exposed to hydrogen due to the more localized stress and strain fields at the notches, causing a promotion of hydrogen accumulation. These results highlight that hydrogen embrittlement gets more critical in presence of local defects.

While using the RA only the general embrittlement of the specimen can be described, surface observations can yield more insight on the hydrogen embrittlement process. A material strength dependency on the amount of softening as well as a local embrittlement around initiated cracks could be shown. Furthermore, the effect of an increasing strain rate on the embrittled material and the observed dislocation density lead to a better understanding of the hydrogen embrittlement process.

All observations from tensile testing given above were presented to give the reader a general overview of hydrogen embrittlement. The importance of the different observations are put into a more detailed context in the following chapters to derive important modelling parameters.

3.2.2. Experimental conditions affecting hydrogen embrittlement

Previously, an overview of the general impact of hydrogen on tensile testing was discussed. In a next step, the influence of varying testing conditions shall be examined. On the one hand, the influence of two available charging techniques, which are mainly used in literature, are examined. On the other hand, the effect of the presence of hydrogen gas in different stages of tensile straining is reviewed.

Charging technique

For introducing hydrogen into a specimen, two different procedures exist: charging in a pressurized gas cell or cathodically. Both charging techniques can introduce a comparable amount of hydrogen, what Lam et al. [47] showed in an overview paper for a flat, double notched tensile specimen. Apart from the charging technique, the exact same test environment was used [54, 47]. The tensile test results of a specimen charged cathodically by a current density of $2.5\,mA/cm^2$ and a specimen charged within a hydrogen gas atmosphere of $21\,MPa$ are essentially the same with regard to the fracture behaviour and the morphology of the fracture surface.

However, there is one difference between these two charging techniques: Introducing hydrogen by cathodical charging is more aggressive and can introduce damage to the material especially for high current densities. As already briefly discussed in chapter 3.2.1, Merson et al. [50] examined that once the hydrogen content is removed by a heating procedure from an cathodically charged tensile specimen at a current density of $170\,mA/cm^2$, the same ductility can be recovered. Nevertheless, once specimens were charged with hydrogen, cracks appeared at the fracture surface which were not monitored in non-charged samples. Merson et al. concluded that these cracks were introduced while charging the specimen cathodically [50].

According to the discussion above, comparable amounts of hydrogen embrittlement could be observed for chathodical charged samples and specimens tested in a high gas pressure cell. Nevertheless, cracks are induced by the cathodic charging technique at high current densities.

Influence of charging chronology in hydrogen atmosphere

Another factor which influences experimental results is the chronological order of the hydrogen charging procedure. A hydrogen concentration can be introduced before testing or while testing (in-situ testing). According to literature, both charging techniques are used to induce hydrogen in a specimen. For specimens, which were loaded before testing, a decreasing hydrogen content can be observed at the surface. This surface concentration was determined to about half of the one in the bulk material [8]. For in-situ charged specimens, the contrary occurs: At the surface of the specimen, a high hydrogen concentration can be detected which is decreasing to the center of the specimen until a constant distribution is reached. Thus, the hydrogen atmosphere within a specimen varies, dependent even on the process used to charge the sample with hydrogen. Nevertheless, both procedures in general can lead to a pronounced embrittlement.

In order to get a better understanding in which state of tensile testing the hydrogen is influencing the material properties, three tests conducted by Moro et al. [52] are reviewed in the following.

The tensile tests were performed in a pressure cell with hydrogen gas and nitrogen gas as an inert environment. It was monitored that the nitrogen gas does not change the fracture behaviour of the investigated high strength low carbon pipeline steel X80. A strain rate of $5\ 10^{-5}\,s^{-1}$ has been applied at room temperature.

In the first test scenario the notched specimens are charged for $60\,min$ at an hydrogen pressure of $30\,MPa$ in advance of testing and then strained at the same hydrogen pressure. The tensile test was interrupted shortly before the fracture would occur for specimens exposed to a $30\,MPa$ hydrogen pressure until failure (see Figure 3.4, black cross). The hydrogen within the cell was replaced by $0.2\,MPa$ nitrogen (over the course of $8\,min$), after which the specimen was strained until failure. The results imply that the fracture strain is surprisingly ductile.

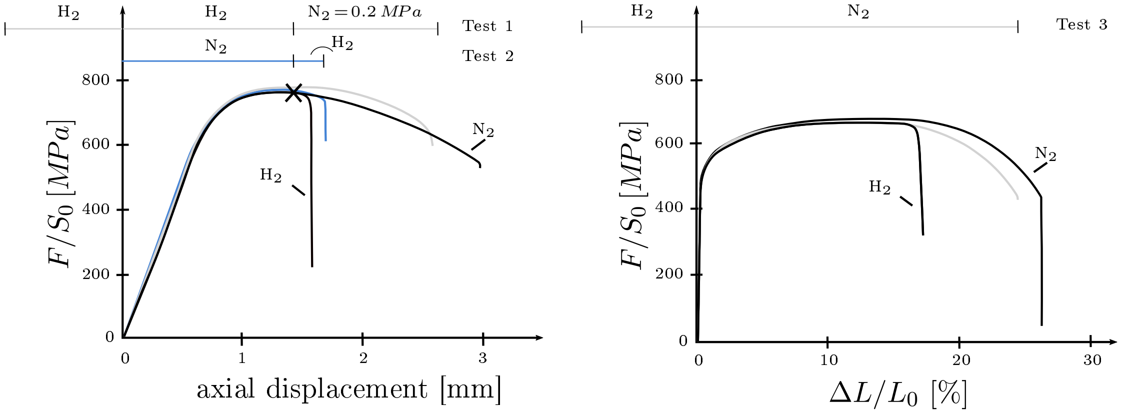

Figure 3.4.: Stress-strain curves from tensile tests using a notched specimen, left, and a smooth specimen, right. The tests were conducted in a high pressure cell with a X80 pipeline steel specimens. The hydrogen gas application phase is marked by H_2, while a nitrogen gas atmosphere is marked with N_2. The gas pressures are $30\,MPa$, if not marked differently (compare Moro et al. [52]).

In order to understand this ductile behaviour of test 1, a second test scenario was discussed [52]. In a first step, the specimen is strained in $30\,MPa$ nitrogen gas again until the point where almost brittle failure occurs for a specimen tested in a hydrogen gas atmosphere. This point is marked in Figure 3.4 by a black cross. Then, the nitrogen gas was replaced by hydrogen and the specimen was strained until failure. The failure mode shows to be brittle, even when the specimen was exposed to hydrogen only for a short time period (compare Figure 3.4, blue line).

In test 1, the specimens were exposed to a hydrogen gas atmosphere over a total of one hour, whereas in test 2 only for eight minutes a hydrogen gas atmosphere was present in the experimental environment. This leads to the finding that hydrogen is transferring the failure mode from ductile to brittle only if hydrogen is present during necking and thus crack initiation. It is concluded that the occurring surface cracks during necking provide advantageous hydrogen uptake surfaces. Thus, embrittlement only occurs when the specimen is surrounded by hydrogen gas during this stage. This is in agreement with the surface cracks observed by Hoover et al. [49] (compare chapter 3.2.1).

In a third test, a tensile specimen was loaded before testing within 30 MPa hydrogen gas and then strained until failure in a nitrogen atmosphere. When comparing the value of the UTS to the one of test 1 and test 2, a decrease can be recognized. This is caused by a reduced value of the cross section S_0. Moro et al. referred to this specimen as notched one. Nevertheless, the used tensile specimen has only a reduced cross section, but no sharper notch as in the sketch of Figure 3.2, top right. Thus, in this context, this specimen is referred to as smooth, which is also supported by the typical results of the stress strain curve in Figure 3.4 for smooth tensile specimen. However, in case of test 3, the authors state that no brittle behaviour could be noticed as the results lie within the scatter of the test results (compare Figure 3.4, right).

The result of test 3 of Moro et al. [52] is in contrast to the findings of Merson et al. [50], who could observe a pronounced embrittlement of tensile specimens charged electrolytically before straining for 60 minutes at a current density of 170 mA/cm^2. This flat tensile specimen was tested 5 min after charging. Thus, in the case of the tests within the pressure cell by Moro et al. [52], a surface layer could prevent the hydrogen uptake during the charging process of test 3. Nevertheless, the authors stated that they took actions to prevent the creation of such a surface layer. Another explanation would be that the time of one hour, in which the specimen was exposed to the hydrogen atmosphere, was too short or the hydrogen pressure was not large enough to introduce a sufficient hydrogen content into the specimen.

In order to explain these diverging results of Moro et al. and Merson et al., the applied current density needs to be related to the hydrogen gas pressure. In the previous paragraph, when discussing the charging techniques, it was stated that a current density of 2.5 mA/cm^2 could be related to a pressure of 21 MPa [54, 47]. The current density used by Merson et al. is 68-times larger than the one related to a gas pressure of 21 MPa. It should be noted that the results cannot be simply linearly extrapolated due to different test environments and since no further information on the coupling behaviour of the charging current density and the hydrogen pressure is available. Nevertheless, it can be concluded that the hydrogen gas pressure which is needed to result in the same embrittlement behaviour as for a current density of 170 mA/cm^2 has to be extensively larger than the aforementioned 21 MPa. Judging from the different grades of hydrogen embrittlement, the hydrogen pressure also needs to be larger than the 30 MPa investigated by Moro et al. [52]. Thus, the reason for the different observed effects can be found in the different charging techniques. The cathodical charging technique used by Merson et al. introduces a higher amount of hydrogen atoms in the same time than specimens charged within a pressurized gas cell by 30 MPa.

It can be concluded that for samples charged with hydrogen before straining, the amount of introduced hydrogen needs to be rather large in order to embrittle the material. These high required internal hydrogen populations seem not to be practically attainable in case of charging the specimen within a pressurized hydrogen gas atmosphere. Since in the natural gas pipeline system the hydrogen would be present in form of gas, one important fact of hydrogen entering the material can be derived: If hydrogen gas is present in a tube, the influence of hydrogen is pronounced in the case of crack initiation or crack propagation. Then, the uptake of hydrogen is rather rapid over the new surfaces and causes a fatal brittle failure mode.

3.2.3. Characterization of major parameters affecting hydrogen embrittlement

Previously the effect of hydrogen was discussed in general for uniaxial tensile tests and experimental factors like charging techniques as well as the importance of the presence of hydrogen availability during tensile straining were discussed. Here, the influence of different parameters on the amount of hydrogen embrittlement are analysed, namely the hydrogen content, the material strength level, welding and the strain rate. The importance of including these parameters in the actual numerical model are discussed.

Hydrogen content

In Figure 3.5, the relationship of hydrogen pressure within a high pressure gas cell and the according fracture strain of an in-situ tensile test is depicted for different low carbon steels. It should be noted that the strain rate as well as the experimental procedure might vary since the experiments were performed by different research groups. Therefore, the results can only be qualitatively compared. The results of Moro et al. [52] show a dotted line between 5 and 30 MPa, indicating that in between these pressures, the authors stated that the fracture elongation is constant without mentioning the exact relation between hydrogen pressure and fracture strain. The scattering of the results is marked, if available.

For all the tests depicted in Figure 3.5, the same trend can be observed. The higher the hydrogen pressure is within the test cell, the higher the hydrogen induced reduction of fracture strain is until a minimum of fracture strain and thus a maximum of embrittlement is reached. After reaching this plateau, any further increase of the hydrogen pressure within the cell does not lead to a pronounced further embrittlement.
It should be noted that already small hydrogen pressures of 0.1 MPa show to reduce the fracture strain. Therefore, even the general presence of hydrogen already induces a brittle behaviour. From those low pressures on, a decreasing non-linear fracture strain with increasing hydrogen pressure can be observed until a plateau is reached.
These results imply that a maximum of hydrogen embrittlement in a material is attainable.

Material strength dependency

Another factor influencing the amount of hydrogen embrittlement is the material strength level. Hardie et al. [56] investigated the effect of the material strength level by comparing the pipeline steels X60, X80 and X100 under tensile straining and cathodic polarization charging at 40 $℃$. The reduction of fracture area (RA) was investigated as a measure of embrittlement. For a current density of 0.44 mA the same RA for all tested steels could be detected. However, when applying a higher current density of 0.66 mA, an enhanced embrittlement with increasing strength level was recognized.

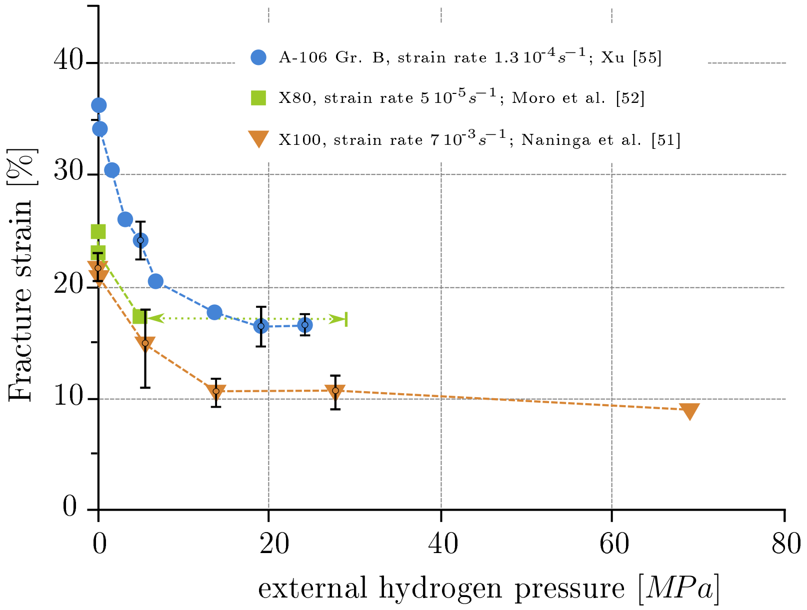

Figure 3.5.: Fracture strain in relation to the hydrogen pressure within a high pressure gas cell for different materials and strain rates; The dotted line for X80 steel denotes that Moro et al. [52] solely stated that in this domain of hydrogen concentration, the fracture strain is considered as constant.

Nanninga et al. [51] also examined an increase of hydrogen embrittlement with alloy strength by examining the steels X52, X65 and X100 under tensile straining. When examining the surface, the number of micro cracks increased with the material strength level, which in turn correlates with an increase in hydrogen embrittlement.

Furthermore, Hoover et al. [49] stated that for the investigated pipeline materials, high strength low carbon steels tolerate very little plastic localized strain in the presence of hydrogen, as discussed in chapter 3.2.1. This can be attributed to their in general limited toleration of plastic deformation even without hydrogen. Thus, in case of high strength steels the embrittlement is more critical.

Hardie et al. [56] pointed out that the dependence on strength level seems to correlate with the applied current density and thus the available hydrogen concentration. Therefore, a threshold for the hydrogen concentration is suspected at which the material strength dependence can be observed. Unfortunately, the current density cannot be directly linked to the hydrogen pressure and no lower bound can be identified. It can only be stated that at hydrogen pressures of 6.9 MPa [49] and 13.8 MPa [51], a strength level dependent effect could be discovered.

Welded samples

Parfene at el. [57] examined the influence of welds on hydrogen induced embrittlement by Charpy Impact testing. The welding procedure itself introduced an hydrogen atmosphere in the specimen. For a low carbon steel S235JR, an increase of embrittlement was detected when using girth welded as well as seam welded base materials. The amount of introduced hydrogen, using manual arc welding, is in this case higher than the hydrogen introduced by charging the base material electrolytically for 30 hours. Unfortunately, the charging current density was not reported. The contrary was stated by Hoover et al. [49]: For seam and girth welded low carbon steels the same amount of reduction of area was detected as for the base material.

To include the influence of welds in numerical models mainly three driving parameters can be identified: The local change of strength level in the weld, thermal eigenstrains and an additionally induced hydrogen atmosphere during the welding process. Nevertheless, the experimental results are contradictory. Since no effect on welds could be determined when tests were realized in a hydrogen gas atmosphere, and in the pipeline system hydrogen would be ducted through in form of gas, welds are not considered within this work.

Strain rate

Merson et al. [50] examined the influence of the applied strain rate on a tensile specimen of low carbon steel S235JR which was electrolytically precharged with hydrogen. In Figure 3.6, left, the relationship of the fracture strain to the strain rate is plotted for different charging current densities and thus varying internal hydrogen concentrations. For specimens not charged with hydrogen, the fracture strain is slightly decreasing for higher strain rates. Nevertheless this slight decreasing tendency lies in the scattering of the experimental results and can be interpreted as constant.

When examining the results of hydrogen charged samples, a clear dependence on the strain rate is observed. For low strain rates of $10^{-4}\,s^{-1}$ the fracture strain decreases significantly which implies a high hydrogen induced embrittlement. In the case of higher strain rates of $10^{-1}\,s^{-1}$, the induced hydrogen has almost no effect on the fracture strain. This is due to the fact that at these high strain rates, the hydrogen in the specimen does not have enough time to redistribute and accumulate at critical places, like for example at stress peaks in the vicinity of crack tips. Thus, the hydrogen cannot effectively embrittle the material. If the hydrogen concentration is increased within the specimen by applying a higher charging current density, the embrittlement gets more pronounced considering the same strain rate.

Similar results were obtained by Moro et al. [52]. Besides the three tests discussed above in chapter 3.2.2, they examined tensile specimens of high strength low carbon steel X80 within a constant hydrogen atmosphere for various strain rates. The results are extracted from stress-strain curves and are depicted in Figure 3.6, right. The results in nitrogen environment imply a slightly increasing fracture strain with increasing strain rate, but the provided amount of tests is not large enough to justify direct conclusions. However, a clear dependency on the strain rate for specimens tested in a $30\,MPa$ hydrogen atmosphere is noticed. The higher the strain rate, the lower the embrittlement due to hydrogen shows to be.

Nanninga et al. [51] reported no clear dependency on the strain rate for a high strength low carbon steel X100. The test was transduced in-situ at a hydrogen pressure of $13.8\,MPa$. For strain rates from $10^{-5}\,s^{-1}$ to $10^{-2}\,s^{-1}$, only a slight increase of ductility with rising strain rate could be observed. This increase was judged as not significant compared to the scattering of test results. It was concluded that in this case the strain rate has only a little influence on the amount of embrittlement. It should be noted that the hydrogen gas atmosphere while testing is less than half of the pressure that was used for in-situ testing by Moro et al. [52]. Furthermore, Merson et al. [50] recognized that for higher hydrogen concentrations the dependency on the strain rate is more pronounced.

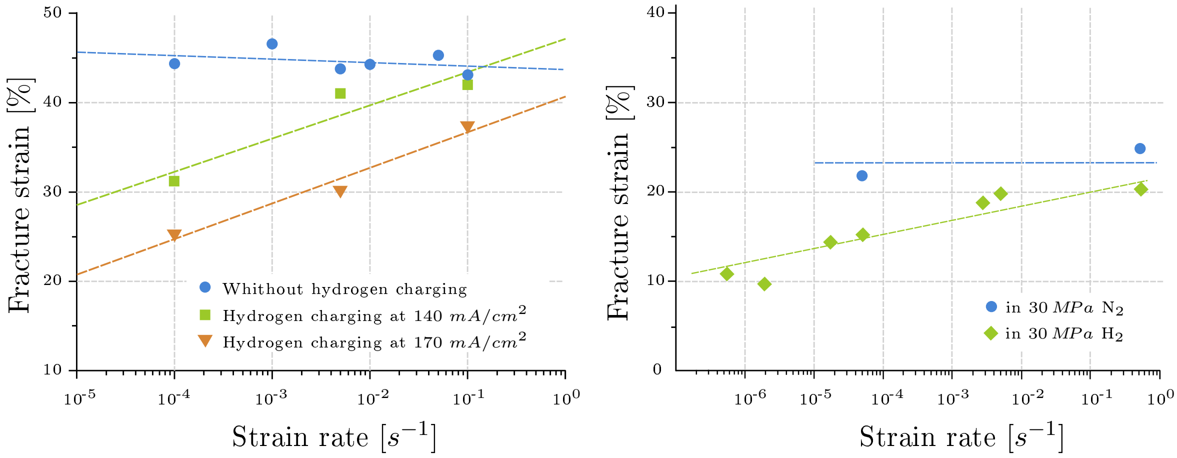

Figure 3.6.: Fracture strain over strain rate of uniaxial tensile tests with smooth specimens; tests conducted in air after electrolytically charging the specimens of low carbon steel S235JR with different current densities, reproduced from [50] (left); tests conducted in a high pressure cell with specimens made of X80 steel, data reproduced from [52] (right)

Thus, the two contradictory observations of the influence of the strain rate on the amount of hydrogen embrittlement can again be explained by two different hydrogen concentrations within the material.

It can be concluded that the dependency of hydrogen embrittlement on the strain rate is influenced by the local hydrogen concentration or moreover the availability of hydrogen. In the pipeline system only small pressure changes are expected and thus the present strain rate is rather small. Therefore, the effect of strain rate does not have to be considered when modelling the pipeline system.

3.2.4. Identification of essential parameters for numerical modelling

In the previous chapters, an overview of the conditions in a natural gas pipeline system as well as an analysis of experimental findings was given. Furthermore, the influence of the environmental conditions during testing on the amount of hydrogen embrittlement were presented.

Four parameters were discussed in chapter 3.2.3 which influence the amount of hydrogen embrittlement, namely the hydrogen content, the material strength dependency, welded samples as well as the strain rate. In the following, these parameters are discussed regarding their importance when investigating gas pipeline systems.

The most important parameter in case of the investigated gas pipeline structures is the hydrogen gas pressure within the tube. With rising gas pressure, the brittle effect of hydrogen increases. Firstly, this parameter obviously has to be considered in the mechanical model by including pressure boundary conditions. Secondly, the gas pressure needs to be related to a surface hydrogen concentration as boundary condition of a hydrogen distribution model, since the amount of hydrogen which can enter into the material lattice directly depends on the surrounding gas pressure.

The material strength dependent on increased hydrogen embrittlement can be interpreted as a material dependent parameter, which modifies the amount of hydrogen embrittlement in mechanical modelling. It should be kept in mind that for lower hydrogen pressures, the effect of the material strength can be neglected, while a lower bound of hydrogen pressure could not clearly be determine.

Since the tubes of the pipeline system have weld lines, the influence of welds on the amount of hydrogen embrittlement is also an interesting parameter. Welded samples, which were tested in hydrogen atmosphere, did not show a more pronounced embrittlement than specimens without welds. Thus, at this point in time, this parameter is not further investigated.

The influence of the strain rate can be neglected within the pipeline systems, since only minor changes in pressures are expected in the tubes.

All in all, two primal parameters could be identified to influence the grade of hydrogen embrittlement in a natural gas pipeline system. The hydrogen gas pressure in the tube and the material strength level.

In a next step, a short excurse to experimental findings on meso length scale shall be given. Understanding these underlying material processes simplifies the subsequent interpretation of macroscale experimental results as well as the underlying hydrogen embrittlement mechanism.

3.2.5. Changes in grid dislocation amount and behaviour

Up to this point, the focus of discussion was put on the macroscopic effect of hydrogen on the material in form of tensile testing. In the following paragraph, a more detailed look at experimental findings on the mesoscale is presented. The fundamental description of dislocation behaviour and its continuum mechanical interpretation can be found in chapter 2.2.

In order to test the influence of hydrogen on the dislocation mobility, Robertson et al. [58] used electron thinned foils under tensile loading conditions and utilized a transmission electron microscope to observe the dislocation behaviour. Two types of experiments were conducted by in-situ testing with hydrogen gas pressures of up to $20\,kPa$.

In a first test electron thinned foils were stretched so that the dislocations started to move. When hydrogen gas was introduced, a higher velocity of the dislocations could be recognized. By removing the hydrogen gas atmosphere, the original velocity was recovered.

For the second test hydrogen gas was introduced to a thinned foil at a constantly applied force with stationary dislocations. When introducing the hydrogen atmosphere, these dislocations started to move.

According to the two tests, it can be concluded that hydrogen speeds up dislocations motion as well as that dislocations start moving at lower stress levels. It is interesting to note that this however is not dependent on the material structure or dislocation type. Robertson et al. [58] were able to examine that it rather depends on the hydrogen gas pressure as well as the purity of the material.

For a higher carbon level in Fe-steel, a decreasing dislocation velocity has been observed [59]. This effect was traced back to the fact that carbon acts as an impurity in the material and impedes the dislocation motion. Thus, the dislocation velocity was observed to depend on the material purity.

It could be argued that this enhanced dislocation motion is due to the fact of introducing a gas pressure around the thin foil. This could be disconfirmed by using a dry inert gas [58]. Here, an increase in dislocation motion according to the induced pressure could be detected for some seconds before steady state conditions were reached. The effect of hydrogen gas on the dislocation mobility noticeable exceeded this time frame.

However, the general effect of hydrogen enhancing the mobility of dislocations could be observed for numerous materials, pure metals and alloys. Robertson et al. concluded that this effect is therefore independent from the crystal structure [59, 58]. Additionally, an enhanced production of dislocations has been monitored and thus the actual number of dislocation increased in the plastic regions.

Furthermore, an increasing slip planarity in the presence of hydrogen has been determined by nanoindentation for nickel [8, 7]. A further observed effect of hydrogen is a reduction of the dislocation pile up distance at a grain boundary for the 310SS steel [59].

A discussion and interpretation of the observed effects described above can be found in chapter 3.3.

3.3. General mechanisms for describing hydrogen embrittlement phenomena

According to the conclusion of chapter 3.1, the critical sections of pipeline systems are the already damaged ones. Consequently, all mechanisms are explained at the example of a crack and its propagation.

The stress state of a blunted crack is well known from fracture mechanics [32, 60]. The maximal hydrostatic stresses are located shortly ahead of the crack tip. This means that here the material is strained volumetrically. At this strained region, hydrogen accumulates easily due to the additional spacing between the host lattice molecules. Thus, the hydrogen present within the material or the one entering through the material surface accumulates in front of a crack tip [21, 15]. In the following, this effect is schematically depicted for all mechanisms indicated by arrows for the moving direction of the hydrogen.

Generally the mechanisms of hydrogen embrittlement can be distinguished in two main groups; in materials where the host lattice of the material reacts with hydrogen to a brittle hydride and in materials which do not form hydride.

3.3.1. Materials exhibiting hydride forming under hydrogen influence

In hydride forming materials, like Titanium (Ta), Vanadium (V) and Zirconium (Zr), the mechanism of hydride embrittlement is active. This mechanism includes that the accumulated hydrogen at the crack tip nucleates with the host material and forms a brittle hydride like depicted in Figure 3.7. The crack propagates, when a critical size of the hydride is reached and cleavage occurs. The crack stops at the interface of the hydride until enough hydrogen is diffused again to the crack tip to form the brittle hydride [61]. This mechanism could be clearly shown for hydride forming materials within several experiments [62, 63].

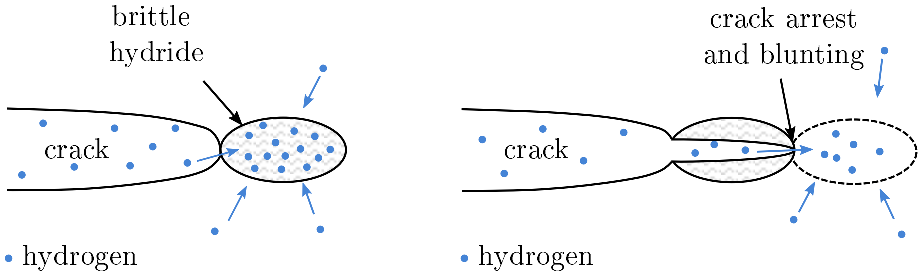

Figure 3.7.: Scheme of hydride embrittlement mechanism. The dots, which mark the hydrogen, should only give a broad idea where hydrogen is accumulated (adapted from [64]).

3.3.2. Materials with no hydride forming under hydrogen influence

For non-hydride forming materials, different mechanisms are discussed in the scientific community [58, 61, 64, 65]. The Hydrogen Enhanced Decohesion (HEDE) mechanism, the Hydrogen Enhanced Localized Plasticity (HELP) mechanism and the Adsorption Induced Dislocation Emission (AIDE) mechanism. These mechanisms are discussed in greater detail, since the pipeline system is constructed out of non-hydride forming materials.

HEDE

The Hydrogen Enhanced Decohesion (HEDE) mechanism assumes that accumulated hydrogen lowers the cohesive strength between atoms within the host lattice. At atomic sharp crack tips the adsorbed hydrogen lowers the cohesive strength of the atoms and therefore the crack can propagate at lower stress levels like schematically depicted in Figure 3.8. Furthermore the hydrogen is assumed to lower the atomic bonds inside the lattice, as a result of the accumulated hydrogen in a short distance ahead of a crack tip. Here voids start to form and these voids enhance the brittle crack propagation. According to this HEDE mechanism a tensile separation of the atoms is favored compared to plastic effects as slip [61].

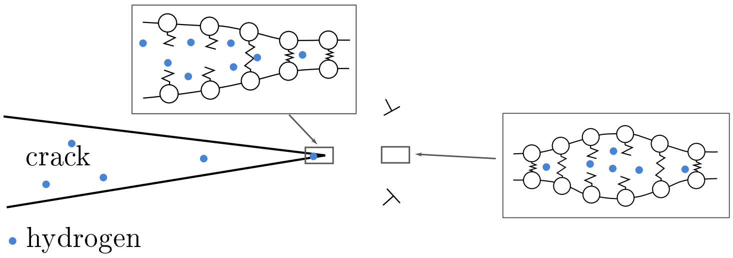

Figure 3.8.: Scheme of HEDE mechanism. The dots, which mark the hydrogen, should only give a broad idea where hydrogen is accumulated (adapted from [64]).

HELP

The Hydrogen Enhanced Localized Plasticity (HELP) mechanism assumes that the presence of hydrogen shields dislocation or obstacles from each other by changing the local stress field. This local refinement of the stress field enables the dislocations to move at lower stresses, which leads to a more localized plastic zone as depicted in Figure 3.9. Furthermore, this more localized plasticity in turn leads to a more localized formation of micro voids. This local softening by enhancing the plastic effects in front of the crack tip leads to a sudden brittle crack propagation which appears like brittle failure on macroscale.

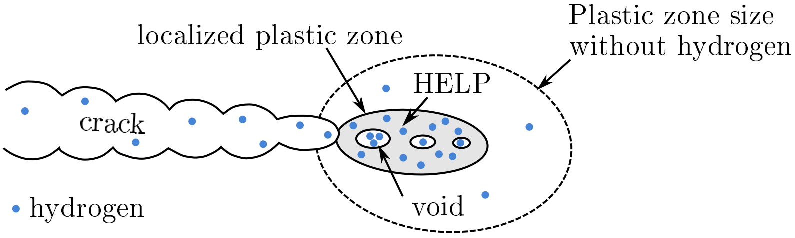

Figure 3.9.: Scheme of HELP mechanism. The dots, which mark the hydrogen, should only give a broad idea where hydrogen is accumulated (adapted from [64]).

AIDE

The fundamentals of the HEDE mechanism are adapted in a more complex manner to formulate the Adsorption Induced Dislocation Emission (AIDE) mechanism. It is assumed that hydrogen is adsorbed at the material surface and reduces here the atomic bounds like in the HEDE mechanism. This leads to a facilitated nucleation of dislocation cores within the surface layers by sheering processes. This dislocation cores can be emitted to the inner of the material at sufficient stress levels, forming dislocation bands like depicted in Figure 3.10. The dislocations are considered to drag the hydrogen atoms inside the material. In front of the crack tip voids form, enhanced by the accumulated hydrogen. The facilitated emission of dislocation cores from the surface as well as the void formation in front of the crack tip lead to a brittle crack propagation on macroscopic scale.

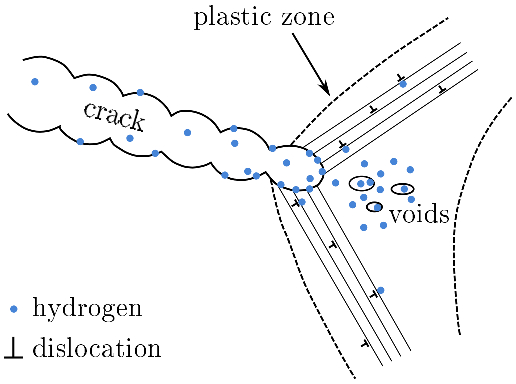

Figure 3.10.: Scheme of AIDE mechanism. The dots, which mark the hydrogen, should only give a broad idea where hydrogen is accumulated (adapted from [64]).

Concept on atomic length scale

The three mechanisms for non-hydride forming materials described above depict the embrittlement effect of hydrogen in front of a crack tip. It is commonly agreed in literature that all three mechanisms act simultaniously within a material, while one mechnism is the dominant one [15, 65, 66, 67]. The determination of the active mechanism directly from the macroscopic results discussed in chapter 3.2 is rather difficult. Therefore, the experiments on the meso length scale are more promising to identify the dominant mechanism. Based on these results, the behaviour of hydrogen on meso length scale is described in the following while the actual evaluation of the mechanisms shall be discussed in chapter 3.3.3. The basic link of the micro-structure and the continuum mechanical interpretation is fundamentally summarized in chapter 2.2.

The description of hydrogen behaviour in the following is based on the work of Robertson et al. [58]. According to the experimental findings, hydrogen is on the one hand enhancing the number of dislocations and on the other hand lowers the stress levels at which the dislocations begin to move (compare chapter 3.2.5). Furthermore an increasing of the moving velocity could be detected. This observation can be explained by hydrogen accumulating at the local stress fields of dislocations. Here, the hydrogen locally modifies the stress field and enables the dislocations to move at lower stress levels. Since a constantly enhanced dislocation motion can be observed in the presence of hydrogen, Robertson et al. [58] concluded that the dislocations carry the hydrogen atmosphere with them. A schematic representation of this effect is depicted in Figure 3.11, A. When the material is strained, the dislocations move at lower stress levels, implying a higher velocity and dragging the hydrogen with them.

This concept of dislocations dragging the hydrogen atoms with them naturally explains the dependency on the strain rate. If the dislocations move too fast, the hydrogen atmosphere cannot be dragged with the dislocations anymore and the hydrogen atoms start breaking away from the dislocation cores. In this case, the hydrogen just acts as an impeding impurity for dislocation motion within the material.

The hydrogen concentration being dragged with the dislocations also gives an explanation for limited cross slip [58]. In case the dislocations change to an alternative slip plane, the bounded hydrogen atmosphere needs to be redistributed. Thus, in the case of cross-slip, an additional force would be needed to drive this redistribution compared to a system without hydrogen. In other words, more energy would be needed in a system with hydrogen compared to one without hydrogen to generate a change in the slip plane. Since no additional driving force is present in a material exposed to hydrogen, less cross-slip can take place and thus the slip-planarity increases [58].

Since hydrogen is assumed to alter the local stress field, also the dislocation interaction with a grain boundary is influenced. In case a dislocation which carries hydrogen reaches a grain boundary, a reduction in the pile-up distance of dislocations can be recognized compared to a system without hydrogen [59].

Furthermore, the grain boundaries in general can include dislocations as well as send dislocations out into another neighbouring grain (compare chapter 2.2). In case dislocations drag hydrogen with them and enter a grain boundary, the hydrogen atmosphere accumulates here due to its higher binding energy. Thus, the grain boundary acts as a sink. In Figure 3.11, B, a schematic representation of this effect is illustrated. First, all hydrogen carried by dislocations entering the grain boundary is bound here until the sink is filled

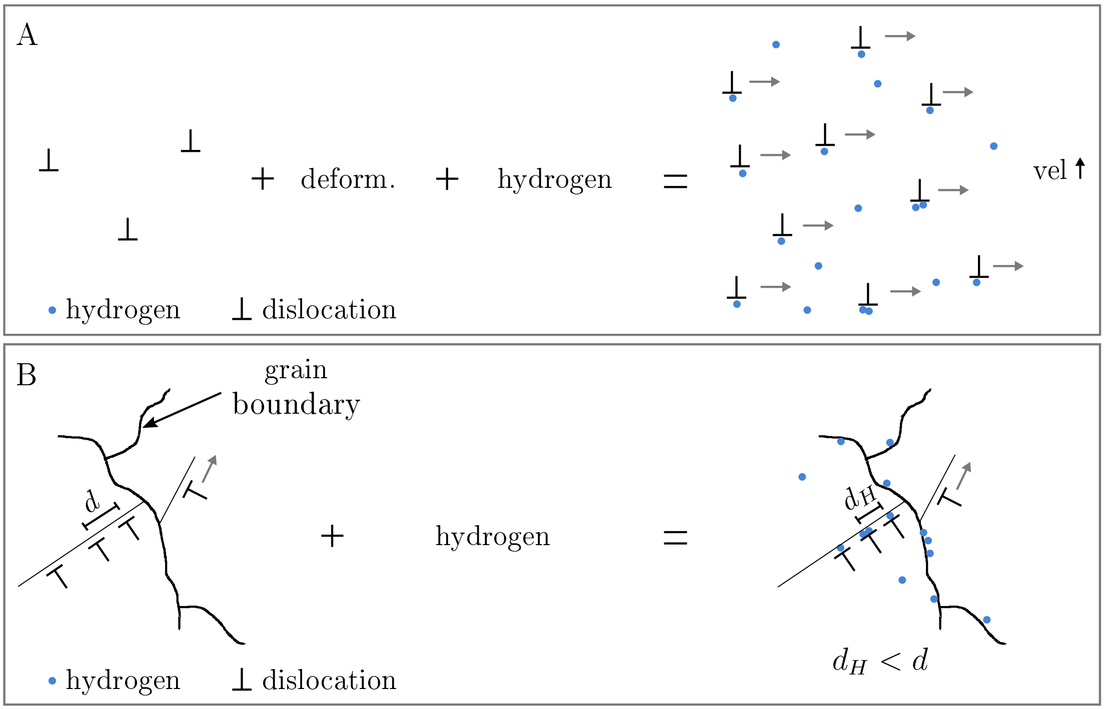

Figure 3.11.: Schematic representation of the effect of hydrogen on the dislocation behaviour: Dislocations drag the hydrogen atmosphere with them and increase the number as well as the velocity of the moving dislocation compared to a system without hydrogen (A). In the presence of hydrogen, the pile-up distance of dislocations at grain boundaries is decreased and hydrogen is accumulated at the grain boundary (B).

and thus no further hydrogen can be hold within the grain boundary. Then, also the out sending dislocations can drag a hydrogen atmosphere with them. The accumulated hydrogen is changing the local stress state at the grain boundary and provides an explanation for several observed intergranular failure cases [58].
The experimentally observed increased number of dislocations consequently leads to an increasing interaction with grain boundaries. The more dislocations enter the grain boundary, the more disorder is generated.
Beside the influence of hydrogen on the material properties, also the importance of hydrogen transport by the dislocations shall be discussed. If hydrogen transport would be primarily governed by the dislocation motion, embrittlement should be enhanced with increasing strain rate. This is because with increasing strain rate, the dislocations would move faster and thus quickly distribute the hydrogen within the specimen. Nevertheless, there is an upper bound of velocity where the hydrogen gets debounded from the dislocation core. Detailed information of modelling this way of hydrogen transport by a dislocation sweeping model can be found in [68, 69].
However, the investigated pipeline steel shows a decreasing embrittlement with increasing strain rate. Thus, the movement and distribution of hydrogen is not dominated by dislocation transport in the prevalent case. Moreover, it seems that the hydrogen distribution is governed by the mechanical stress and strain field as broadly described in the beginning of chapter 3.3. Nevertheless, a hydrogen atmosphere bound to the dislocation cores still alters the stress state and increases the dislocation density as discussed above.

Solely the transportation of hydrogen via dislocation as a primal hydrogen distribution model is discarded.

The discussed effect of hydrogen on the dislocation behaviour can be phenomenologically transferred to a continuum approach. In continuum mechanics, the micro-mechanically observed dislocations are accounted for by plastic straining (compare chapter 2.2). Since the dislocations move at lower stress levels and a higher density is observed in the presence of hydrogen, the continuum mechanical parameter of the plastic strain could be accumulated at lower stress states. Thus, in total, more plastic strain is accumulated than in the absence of hydrogen. Since the HEDE mechanism excludes dominant plastic effects, this interpretation of the experimental results leads to the assumption that either the HELP or the AIDE mechanism is active in the prevalent case.

The surface examination of a tensile test specimen of Martin et al. [53] supports the effect discussed above. A constant dislocation density over several grains from the crack surface could be detected (compare chapter 3.2). This can be explained by the enhanced plastic processes discussed above. Martin et al. concluded that in case the AIDE mechanism would be active, a gradient of the dislocation density should be present from the crack surface to the inside of the bulk material, since the dislocations are assumed to be emitted from the surface. The authors concluded that the AIDE mechanism is not likely to be active and favoured the HELP mechanism. Nevertheless, Lynch [70] stated that the expected gradient of dislocations according to the AIDE mechanism could not be separated from the high plastic processes at the crack surface. Thus, the observed constant dislocation density does not directly discard the AIDE mechanism. For a single crystal of Fe-Si alloy, a decreasing dislocation density with distance to the crack surface could be observed under fatigue loading conditions [71, 72, 73]. Therefore, a dominant mechanism cannot be finally identified in this chapter.

It is concluded that in the presence of hydrogen, dislocations move at lower stress levels which can be related in a continuum mechanical sense to an accumulation of plastic strain at lower stress levels. This is in agreement with the HELP as well as the AIDE mechanism. Furthermore, it could be demonstrated that the hydrogen distribution within the lattice of a material is not dominated by dislocations dragging hydrogen with them.

After this excurse on hydrogen interaction with the material lattice on mesoscale, in the next chapter, the conditions in which the different mechanisms are active is discussed.

3.3.3. Evaluation and discussion of hydrogen embrittlement mechanisms

The investigated pipeline system consists of non-hydride forming materials. Therefore, only the three mechanism HEDE, HELP and AIDE are discussed in the following. Based on the experimental findings, the HELP and AIDE mechanism were favoured. Here, an overview of the applicability of the different mechanism shall be given for different material strength levels leading to the determination of one mechanism applied in the continuum approach within this thesis.

It is commonly agreed upon in literature that not a single mechanism is responsible for the brittle effect of hydrogen on the material properties. Moreover, all three mechanisms act simultaneously while one dominates [15, 65, 66, 67].

One parameter influencing the activity of a mechanism is the strength level of the material. When soft materials are exposed to hydrogen gas, surface blisters can be observed. These blisters result from atomic hydrogen recombined to molecular one in the surface area. The soft host lattice cannot bear this internal pressure and the surface region is

expanded to surface blisters. For this observation, none of the discussed mechanisms is applicable. This observation could be interpreted as a mechanism on its own which only can be observed in soft materials.
Ultra-high strength steels tolerate only very little plastic deformations in general, as stated in chapter 3.2.1. Thus, the HELP mechanism as well as the AIDE mechanism are unlikely to be dominant for hydrogen embrittlement, since both mechanisms assume an increased amount of plastic deformations. Therefore, the reduction of cohesive strength implied by the HEDE mechanism seems to be a likely failure mechanism.
In between the two extremes, more than one mechanism is operative. It can be assumed that due to localized plastic effects (HELP) and the emission of dislocations of the surface (AIDE) the conditions for failure are established while the final rupture is governed by the reduced cohesive strength between the atoms (HEDE).
The existing natural gas pipeline system mainly consists of steels of this intermediate strength range. The AIDE mechanism could be active especially at surfaces in contact with hydrogen. The dislocations emitted from the surface would drag the hydrogen quickly into the bulk material. It could be shown that hydrogen dragged with dislocations inside the material is not a dominant effect in the investigated material. However, the AIDE mechanism involves more complex structures than solely the emission of dislocations which cannot straight forwardly be included in a continuum mechanical approach. Thus, the AIDE mechanism is not considered in this work.
In the following, it is assumed that the enhanced plastic processes (HELP) establishes the conditions for failure, while the final rupture might be dominated by the HEDE mechanism. Since within this study the preexisting conditions of a damaged pipeline segment shall be simulated, the actual failure process is not investigated. Thus, solely the HELP mechanism will be considered within the applied continuum approach. In the next chapter, a stress driven hydrogen transport model is proposed for the calculation of the hydrogen concentration within the material which is coupled with a modified elasto-plastic material model considering the HELP mechanism.

3.4. Mathematical representation of hydrogen embrittlement

Within this thesis, the hydrogen distribution and the according interaction with the material is investigated with a continuum mechanics approach. Therefore, the observed experimental results have to be interpreted in a continuum sense.
In order to simulate hydrogen embrittlement, two coupled models are derived. The hydrogen distribution model is governed by the stress and strain state of the investigated domain while the loading of the material is affect by the accumulated hydrogen. These highly coupled equations are summarized in the following.
Firstly, the mathematical formulation of the hydrogen distribution model is described, followed by a discussion of different possibilities to account for the HELP mechanism in continuum sense.

3.4.1. Governing equations of hydrogen transport

The stress-driven hydrogen distribution model considering trapping is one of the widest used approaches to describe the hydrogen transport within a material lattice [21, 20]. This model is based on the first and second Fick's laws, which were extended by a stress dependent term [74]. The total hydrogen concentration is divided into a hydrogen concentration at lattice sites C_L as well as one concentration bonded to reversible trapping sites C_T as dislocations. Based on Oriani's theorem, the two hydrogen populations of lattice and trapped hydrogen are always in equilibrium [46]. This assumption holds true when the hydrogen concentrations are finite populations and the occupied sites do not interact with each other [15, 46]. Furthermore, the kinetics of filling the reversible traps are assumed to be rather rapid. All systems around a temperature of 300 K meet typically these equilibrium conditions.
The equilibrium relation of lattice and trapping sites can be expressed as [75]

$$\frac{\theta_T}{1-\theta_T} = \frac{\theta_L}{1-\theta_L} exp\left(\frac{W_B}{RT}\right). \tag{3.1}$$

The parameter θ_T represents the occupancy of available trapping sites whereas θ_L represents the one of the interstitial lattice sites. The equilibrium coefficient $exp\left(\frac{W_B}{RT}\right)$ depends on the trap binding energy W_B, the universal gas constant R and the temperature T.
The lattice hydrogen concentration can be expressed by the relation

$$C_L = \theta_L \beta N_L \tag{3.2}$$

with β being the number of normal interstitial lattice sites per host atom. The number of solvent atoms per unit volume $N_L = N_A/V_M$ is defined by Avogadro's number N_A and the molar volume of the host lattice V_M.
Accordingly, the trapped hydrogen concentration

$$C_T = \theta_T \alpha N_T \tag{3.3}$$

is described with α being the number of available sites per trap where hydrogen can be bound.
As the trapping sites, as dislocations, increase in plastically strained regions, the trap density N_T is correlated to the equivalent plastic strain $\bar{\varepsilon}^p$. Kumnick and Johnson [15, 76] associated experimentally the available trapping sites N_T to the equivalent plastic strain $\bar{\varepsilon}^p$

$$\log(N_T(\bar{\varepsilon}^p)) = 23.26 - 2.33\ e^{-5.5\,\bar{\varepsilon}^p} \tag{3.4}$$

for α-iron. Since no experimental results are available to determine the function $N_T(\bar{\varepsilon}^p)$ for the investigated material, the correlation for α-iron is adopted in the following.
The transient stress driven advection diffusion equation including trapping can be defined as follows [21]

$$\frac{D}{D_{eff}}\frac{dC_L}{dt} + \underbrace{\alpha\theta_T\frac{dN_T}{d\bar{\varepsilon}^p}\frac{d\bar{\varepsilon}^p}{dt}}_{trap\ generation} - \underbrace{D\,\nabla^2 C_L}_{diffusion} + \underbrace{\nabla\left(\frac{DV_H}{RT}C_L\,\nabla p\right)}_{advection} = 0 \tag{3.5}$$

with the time derivative $\frac{(\cdot)}{\partial t}$ and the partial molar volume of hydrogen V_H. The transient differential equation of the interstitial lattice concentration C_L can generally be subdivided into a trap generation, a diffusion as well as in an advective part.

The trap generation term is non-zero when new traps are generated by plastic straining. Therefore, the filling of the newly generated traps is considered by reducing the lattice hydrogen concentration C_L and in turn an increasing trapped hydrogen concentration C_T governed by the function of the trapping sites $N_T(\bar{\varepsilon}^p)$. This term captures the strain rate dependent effect of hydrogen embrittlement since at high strain rates the accumulated equivalent plastic strain over time $\frac{\partial \bar{\varepsilon}^p}{\partial t}$ results in high values. Thus, the reduction of the lattice hydrogen concentration gets more pronounced until all traps are filled and reduces the amount of hydrogen which enters further inside the material.

The diffusion term is characterized by the lattice diffusion coefficient D.

The stress driven diffusion part acts like an advective term in this differential equation. When investigating the units of this term, it results in the unit of a velocity multiplied by the lattice hydrogen concentration C_L. Thus, this stress dependent term can be interpreted as the advective part and the derivative of the hydrostatic stress ∇p defines the velocity direction. In other words, the host lattice is stretched due to the hydrostatic stress and therefore the spacing between the molecules is increased. Thus, the hydrogen atoms can move more easily in regions with higher hydrostatic stresses.

In case the traps in the lattice are not filled with hydrogen, a reduction of the lattice hydrogen concentration needs to be considered until the traps are filled. This reduces the diffusion of hydrogen through the lattice and can be expressed by the term $\frac{D}{D_{eff}}$, defined as [21]

$$\frac{D}{D_{eff}} = \left(1 + \frac{\partial C_T}{\partial C_L}\right) = \left(1 + \frac{K_T\,\alpha\,\beta\,N_L N_T}{\left[\beta N_L + (K_T - 1)C_L\right]^2}\right). \tag{3.6}$$

In case the trapping sites are not totally filled with hydrogen, this ratio of the diffusion parameter D and the effective diffusion parameter D_{eff} is smaller than one scaling the lattice hydrogen concentration C_L to account for the rapid filled traps. In case all traps are filled with hydrogen, this scaling factor is equal to one and does not alter the lattice hydrogen concentration.

The trapped hydrogen concentration C_T can be derived from equation (3.1) to (3.3) as

$$C_T = \frac{K_T\,\alpha\,N_T(\bar{\varepsilon}_p)\,C_L}{\beta N_L + (K_T - 1)C_L}. \tag{3.7}$$

The trapped hydrogen concentration C_T is governed by the available trapping $N_T(\bar{\varepsilon}^p)$ as well as the available hydrogen concentration in the lattice C_L.

Up to this point, the transient differential equation accounting for hydrogen transport and trapping effects has been presented. The derived equations are tied to the mechanical stress and strain field, namely the hydrostatic stress p and the equivalent plastic strain $\bar{\varepsilon}^p$. In the following, the effect of accumulated hydrogen on the material properties shall be discussed.

3.4.2. Adjustment of elasto-plastic material model to account for hydrogen

The experimental results in chapter 3.2 have shown that hydrogen embrittles the material and the HELP mechanism was identified to be active in case of the investigated pipeline material. In the following, possibilities to include the brittle effect of hydrogen in an elasto-plastic continuum framework presented in chapter 2.1 is investigated.

In general, two fundamental ideas to account for hydrogen embrittlement in continuum mechanics are discussed in literature. Firstly, hydrogen is assumed to introduce additional straining within the material [21]. Secondly, a reduction of the yield stress in the presence of hydrogen is assumed [25]. Also combinations of both attempts are studied [20]. These ideas shall be examined in the following in the context of reflecting the hydrogen embrittlement mechanism.

The first attempt is to extend the classical continuum mechanics by an additional strain introduced by accumulated hydrogen $\boldsymbol{\varepsilon}_H$ [21]. Then, the strain tensor is decomposed into three parts $\boldsymbol{\varepsilon} = \boldsymbol{\varepsilon}_e + \boldsymbol{\varepsilon}_p + \boldsymbol{\varepsilon}_H$. A further assumption for this additional strain $\boldsymbol{\varepsilon}_H$ implies that hydrogen induces only dilatational straining [18]. Thus, $\boldsymbol{\varepsilon}_H$ does not affect the plastic behaviour of the material since the plastic strain is assumed to be independent from volumetric straining.

This additional strain due to hydrogen can be understood as a continuum interpretation of a reduction of the cohesive strength since an additional local dilatational stress is introduced by the hydrogen. Therefore, this idea of hydrogen induced straining can be interpreted as equivalent to the HEDE mechanism. In chapter 3.3.3 it has been concluded that the HELP mechanism establishes the conditions for failure. Thus, no hydrogen induced purely dilatational straining is considered within the numerical realization in this work.

Another idea of defining the hydrogen dependent strain $\boldsymbol{\varepsilon}_H$ is to assume that hydrogen induces a dilatational straining as well as a deviatoric one [20]. The deviatoric part of the hydrogen dependent strain $\boldsymbol{\varepsilon}_H$ enhances the plastic deformation at places of accumulated hydrogen. This additional plastic strain can be treated as a local enhanced plasticity effect due to hydrogen and thus as the HELP mechanism. However, this way of modelling the HELP mechanism only indirectly induces a local softening via the deviatoric part of the hydrogen dependent strain $\boldsymbol{\varepsilon}_H$. The dilatational part reflects mostly the HEDE mechanism as discussed above. Therefore, within this work a more direct influence on the plastic behaviour is favoured which is discussed in the following in more detail.

The second approach includes a direct effect of hydrogen on the yield stress which induces direct local softening in a continuum sense like proposed in the HELP mechanism.

Therefore, a reduction of the yield stress is defined in dependency of hydrogen [13, 25]. The strain $\boldsymbol{\varepsilon}$ is decomposed like in classical continuum mechanics in an elastic $\boldsymbol{\varepsilon}_e$ and a plastic $\boldsymbol{\varepsilon}_p$ component. In this case no additional strain according to hydrogen is considered. The von Mises yield criterion, expressed in equation (2.16), can be defined in dependency on the hydrogen concentration with the parameter c

$$f = \|\widetilde{\boldsymbol{\sigma}} - \boldsymbol{\beta}\| - \sigma_y(\sigma_{y0}, \alpha, c). \tag{3.8}$$

Therefore, the function $\sigma_y(\sigma_{y0}, \alpha)$ given in equation (2.17) can be redefined in dependency on a hydrogen dependent yield stress $\sigma_{y0}(c)$ as follows

$$\sigma_y(\sigma_{y0}, \alpha, c) = \sqrt{\frac{2}{3}}(\sigma_{y0}(c) + \alpha). \tag{3.9}$$

In literature, several approaches to define the hydrogen dependent yield stress $\sigma_{y0}(c)$ are derived. In the following, three different approaches are presented.
Motivated by an experimentally observed linear correlation of the hydrogen pressure and the flow stress in iron by Tabata and Birnbaum [77], Sofronis et al. [78] suggested a linear decrease of the original material yield stress σ_{y0} with an increasing hydrogen concentration

$$\sigma_{y0}(c) = [(\xi - 1)c + 1]\,\sigma_{y0}. \tag{3.10}$$

The parameter c depends on the lattice hydrogen concentration C_L as well as on the trapped hydrogen concentration C_T

$$c = (C_L + C_T)/N_L. \tag{3.11}$$

The total hydrogen concentration of the trapped and lattice hydrogen concentration $C_L + C_T$ is normalized by N_L, a parameter reflecting the total available sites of solvent atoms per unit volume in lattice sides. In other words, the factor c reflects the occupancy of available lattice sides.
The parameter ξ is a material dependent softening parameter. If ξ is considered to be one, the material is not affected by hydrogen. In case the parameter ξ is chosen to be zero, the material is maximally susceptible to hydrogen and thus a maximal reduction of the yield stress is applied, leading to an enhanced softening effect. With the help of this parameter, effects like the hydrogen dependency on the material strength level can be considered in the numerical model.
A modification of this approach was proposed by Kotake et al. [13] in the form of

$$\sigma_{y0}(c) = (\zeta\, c + 1)\,\sigma_{y0}. \tag{3.12}$$

In this case, the parameter ζ can emulate hydrogen induced softening with $\zeta < 0$ as well as hardening with $\zeta > 0$. By choosing $\zeta = 0$, no effect of hydrogen on the yield stress is considered. Hydrogen induced hardening contradicts the experimental findings of the hydrogen effect on the investigated pipeline materials summarized in chapter 3.2. Nevertheless, hardening in the presence of hydrogen could be observed for other materials under certain circumstances [13, 79].
It should be noted that the parameter ζ may very well be interpreted as an entirely material dependent measure for the amount of hydrogen embrittlement, in contrast to ξ being a scaling factor limited to a maximum value of one (compare equation (3.10)).
A further approach assuming the yield stress being solely dependent on the trapped hydrogen, is suggested by Dadfarnia et al. [26]

$$\sigma_{y0}(c) = [(\xi - 1)c_{T,r} + 1]\;\sigma_{y0} \tag{3.13}$$

with the factor $c_{T,r} = C_T/C_r$ and the reference concentration C_r. According to Dadfarnia et al. [26], this reference concentration C_r is chosen to be equal to the surface hydrogen concentration $C_{L,0}$ which is applied as a boundary condition on the pipeline surface. This surface hydrogen concentration is determined in dependency on the hydrogen pressure within the tube. For further information on the determination of $C_{L,0}$ it is referred to chapter 5.2.2.
To give a better overview of the meaning of the different material parameters, Table 3.1 summarizes the suggested softening parameters for the three presented approaches.

Table 3.1.: Comparison of softening approaches

Equation	**No softening**	**Max. softening**	**Relation to hydrogen concentration**
equation (3.10)	$\xi = 1$	$\xi = 0$	$c = (C_L + C_T)/N_L$
equation (3.12)	$\zeta = 0$	$\zeta < 0$ (no defined max. limit)	$c = (C_L + C_T)/N_L$
equation (3.13)	$\xi = 1$	$\xi = 0$	$c_{T,r} = C_T/C_r = C_T/C_{L,0}$

When comparing equation (3.13) to equation (3.10), the factor c is replaced by the parameter $c_{T,r}$. One obvious difference of these two factors is that the parameter c includes a softening effect due to the lattice as well as the trapped hydrogen concentration while the factor $c_{T,r}$ refers only a softening effect to the trapped hydrogen population C_T. A further distinction of these two parameters is the reference value of the respective hydrogen concentrations. As discussed above, the factor c relates the total hydrogen concentration to the available trapping sites N_L and can therefore be interpreted as the amount of lattice sides occupied with hydrogen. In contrast to that, the parameter $c_{T,r}$ is relating the trapped hydrogen concentration to a reference hydrogen concentration. The choice of the softening model and the reference values obviously has a direct impact on the amount of hydrogen embrittlement which will be discussed in chapter 6.2.

The general aim of all softening models presented above is to describe the effect of hydrogen embrittlement in a continuum mechanics framework suitable for large engineering structures such as members of the existing natural gas pipeline system. The challenge of the continuum model is to solve the highly coupled equations of the mechanical and the hydrogen distribution model. In the following chapter, the realization of the numerical framework is discussed.

4. Numerical Methods

In this chapter, the numerical procedure and the methods used to simulate hydrogen embrittlement are discussed. First a iterative procedure for the coupled mechanical and hydrogen transport model is presented. Then, the numerical models used for discretisation are described.
As a basis of this program serves the institute's inhouse Matlab based finite element code.

4.1. Structure of the model

Figure 4.1 gives a schematic representation of the numerical procedure for coupling the mechanical model with the transient hydrogen transport model. The mechanical elasto-plastic finite element model includes no time dependent effects. The stress state depends only on the applied loading. However, the hydrogen distribution is transient and thus every load step is artificially tied to a time step.

```
for each load step/ time step
    while hydrogen + mechanical model not converged do
    end
end
```

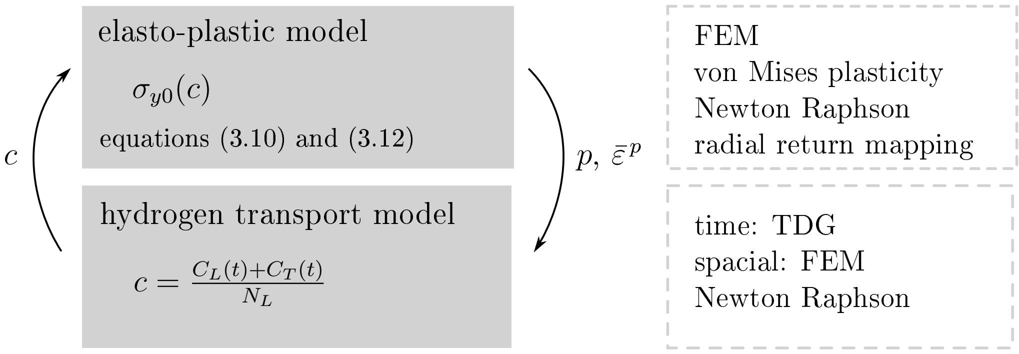

Figure 4.1.: Schematic representation of the coupling procedure of the elasto-plastic model with the hydrogen distribution model

In a first step, the mechanical equilibrium condition is solved with the initial hydrogen concentration. When the mechanical model converges, the hydrostatic stress p and the equivalent plastic strain $\bar{\varepsilon}^p$ are forwarded to the transient hydrogen distribution model. In a second step, the hydrogen concentration distribution is determined with the constant input variables of the mechanical model. The hydrogen parameter c is then passed back to the elasto-plastic model, influencing directly the yield stress $\sigma_{y0}(c)$. Then the mechanical equilibrium condition is solved again.

This procedure is repeated until the mechanical and hydrogen properties are in equilibrium. Then the next load step is applied.

The elasto-plastic model as well as the hydrogen transport model are discretised by the finite element method (FEM) in space. For the time discretisation of the transient hydrogen distribution, also a finite element approach is used in form of the Time Discontinuous Galerkin (TDG) method. These discretisation methods are described in more detail in the following.

4.2. Hydrogen transport model

The differential equation of the hydrogen transport model needs to be discretised in time as well as in space. Therefore, a finite element approach in space and time is used, which is described in the following.

4.2.1. Time discretisation: Discontinuous Galerkin method

The general idea of the Time Discontinuous Galerkin (TDG) method is to discretise the time domain using finite elements and allow discontinuities at the borders of these time elements. This approach is based on the discontinuous Galerkin method which was origionally formulated for hyperbolic equations [80]. The advantages of the TDG method are that it is unconditionally stable and the time integration scheme is accurate even with high Courant numbers [81]. Therefore, the TDG is not tied to small time steps. This method was introduced by Reed & Hill [82] and Lesaint & Reviart [83]. A detailed description of the TDG method can be found in [84, 80] and other parts of literature.

Figure 4.2 depicts a schematic representation of the TGD for linear elements. The time domain τ_n is separated into time steps $[t^{n-1}, t^n]$, similar to finite difference schemes. At the borders of time elements, discontinuities are explicitly allowed, which implies two different results of the primal variable at every time step.

The strategy of this numerical scheme is explained at the example of the transient hydrogen transport model in the following analogue to [84, 80, 85].

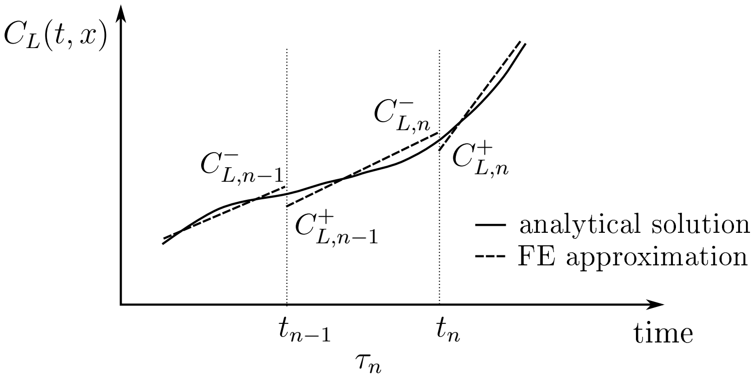

Figure 4.2.: Scheme of TDG for linear elements (adapted from [84])

In a first step, the weak form of the transient hydrogen distribution model, given in equation (3.5), is postulated. For this, the differential equation (3.5) is integrated over the space domain Ω as well as the time domain τ_n and it is multiplied by a test function η

$$\int_{\Omega}\int_{\tau_n} \eta \left[\frac{D}{D_{eff}} \frac{\partial C_L}{\partial t} + \underbrace{\alpha\theta_T \frac{dN_T}{d\bar{\varepsilon}^p}\frac{d\bar{\varepsilon}^p}{dt} - \nabla\left(D\nabla C_L\right) + \nabla\left(\frac{DV_H}{3RT} C_L \nabla p\right)}_{Z} \right] dt\, dV = 0. \quad (4.1)$$

The test function depends on space and time $\eta = \eta(x,t)$. In this chapter, the focus lies on the time discretisation scheme. The spatial representation is only mentioned for the sake of completeness and is discussed in the framework of the next chapter. Thus, for reasons of clarity, the entire spatial part of the transient hydrogen distribution equation is summarized and substituted by the function Z.

$$\int_{\Omega}\int_{\tau_n} \left(\eta \frac{D}{D_{eff}} \frac{\partial C_L}{\partial t} + \eta\, Z \right) dt\, dV = 0 \quad (4.2)$$

Here, also the trapping term $\alpha\theta_T \frac{dN_T}{d\bar{\varepsilon}^p}\frac{d\bar{\varepsilon}^p}{dt}$ is treated as a spatial discretisation term because the evolution of the plastic strain rate computed with the mechanical model does solely depend on the applied loading conditions and does not include time dependent material effects. Thus, the time derivative of the equivalent plastic strain $\frac{d\bar{\varepsilon}^p}{dt}$ can be interpreted as the plastic strain accumulated during one loading step which is artificially tied to a time step by the hydrogen distribution model. Then, this artificial time dependency does not need to be included in the time integration scheme.

The ratio $\frac{D}{D_{eff}}$ is a function of the lattice hydrogen concentration C_L (compare equation (3.6)). Practically speaking, this factor scales the lattice hydrogen concentration from zero to one, accounting for trapping effects. Here, the same argument holds true as for the trap generation term: In this work the focus is placed on the steady state results and thus this ratio is set to one.

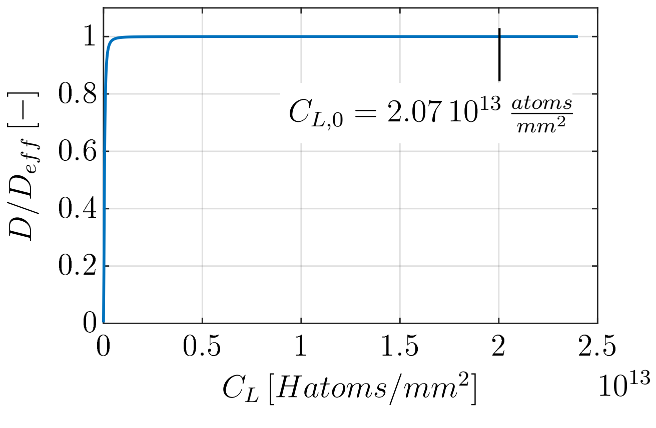

Figure 4.3: The effective diffusion ratio $\frac{D}{D_{eff}}$ as a function of the lattice hydrogen concentration C_L. The Dirichlet boundary condition $C_{L,0}$ is chosen for a hydrogen pressure of $10\,MPa$ according to Sieverts' law (compare chapter 5.2.2).

Besides modelling aspects, there is another reason from an engineering point of view to set the ratio $\frac{D}{D_{eff}}$ to one. In Figure 4.3, the ratio $\frac{D}{D_{eff}}$ is plotted according to equation (3.6) over the lattice hydrogen concentration C_L and the applied boundary condition for a pressurised tube is marked within the graph. When investigating near surface characteristics, like in this work, this factor is always one. Thus, an additional linearisation of this factor and the additional numerical costs are judged as not reasonable.

Coming back to the TDG derivation, as stated above, jumps of the primal variable $[|C_{L,n}|]$ are allowed at the time element borders. Thus, for every time step t_n two values of $C_L(x,\, t_n)$ exist for linear time elements (compare Figure 4.2). These values can be expressed by

$$C^+_{L,n} = \lim_{e \to 0} C_L(t_n + e), \quad C^-_{L,n} = \lim_{e \to 0} C_L(t_n - e), \quad [|C_{L,n}|] = C^+_{L,n} - C^-_{L,n} \tag{4.3}$$

with the scalar $e > 0$. These two values of C_L for one time step t_n are marked with a $-$ in case the value corresponds to the former finite time element (left) and $+$ when referring to the next finite time element (compare Figure 4.2).

The partial integration of the time integral of equation (4.2) leads to

$$\int_\Omega \int_{\tau_n} \left(-\frac{\partial \eta}{\partial t} C_L + \eta\, Z \right) dt\, dV + \eta(t_n)\, C_L(t_n) - \eta(t_{n-1})\, C_L(t_{n-1}) = 0. \tag{4.4}$$

Due to the admitted discontinuities at the element borders these elements are not coupled. Therefore, a numerical flux of the form

$$\eta(t_n)\, C_L(t_n) - \eta(t_{n-1})\, C_L(t_{n-1}) = \eta^+_n\, C^+_{L,n} - \eta^+_{n-1}\, (\alpha C^-_{L,n-1} + (1-\alpha) C^+_{L,n-1}) \tag{4.5}$$

is applied at the nodes of this time interval. The parameter $\alpha \in [0, 1]$ controls the numerical flux. Since for the time approximation it is straight forward to assume that information are passed from the past to the future, an explicit scheme by choosing $\alpha = 1$ is adopted. This passing of information from the previous finite time element by $C^-_{L,n-1}$ serves as a kind of initial condition for the actual investigated one (compare Figure 4.2).

A second partial integration of equation (4.4) in time leads to

$$\int_\Omega \int_{\tau_n} \left(\eta \frac{\partial C_L}{\partial t} + \eta\, Z \right) dt\, dV + \eta^+_{n-1}\, [|C_{L,n-1}|] = 0 \tag{4.6}$$

at the time interval border t_{n-1}.

With the help of the shape function in time $\widetilde{N} = \widetilde{N}(t)$, the primal variable $C_L = C_L(x,t)$ and the test function $\eta = \eta(t,x)$ can be written as

$$\begin{aligned} C_L(x,t) &\approx \sum_{\theta=1}^{m_t} \widetilde{N}_\theta\, \widetilde{C}_{L\,\theta}, \qquad \eta(t,x) \approx \sum_{\theta=1}^{m_t} \widetilde{N}_\theta\, \widetilde{\eta}_\theta, \\ \frac{\partial \eta}{\partial t} &\approx \sum_{\theta=1}^{m_t} \frac{\partial \widetilde{N}_\theta}{\partial t} \widetilde{\eta}_\theta = \sum_{\theta=1}^{m_t} \widetilde{N}_{,t\,\theta}\, \widetilde{\eta}_\theta, \end{aligned} \tag{4.7}$$

with the number of nodes in time m_t. The variables marked with $\widetilde{(\cdot)}$ are discretised in time, but not yet in space. Using the discretisation above, the weak formulation of equation (4.6) leads to

$$\begin{aligned}\underbrace{\left[\int\limits_{\tau_n} \widetilde{\boldsymbol{N}}^T \widetilde{\boldsymbol{N}}_{,t}\,dt + \widetilde{\boldsymbol{N}}^{+T}_{t_{n-1}} \widetilde{\boldsymbol{N}}^{+}_{t_{n-1}}\right]}_{\boldsymbol{T_a}} \otimes \int\limits_{\Omega_e} \tilde{\eta}\,\widetilde{\boldsymbol{C}}_L\,d\Omega_e + \underbrace{\left[\int\limits_{\tau_n}\widetilde{\boldsymbol{N}}^T\widetilde{\boldsymbol{N}}dt\right]}_{\boldsymbol{T_b}} \otimes \int\limits_{\Omega_e}\tilde{\eta}\,\widetilde{\boldsymbol{Z}}\,d\Omega_e \\ = \underbrace{\left[\int\limits_{\tau_n}\widetilde{\boldsymbol{N}}^{+T}_{t_{n-1}}\widetilde{\boldsymbol{N}}^{-}_{t_{n-1}}dt\right]}_{\boldsymbol{T_c}}\otimes\int\limits_{\Omega_e}\tilde{\eta}\,\widetilde{\boldsymbol{C}}_L\,d\Omega_e.\end{aligned} \tag{4.8}$$

It is assumed that time and space can be separated multiplicatively. The time matrices $\boldsymbol{T_a}$, $\boldsymbol{T_b}$ and $\boldsymbol{T_c}$ are constant as long as the time step is constant.
The function $\widetilde{\boldsymbol{Z}}$ represents the spatial part of the advective diffusion equation in which the primal variable $\widetilde{\boldsymbol{C}}_L$ is discretised in time, but not yet in space. This time discretisation approach can be combined with any spatial finite element approach.
The polynomial order of the shape function in time can be chosen arbitrarily. Nevertheless, it has to be kept in mind that with increasing degree of the polynomial order, additional degrees of freedom (DOF) are added. When using a TDG of the polynomial order of 0 for a system of equations with $n \times n$ DOFs, no degrees of freedom are added. With linear shape functions in time two additional DOFs are added to the spatial degrees of freedom n and the system of equations has the dimension of $2n \times 2n$ DOFs.
Obviously, this leads to a significant increase in numerical costs, especially when simulating larger models. In this thesis, the TDG is applied, since it showed to be well suitable to avoid stabilization problems, especially for larger time steps. Still, the engineer or researcher has to repeatedly outweigh the increased numerical effort due to a higher number of DOFs when using the TDG against a possibly higher number of necessary equilibrium iterations when using other time discretisation methods.

4.2.2. Spatial discretisation: Finite element method

For the spatial discretisation of the stress driven diffusion equation, a standard finite element method (FEM) is used. A brief overview of its coupling to the TDG method is given in the following.
In a first step, the term from equation (4.8) which was previously summarized to $\widetilde{\boldsymbol{Z}}$ is discussed

$$\begin{aligned}\int\limits_{\Omega_e} \tilde{\eta}\,\widetilde{\boldsymbol{Z}}\,d\Omega_e = \frac{D_{eff}}{D}\Bigg(\int_{\Omega} \tilde{\eta}\,\alpha\theta_T \frac{dN_T}{d\bar{\varepsilon}^p}\frac{d\bar{\varepsilon}^p}{dt}\,\mathrm{d}\Omega \\ - \int_{\Omega}\tilde{\eta}\,\nabla\Big(D\,\nabla\widetilde{\boldsymbol{C}}_L\Big)\,\mathrm{d}\Omega + \int_{\Omega}\tilde{\eta}\,\nabla\left(\frac{DV_H}{3RT}\,\widetilde{\boldsymbol{C}}_L\,\nabla p\right)\mathrm{d}\Omega\Bigg)\,.\end{aligned} \tag{4.9}$$

Before the discretisation of the weak formulation itself is reviewed in more detail, again the trap generation term shall be addressed (compare the discussion in the chapter 3.4.1). Since steady state conditions are evaluated in this work, the trap generation term $\alpha\theta_T \frac{dN_T}{d\bar{\varepsilon}^p}\frac{d\bar{\varepsilon}^p}{dt}$ can be discarded as this term will not alter the steady state results.

When discarding this terms from equation (4.9), the weak formulation can be rewritten by using the product rule and the divergence theorem to

$$
\begin{aligned}
\int\limits_{\Omega_e} \tilde{\eta}\, \tilde{\boldsymbol{Z}}\, d\Omega_e = -\int_{\Omega} \nabla\tilde{\eta} \left(D \nabla \tilde{\boldsymbol{C}}_L \right) \mathrm{d}\Omega + \int_{\Omega} \tilde{\eta}\, \frac{DV_H}{3RT} \nabla \tilde{\boldsymbol{C}}_L\ \nabla p \,\mathrm{d}\Omega \\
+ \int\limits_{\Gamma} \eta\, \frac{DV_H}{3RT}\, C_L \nabla p\, n \,\mathrm{d}\Gamma - \int\limits_{\Gamma} \eta\, D\, \nabla C_L\, n \,\mathrm{d}\Gamma.
\end{aligned}
\tag{4.10}
$$

The gradient of the hydrostatic stress ∇p is assumed to be constant within one time step. This gradient is treated as an input variable from the mechanical model and thus is assumed to be independent from the primal variable $\tilde{\boldsymbol{C}}_L$. With the help of the two surface therms, flow boundary conditions can be defined. In this thesis, no flow boundary conditions are applied. Thus, the two surface terms combined are equal to zero ($\int\limits_{\Gamma} \eta\, \frac{DV_H}{3RT}\, C_L \nabla p\, n \,\mathrm{d}\Gamma - \int\limits_{\Gamma} \eta\, D\, \nabla C_L\, n \,\mathrm{d}\Gamma = 0$).

The primal variable $\tilde{\boldsymbol{C}}_L$ and the test function $\tilde{\eta}$ as well as its derivative are approximated using the approach

$$
\begin{aligned}
&\tilde{C}_L \approx \sum_{I=1}^{m_s} N_I\, \hat{\tilde{C}}_{L\,I}, &&\tilde{\eta} \approx \sum_{I=1}^{m_s} N_I\, \hat{\tilde{\eta}}_I, && \\
&\nabla\tilde{C}_L \approx \sum_{I=1}^{m_s} \nabla N_I\, \hat{\tilde{C}}_{L\,I}, &&\nabla\tilde{\eta} \approx \sum_{I=1}^{m_s} \nabla N_I\, \hat{\tilde{\eta}}_I, &&\nabla p \approx \sum_{I=1}^{m_s} \nabla N_I\, \hat{p}_I,
\end{aligned}
\tag{4.11}
$$

with the spatial shape function N_I and the number of spatial nodes m_s. Parameters marked with $\hat{\tilde{*}}$ are discretised in time and in space. The gradient of the hydrostatic stress ∇p is a mechanical property which is only artificially tied to a time step as the trap generation term. Thus, this term is only discretised in space marked with $\hat{*}$.

The gradient of the hydrostatic stress is approximated with the same shape function as the primal variable. It has to be noted that for the spatial discretisation of the mechanical model a C_0-continuous ansatz is used. Thus, the calculated hydrostatic stress p at the Gauss points is constant in one element. In order to get a continuous field of the hydrostatic stresses, the Gauss point solution is projected on the nodes before every hydrogen time step. These smoothed results are used to calculate the gradient of the hydrostatic stress.

With the described discretisation in space above, the coupled finite element approach in time and space, defined in equation (4.8), results in

$$
\begin{aligned}
&\boldsymbol{T_a} \otimes \underbrace{\int\limits_{\Omega_e} \boldsymbol{N}^T \boldsymbol{N}\, d\Omega_e}_{\boldsymbol{M}}\, \hat{\tilde{\boldsymbol{C}}}_L \\
&+ \boldsymbol{T_b} \otimes \underbrace{\int\limits_{\Omega_e} \nabla \boldsymbol{N}^T D\, \nabla \boldsymbol{N}_L \,\mathrm{d}\Omega_e - \int\limits_{\Omega_e} \frac{DV_H}{3RT} \boldsymbol{N}^T \nabla \boldsymbol{N} \hat{\tilde{\boldsymbol{C}}}_L\ \nabla \boldsymbol{N} \hat{\boldsymbol{p}} \,\mathrm{d}\Omega_e}_{\boldsymbol{K}}\, \hat{\tilde{\boldsymbol{C}}}_L \\
&= \boldsymbol{T_c} \otimes \underbrace{\int\limits_{\Omega_e} \boldsymbol{N}^T \boldsymbol{N}\, d\Omega_e}_{\boldsymbol{M}}\, \hat{\tilde{\boldsymbol{C}}}_{L,n-1}\,.
\end{aligned}
\tag{4.12}
$$

To solve this system of equations, a Newton-Raphson scheme is applied. Therefore, the primal variable $\hat{\tilde{\boldsymbol{C}}}_L$ is linearised

$$\hat{\tilde{\boldsymbol{C}}}_L^{k} = \hat{\tilde{\boldsymbol{C}}}_L^{k-1} + \Delta\hat{\tilde{\boldsymbol{C}}}_L^{k-1} \tag{4.13}$$

and equation (4.12) can be reformulated to

$$\left(\boldsymbol{T_a} \times \boldsymbol{M} + \boldsymbol{T_b} \times \boldsymbol{K}\right) \Delta\hat{\tilde{\boldsymbol{C}}}_L^{k-1} = -\left(\boldsymbol{T_a} \times \boldsymbol{M} + \boldsymbol{T_b} \times \boldsymbol{K}\right) \hat{\tilde{\boldsymbol{C}}}_L^{k-1} + \boldsymbol{T_c} \times \boldsymbol{M}\, \hat{\tilde{\boldsymbol{C}}}_{L,n-1}. \tag{4.14}$$

Here, the index $n-1$ refers to the last time step and $k-1$ refers to the last iteration step of the Newton-Raphson iteration scheme.

It should be noted that the shape function in time and space may be chosen independently.

4.3. Elasto-plastic finite element model

The elasto-plastic model describes the material response according to the loading conditions as well as the hydrogen concentration (compare chapter 2.1.3 and chapter 3.4.2). Here, a finite element method (FEM) is applied just like for the spatial distribution of the hydrogen concentration.

In order to formulate the material response with the FEM, the evolution equations summarized in equation (2.18) need to be numerically integrated. For detailed information it is referred to [86, 27, 87]. In the following a short overview is given.

An implicit Euler scheme is used to integrate the plastic strain rate as well as the internal hardening parameters. Geometrically speaking, an unacceptable high stress is orthogonally projected back on the yield surface in the principle stress space, which is often referred to as radial return mapping. An overview of the numerically integrated formulation of an ideal plastic material model is given in box 4.1, since no linear hardening is applied in this work (compare chapter 5).

In a first step, a purely elastic deviatoric test stress ${}^{n+1}\tilde{\boldsymbol{\sigma}}^{test}$ is defined with the plastic strain ${}^{n+1}\tilde{\boldsymbol{\varepsilon}}_p{}^{test}$ chosen to be the plastic strain of the previous iterated load step n. With this test stress, the flow rule f is evaluated.

In case f is smaller than or equal to zero, it is a valid elastic stress state. The total stress ${}^{n+1}\boldsymbol{\sigma}$ can be directly calculated with the deviatoric test stress ${}^{n+1}\tilde{\boldsymbol{\sigma}}^{test}$ and an additional hydrostatic component. The plastic strain is not altered and the material tangent $\mathbb{C}^e$ can be calculated.

In case the flow rule f is larger than zero, the test stress ${}^{n+1}\tilde{\boldsymbol{\sigma}}^{test}$ is invalid high. The material cannot bear such high stress states. Thus, the test stress is projected back on the yield surface by simultaneously accumulating plastic strain. This additional accumulated plastic strain is accounted for by reducing the stress state by the term $2\mu\,\Delta\lambda\,{}^{n+1}\boldsymbol{n}$. The elasto-plastic material tangent $\mathbb{C}^{ep}$ can be determined accordingly.

A Newton-Rapson scheme is applied to iteratively solve every load step of the plastic straining of the material.

calculate test stress and set plastic strain from last iterated step as plastic test strain

$$^{n+1}\widetilde{\boldsymbol{\sigma}}^{test} = 2\mu \left(^{n+1}\widetilde{\boldsymbol{\varepsilon}} -^{n} \widetilde{\boldsymbol{\varepsilon}}_p\right)$$

$$^{n+1}\widetilde{\boldsymbol{\varepsilon}}_p^{\;test} =^{n} \widetilde{\boldsymbol{\varepsilon}}_p$$

evaluate flow rule

$$^{n+1}f^{test} = ||^{n+1}\widetilde{\boldsymbol{\sigma}}^{test}|| - \sqrt{\frac{2}{3}}\,\sigma_{y0}(c)$$

$if\;\; f \leq 0$ - pure elastic step

$$^{n+1}\boldsymbol{\sigma} = 3\kappa\, tr(\boldsymbol{\varepsilon})\boldsymbol{I} + {}^{n+1}\widetilde{\boldsymbol{\sigma}}^{test}$$

$$^{n+1}\widetilde{\boldsymbol{\varepsilon}}_p = {}^{n+1}\widetilde{\boldsymbol{\varepsilon}}_p^{\;test}\,, \quad \Delta\lambda = 0$$

$$\mathbb{C}^e = \kappa\,\boldsymbol{I}\otimes\boldsymbol{I} + 2\mu\left(\mathbf{1} - \frac{1}{3}\boldsymbol{I}\otimes\boldsymbol{I}\right)$$

$else$ - plastic corrector step

$$^{n+1}\boldsymbol{\sigma} = 3\kappa\, tr(\boldsymbol{\varepsilon})\boldsymbol{I} + {}^{n+1}\widetilde{\boldsymbol{\sigma}}^{test} - 2\mu\,\Delta\lambda\,{}^{n+1}\boldsymbol{n}$$

$$^{n+1}\widetilde{\boldsymbol{\varepsilon}}_p = {}^{n+1}\widetilde{\boldsymbol{\varepsilon}}_p^{\;test} + \Delta\lambda\,{}^{n+1}\boldsymbol{n}$$

$$^{n+1}\boldsymbol{n} = \frac{^{n+1}\widetilde{\boldsymbol{\sigma}}^{test}}{||^{n+1}\widetilde{\boldsymbol{\sigma}}^{test}||}\,, \quad \Delta\lambda = \frac{^{n+1}f^{test}}{2\mu}$$

$$\mathbb{C}^{ep} = \kappa\,\boldsymbol{I}\otimes\boldsymbol{I} + 2\mu\left(1 - \Delta\lambda\frac{2\mu}{||^{n+1}\widetilde{\boldsymbol{\sigma}}^{test}||}\right)\left(\mathbf{1} - \frac{1}{3}\boldsymbol{I}\otimes\boldsymbol{I} - {}^{n+1}\boldsymbol{n}^{test}\otimes{}^{n+1}\boldsymbol{n}^{test}\right)$$

Box 4.1: Ideal plasticity for small deformation (compare [86, 27, 87])

5. Numerical Models

In this chapter, the modelling of a representative natural gas pipeline is described. The aim of this thesis is to evaluate the influence of hydrogen gas pumped through the existing natural gas pipeline system on the material properties. Therefore, in a first step representative pipeline dimensions and pressures are identified. In a further step, the modelling of a representative pipeline using a full size model as well as a surrogate model is examined.

5.1. Choice of representative modelling parameters

As stated above, the effect of hydrogen on natural gas pipelines is investigated in this thesis. In consequence, it is mandatory to choose the modelling parameters, as dimensions, material and loading, to be representative for the natural gas pipeline system.

To identify the pipeline dimension and the material, a project list of Salzgitter, one of Germany's main steel tube and pipe supplier companies, is used [41]. This list summarizes the construction projects of natural gas since 2000. The pipeline dimensions varied from diameters of $914\,mm$ to $1,016\,mm$ with wall thicknesses from $9\,mm$ to $22.9\,mm$. In this thesis, a tube with a diameter of $1,016\,mm$ and a wall thickness of $17.5\,mm$ is investigated. Here, the projects with the same dimensions were grouped together and the dimensions used to build the longest distance in the natural gas pipeline system were chosen. The most commonly applied material could be identified as pipeline steel API X70.

A common pressure within the natural gas pipeline system is reported to be up to $100\,bar = 10\,MPa$ for onshore pipelines [40]. Thus, this pressure level is adopted for the following simulations.

While representative dimensions and the choice of material could be based on general spreadsheets from industry practice, the actual material data, such as the Young's modulus and the yield strength, still need to be defined. Fortunately, Baek et al. [88] conducted tensile tests with specimens machined from an actual pipeline tube of API X70 which were exposed to a hydrogen gas pressure of $10\,MPa$ while straining. This implies that the tested material underwent the same forming process as the actual tubes within the natural gas pipeline system. Still, it is possible that by extracting the tensile specimens from the tube, the material properties could have been slightly altered. Nevertheless, as the material data extracted from this testing campaign show to be the most representative ones available, they are applied in the framework of this thesis.

Mechanical parameters which were not directly given in the publication of Baek et al. were extracted from the stress-strain curve reproduced in Figure 5.1. In the framework of the introduced linear hardening theory, the non-linear hardening behaviour of the stress-strain curve cannot be directly captured. Since a linear hardening would overestimate the stress state in the vicinity of the crack tip, a conservative ideally plastic approach is considered for the evaluation of hydrogen embrittlement.

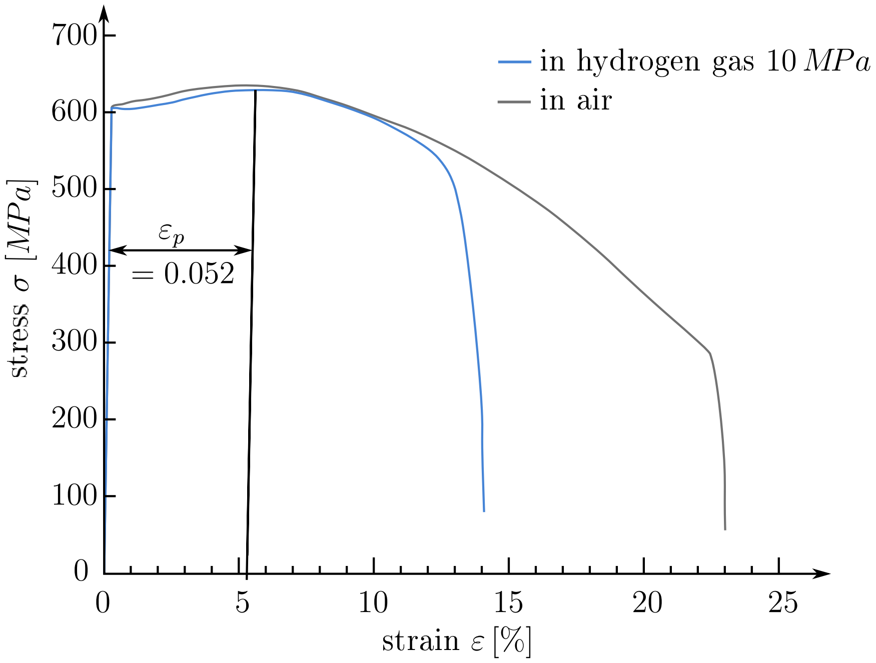

Figure 5.1.: Stress-strain curve of tensile testing; specimens consist of pipeline steel API X70; tests were conducted at room temperature and testing speed $0.002\, mm/s$ (based on the results of Baek et al. [88])

According to chapter 3.2, materials exposed to hydrogen gas show a brittle characteristic after reaching the ultimate tensile strength (UTS). Thus, the plastic strain ε_p until reaching the UTS seems to be an adequate measure for indicating critical behaviour. Here, the plastic deformation from uniaxial tensile testing can be used later on to judge the numerical results whether a critical brittle stage is likely to be exceeded or not.

A summary of the used material parameters for the simulation is presented in Table 5.1, together with the respective sources in literature.

5.2. Definition of numerical pipeline model

When investigating the natural gas pipeline system, the critical areas showed to be the ones with pre-existing damages (compare chapter 3). Therefore, the influence of hydrogen is chosen to be investigated at the example of a pressurized tube with a radial crack.

In Figure 5.2, a three dimensional pipeline with a crack is depicted. Assuming plane strain conditions and using the symmetry of the tube, the three dimensional pipeline can be reduced to a two dimensional model with a crack located at the symmetry plane. In the following, this model is referred to as full-field model (FFM). In literature, instead of the FFM, a surrogate model (SUM) using modified boundary layer formulation is frequently used to investigate hydrogen embrittlement [15, 21, 22]. The SUM is an abstracted specimen where displacement boundary conditions dependent on the stress intensity factor and the T-stress determined from linear elastic calculations of the FFM are applied. A drawback of this abstracted specimen is that parameters as the pipeline dimension, the pressure loading conditions as well as the crack length cannot be directly extracted from this surrogate model. The dimension of this model is not a cut-out of the FFM and thus

Table 5.1.: Material parameters of X70 pipeline steel and further model parameter

Property	Symbol	Value	
elasto-plastic material model			
Young's modulus (extracted from stress-strain curve)	E	207 GPa	[88]
Poisson's ratio	ν	0.3 [−]	[21]
Yield stress (min. measured value)	σ_{y0}	601 MPa	[88]
Material softening parameter, equation (3.10)	ξ	1 [−]	
hydrogen distribution model			
Trap binding energy	W_B	60 kJ/mol	[21]
Diffusion coefficient	D	2 10^{-8} m^2/s	[21]
Partial molar volume of hydrogen	V_H	2 cm^3/mol	[21]
Molar volume host material	V_M	7.116 cm^3/mol	[21]
No. of H-atoms per trap	α	1 [−]	[21]
No. of interstitial lattice sides per host atom	β	1 [−]	[21]
Universal gas constant	R	8.314 $J/mol\ K$	[21]
Temperature	T	300 K	[21]
Avogadro's number	N_A	6.0232 10^{23} $\frac{atoms}{mol}$	[21]

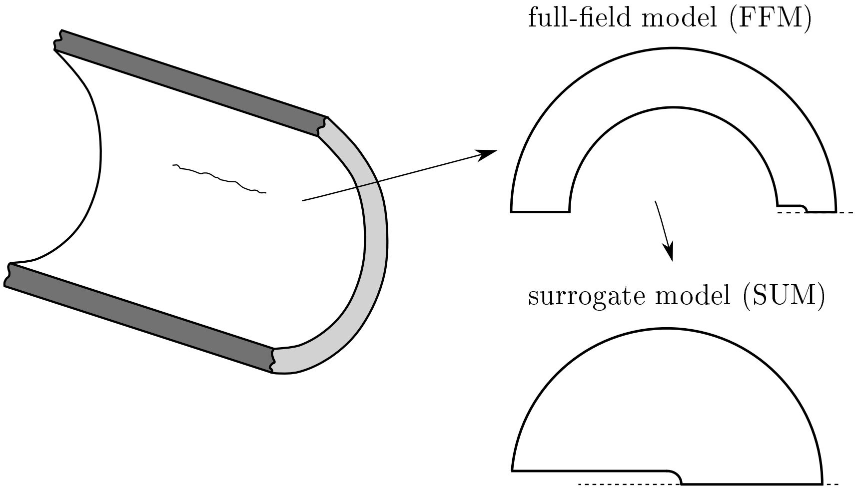

Figure 5.2.: Scheme of pipeline modelling

its dimension can be larger than the crack length in the FFM. If the researcher does not explicitly defines these parameters, the results from literature of hydrogen embrittlement using the SUM cannot straight forwardly be used to judge on the conditions in a real pressurized tube. Nevertheless, to get a better understanding of the processes and to be able to bring various results in line to the findings presented in literature, this abstracted specimen and its applicability shall be discussed in the following.

For simplicity, the mechanical modelling of these two approaches (FFM and SUM) is discussed first. In a second step, the behaviour of the hydrogen concentration is compared. In order to evaluate the agreement of the two models, no effect of hydrogen on the material properties is considered in this chapter. This issue will be discussed in chapter 6.

5.2.1. Mechanical modelling

Within the mechanical continuum model, a linear finite element approach with the von Mises flow criterion is applied (compare chapter 4.3).

The boundary conditions for the FFM and SUM are depicted in Figure 5.3. For both models, the tangential displacement u_2 is set to zero at the symmetry plane. In the FFM (left), an additional zero boundary condition in u_1 direction is applied. At the inner surface of this pipeline model, including the crack surface, a pressure boundary condition P is enforced.

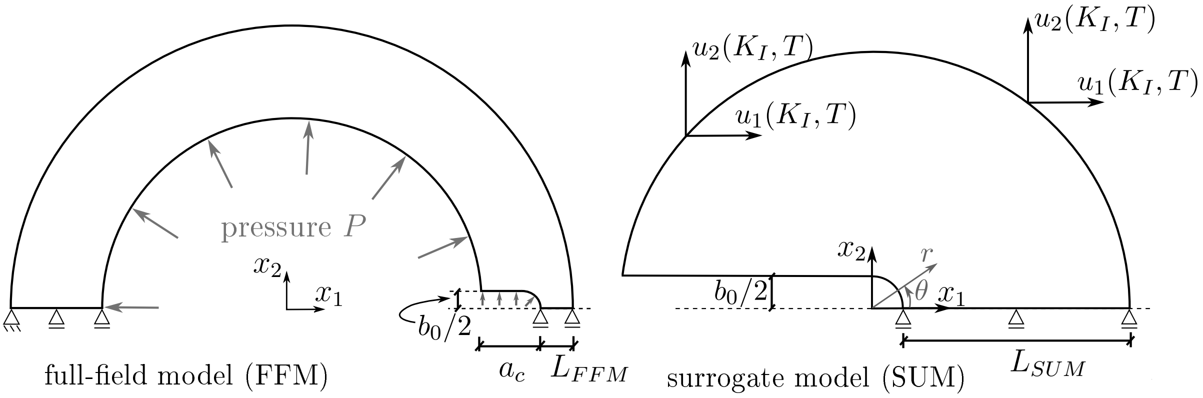

Figure 5.3.: Boundary condition full-field model (left) and surrogate model (right)

In the SUM (right), no pressure boundary conditions are applied. Following the idea of Irwin [89] the size of the plastic zone is assumed to be small compared to the investigated domain size L_{SUM} such that small scale yielding can be applied. Here, the loading is introduced by the displacement boundary conditions at the upper edge, which depends on the stress intensity factor K_I and the T-stress T. The numerical determination procedure of K_I and T is summarized in chapter 2.3. The modified boundary layer formulation is defined in polar coordinates r and θ, such that $u(K_I, T) = u(K_I, T, r, \theta)$. For mode I opening conditions (pure straining, like in a pressurized tube), according to [90, 22], the displacement boundary conditions can be defined to

$$\begin{bmatrix} u_1(K_I,T) \\ u_2(K_I,T) \end{bmatrix} = K_I \, \frac{1+\nu}{E} \, \sqrt{\frac{r}{2\pi}} \begin{bmatrix} \cos\left(\frac{\theta}{2}\right) & \left(\psi - 1 + 2\sin^2\left(\frac{\theta}{2}\right)\right) + \; T \, \frac{1-\nu^2}{E} \, r \, \cos(\theta) \\ \sin\left(\frac{\theta}{2}\right) & \left(\psi + 1 - 2\cos^2\left(\frac{\theta}{2}\right)\right) - \; T \, \frac{\nu\,(1+\nu)}{E} \, r \, \sin(\theta) \end{bmatrix} \tag{5.1}$$

with ψ being equal to $3 - 4\nu$ for plane strain condition.

In a next step, the validity of the SUM is checked by comparing the numerical results with the one determined with the FFM by enforcing a pressure boundary condition of $10\,MPa$. Accordingly, a stress intensity factor of $598\,MPa\sqrt{mm}$ and a T-stress of $164\,MPa$ are applied as boundary conditions on the SUM. The geometric parameters of both models are specified in Table 5.2. The length L_{SUM} of the SUM is chosen to be equal to the uncracked width in the symmetry plane of the FFM L_{FFM} following the idea of [23] (compare Figure 5.3).

Table 5.2.: Geometric modelling parameters

Property	Symbol	Value
full-field model (FFM)		
diameter of pipeline	d	$1,016\,mm$
wall thickness	w	$17.5\,mm$
crack length	a_c	$1\,mm$
crack tip opening displacement	b_0	$6\,\mu m$
surrogate model (SUM)		
length	L_{SUM}	$16.5\,mm$
crack tip opening displacement	b_0	$6\,\mu m$

In Figure 5.4, the hydrostatic stresses are plotted as a function of the radius scaled with the crack tip opening displacement b_0 over the symmetry plane for the FFM as well as the SUM. In order to illustrate the importance of including the T-stress in the boundary condition formulation of the SUM, an additional calculation with $T = 0\,MPa$ is displayed. It can be clearly seen that the stress states calculated using the SUM do not agree with the results of the FFM in the largest part of the field - no matter the choice of the T-stress. This is due to the limitations of the linear elastic theory used to calculate the stress intensity factor and the T-stress and thus the boundary conditions of the SUM in general. By definition, these factors reflect the stress state only in the vicinity of the crack tip (compare chapter 2.3).

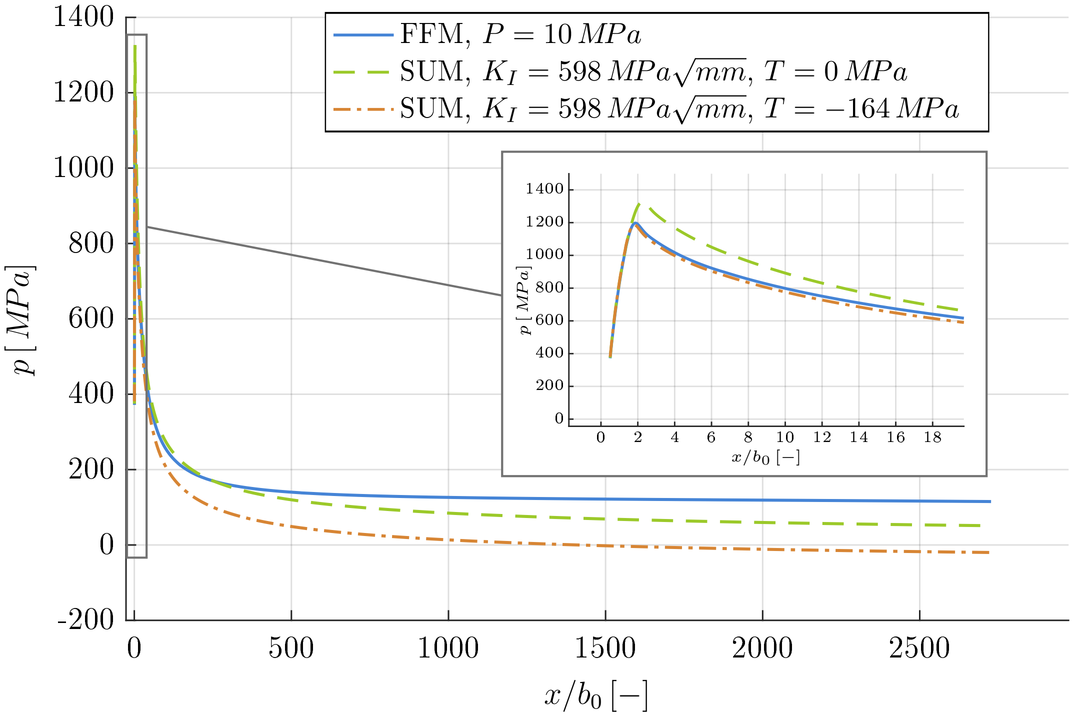

Figure 5.4.: Comparison of hydrostatic stress p of the full-field model (FFM) and the surrogate model (SUM)

However, as the critical domain for failure is directly in front of the crack, only the stress state directly in the vicinity of the crack tip is crucial to evaluate. Here, closely matching results are obtained with FFM and SUM. When the T-stress is included in the boundary layer approach of the SUM, even a better accordance of the results can be obtained. This behaviour agrees well with findings of Dadfarnia et al. [23, 24]. (Note: For lower stress states, such as $1\,MPa$, the higher order term (T-stress) does not necessarily need to be included in the boundary conditions of the SUM to achieve proper results.)
Since the discrepancy of the peak hydrostatic stress is less than $1\,\%$ when comparing the results of the two models, it is concluded that the abstracted specimen (SUM) mirrors the stress state in the vicinity of the crack tip well and thus will be used in the following. Nevertheless, the limitations of the SUM discussed above need to be kept in mind when evaluating further results as well as the results in literature.
The correlations of the pressure within the pipeline and the stress intensity factor as well as the T-stress are displayed in Figure 5.5, using the previously specified modelling parameters. In agreement to the underlying linear theory, consequently a linear relation is found. The advantage of coupling these two models by linear elastic theory is that the boundary condition description is independent from the plastic approximation used for mechanical calculations. When using ideal plasticity or including linear hardening, the same level of accordance between the two models can be achieved.

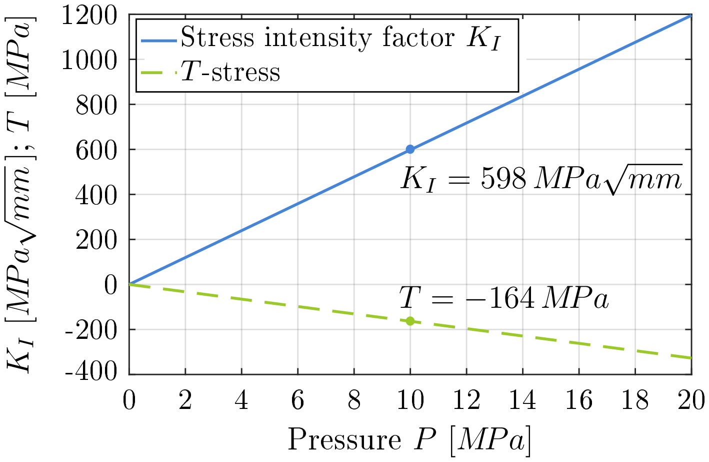

Figure 5.5: Relation of pressure P to the stress intensity factor K_I and the T-stress for a crack length of $1\,mm$

5.2.2. Hydrogen modelling

To simulate the transient hydrogen diffusion problem, a linear finite element approach is applied in space as well as in time for the discontinuous finite element approach. For more details it is referred to chapter 4.2.
It is assumed that at the time step $t = 0\,s$ no hydrogen is within the domain of the FFM and SUM. As depicted in Figure 5.6, a no-flow boundary condition $J = 0$ is applied for both models at the symmetry plane. Furthermore, no flow boundary conditions are also applied at the outer surface of the pipeline, implying that hydrogen cannot diffuse through. This assumption is in agreement with the rather minuscule leakage of hydrogen through the pipeline walls discussed in chapter 1.1.
For the FFM, a Dirichlet boundary condition of $C_{L,0}$ is applied to the inner surface of the pipeline, including the crack surface, as depicted in Figure 5.6, left. The boundary conditions of the SUM are formulated simultaneously (compare Figure 5.6, right).

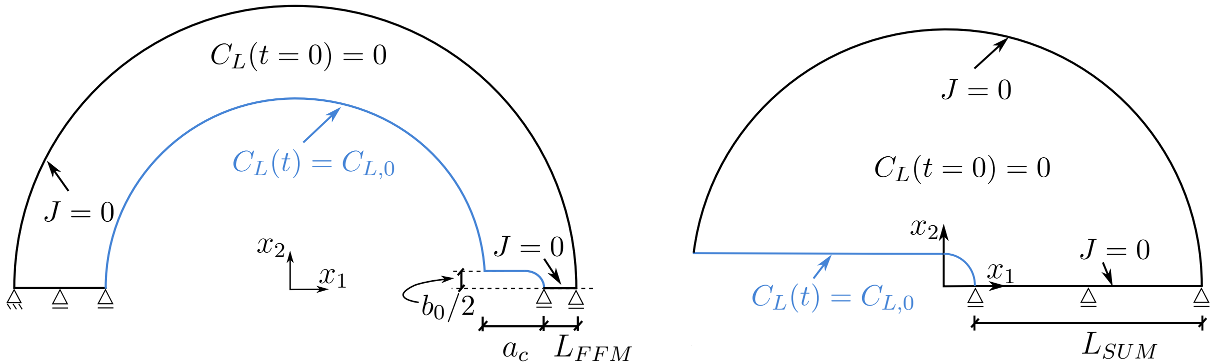

full-field model (FFM) surrogate model (SUM)

Figure 5.6.: Hydrogen boundary conditions of FFM (left) and SUM (right)

To practically realize the Dirichlet hydrogen boundary conditions a correlation of the hydrogen pressure within the tube P and the surface hydrogen concentration $C_{L,0}$ needs to be specified.

One way is to experimentally link the pressure to a surface hydrogen concentration $C_{L,0}(P)$ by volumetrically evaluating the hydrogen absorbed from the metal [91]. In this way, the so-called Sieverts' law was defined for iron and temperatures well above 300 K to [15, 92]

$$C_{L,0} = 6.331 \cdot 10^{28} \sqrt{P}\, e^{-\frac{\Delta H_S}{RT}}, \tag{5.2}$$

where ΔH_S denotes the enthalpy of the solution and P the hydrogen gas pressure within the tube in Pa. Since small hydrogen concentrations are hard to determine by experimental testing and materials at lower temperatures cannot absorb as much hydrogen as at higher ones, Sieverts' law is often extrapolated to smaller temperatures [92].

Another way of determining the surface hydrogen concentration $C_{L,0}$ is to use the fugacity f of the hydrogen molecules and the solubility k of the material [93]

$$C_{L,0} = k\sqrt{f}, \qquad \text{with} \;\; k = k_0\, e^{-\frac{\Delta H_S}{RT}} \tag{5.3}$$

and k_0 denoting the solubility pre-exponential factor.

Since it is not possible to directly measure the fugacity experimentally, the compressibility of the hydrogen gas is used to link the fugacity to the pressure within the tube. Using the results of a compressibility study, the following relation can be derived [93]

$$C_{L,0} = k\sqrt{P\, e^{(z_1/T + z_2)\, P}} \tag{5.4}$$

with the constants z_1 and z_2.

When assuming an ideal gas, the fugacity can be replaced by the pressure and the equation results in Sieverts' law. This assumption is possible at high temperatures or low pressures [93].

Practically speaking, the fugacity acts like an 'effective pressure' and thus this approach reduces the surface hydrogen concentration in comparison to Sieverts' law as depicted in Figure 5.7. The solubility values of the function k are used from pure iron, since no solubility values were available for the pipeline steel X70. The parameters are summarized in Table 5.3.

Table 5.3.: Definition of parameters for surface hydrogen concentration $C_{L,0}$

Property	**Symbol**	**Value**
solubility pre-exponential factor	k_0	$0.82\ m^{-3}Pa^{1/2}$
enthalpy of solution	ΔH_S	$28.6\ kJ/mol$
constant	z_1	$1.51\ 10^{-6}\ K/Pa$
constant	z_2	$-1.04\ 10^{-11}\ 1/Pa$

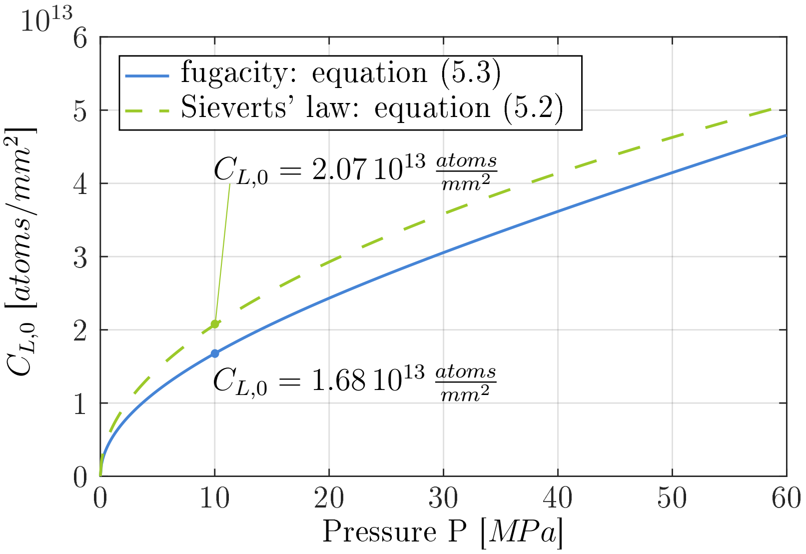

Figure 5.7.: Surface hydrogen concentration $C_{L,0}$ over the pressure P

Krom et al. [93] claimed that hydrogen does not behave as an ideal gas under frequently occurring conditions and used the fugacity to apply the hydrogen concentration boundary condition on their investigated pipeline structure. Nervertheless, Hirth [66] specified that only at pressures higher than 20 MPa the pressure P of Sieverts' law should be replaced by the fugacity f. Therefore, the surface hydrogen concentration in this thesis is calculated by Sieverts' law as it provides the assumption of a conservative worst case scenario.

With the parameters specified in Table 5.3 and Table 5.1 the surface hydrogen concentration for 10 MPa can be determined to 2.07 10^{13} $atoms/mm^2$.

In order to decide if the SUM can depict the hydrogen concentration distribution of the FFM, the results of the lattice hydrogen concentration C_L of the two models are compared at steady state conditions. In Figure 5.8, both approaches show similar trends for the lattice hydrogen concentration. The discrepancy in some distance of the crack tip can clearly be observed. Since the gradient of the hydrostatic stress governs the lattice hydrogen concentration it is not surprising to obtain the same discrepancy as for the hydrostatic stress p. Nevertheless, in the vicinity of the crack tip the two graphs are very close with a deviation of merely 2 %. Therefore, the SUM is adopted as a reasonable abstracted specimen.

One major advantage of the SUM is the reduced number of degrees of freedom. While for the mechanical calculations with the FFM a comparatively coarse meshing over the pipeline wall thickness is well suitable in some distance to the crack tip, problems arise when the boundary hydrogen concentration is introduced at the inner surface of the

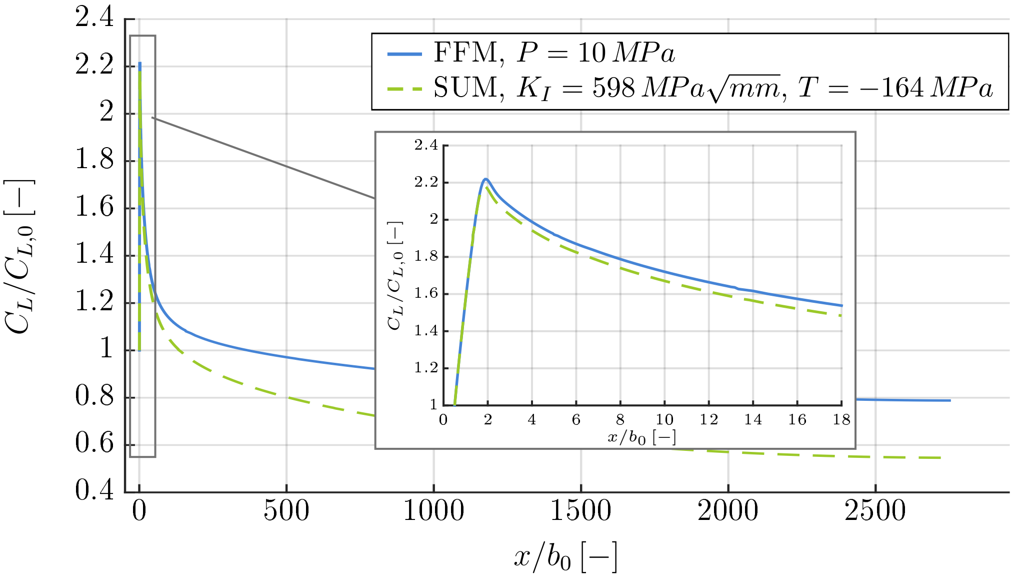

Figure 5.8.: Lattice hydrogen concentration C_L normed by the boundary hydrogen concentration $C_{L,0}$ at steady state conditions plotted over distance to the crack tip over the symmetry plane for the SUM and FFM. The distance to the crack tip is normed by the crack tip opening displacement b_0.

pipeline wall. Then, the gradient is too steep to be captured by a relatively coarse mesh. Nevertheless, reasonable results can be obtained in the crack tip region when applying a finer mesh. A mesh refinement over the whole pipeline domain however would substantially increase the numerical costs. Therefore, the reduced model is considered as an adequate alternative. In order to determine the stress intensity factor and the T-stress a course mesh in the uncracked pipeline region is well suitable.

5.2.3. Definition of surrogate model domain size

In order to properly relate the SUM with the response of the FFM, the sensitivity of the results to a variation of the domain size L_{SUM} needs to be investigated.
As a first attempt, the domain size L_{SUM} was chosen to be the length of the uncracked pipeline wall thickness L_{FFM} following the idea of Dadfarnia et al. [23]. This assumption gives a comparatively large semicircle area of the surrogate model especially for short cracks. Thus, choosing a smaller domain size compared to the uncracked pipeline wall L_{FFM} would be numerically more efficient.
In order to vary the domain size, the following limitation of the surrogate model needs to be kept in mind. Following the approach of Irwin [89], the size of the plastic zone needs to be small compared to the investigated domain size L_{SUM} such that small scale yielding conditions can be applied.
The plastic zone of the in chapter 5.2.2 investigated loading conditions expands to about $0.04\,mm$ in front of the crack tip and is therefore highly localized. Consequently, domain sizes varying from $L_{SUM} = 2\,mm$ to $L_{SUM} = 20\,mm$ are investigated in the following.
In a first step, the effect on the hydrostatic pressure p with changing L_{SUM} is investigated. The results are plotted in Figure 5.9 together with the reference solution of the FFM. It is noticed that with decreasing domain size L_{SUM}, the hydrostatic pressure increases and the results approach the solution of the FFM.

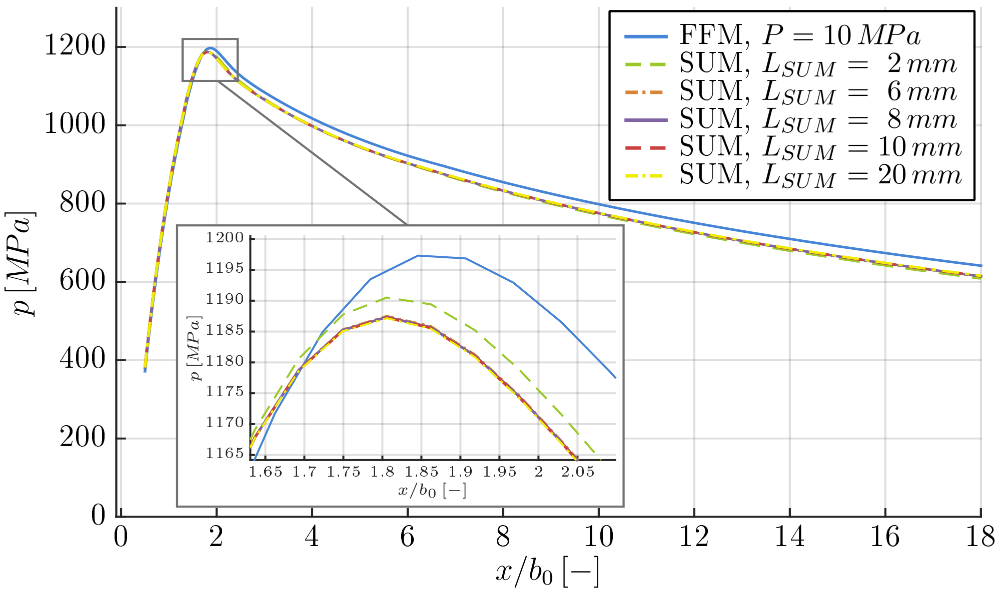

Figure 5.9.: Hydrostatic pressure p over distance to the crack tip normalized by b_0 for varying domain sizes L_{SUM} using the surrogate model analogous to a crack length of $1\,mm$ and $P = 10\,MPa$ ($K_I = 598\,MPa\sqrt{mm}$, $T = -164\,MPa$) and the according FFM reference solution

In addition to the hydrostatic pressure, the influence of the domain size L_{SUM} on the plastic behaviour shall be investigated. In Figure 5.10, the equivalent plastic strain $\bar{\varepsilon}^p$ is depicted for different domain sizes along the symmetry plane. Here, a different trend can be observed than for the hydrostatic stress as with decreasing domain size, the equivalent plastic strain diverges from the FFM reference solution.

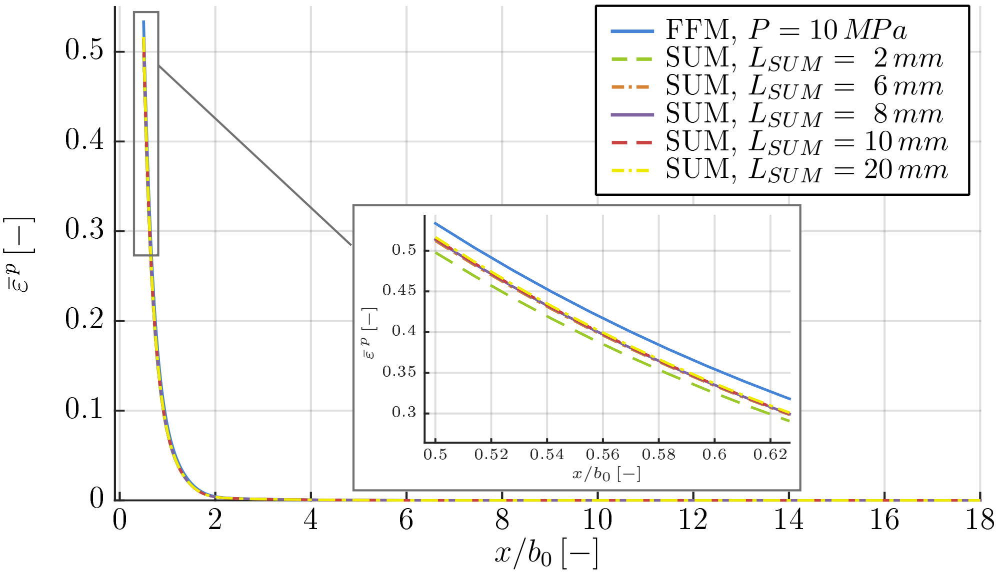

Figure 5.10.: Equivalent plastic strain $\bar{\varepsilon}^p$ over distance to the crack tip normalized by b_0 for varying domain sizes L_{SUM} using the surrogate model analogous to a crack length of $1\,mm$ ($K_I = 598\,MPa\sqrt{mm}$, $T = -164\,MPa$) and the FFM reference solution

Both plots, the one of the hydrostatic stress and the equivalent plastic strain, have in common that the results converge with increasing domain size. Therefore, a converged domain size of $L_{SUM} = 8\,mm$ is chosen.
Apart from the purely mechanical properties, the applicability of the smaller domain size needs to be checked also for the hydrogen distribution model. In Figure 5.11, the lattice hydrogen concentration C_L is depicted over the symmetry plane for varying domain sizes and the reference hydrogen distribution of the FFM. The lattice hydrogen concentration C_L for the domain size of $L_{SUM} = 8\,mm$ varies less than $1\,\%$ from the result of the FFM solution. Thus, this model approximates the hydrogen distribution of the FFM better than a SUM with a domain size of $L_{SUM} = 16.5\,mm$ in the vicinity of the crack tip, while the mechanical responses for both were coinciding (see above).
This increase of hydrogen concentration with decreasing domain size can be explained by the definition of the steady state conditions. Steady state of the hydrogen distribution is assumed when the peak of the hydrogen varies less than 0.1% within one hour. While the stress driven distribution of the hydrogen is rather rapid, the diffusion process of hydrogen inside the material is comparatively slow. Since the hydrostatic stress decreases with distance to the crack tip, here the slow diffusion process is dominant. Thus, in smaller domain sizes, the applied no flow boundary condition influences the results of the peak solution slightly. Nevertheless, in total, a domain size of $L_{SUM} = 8\,mm$ leads to a better approximation of the FFM results.
Since a domain size of $L_{SUM} = 8\,mm$ does not alter the mechanical properties and leads to a better approximation of the lattice hydrogen concentration, this domain size is adopted in the following.

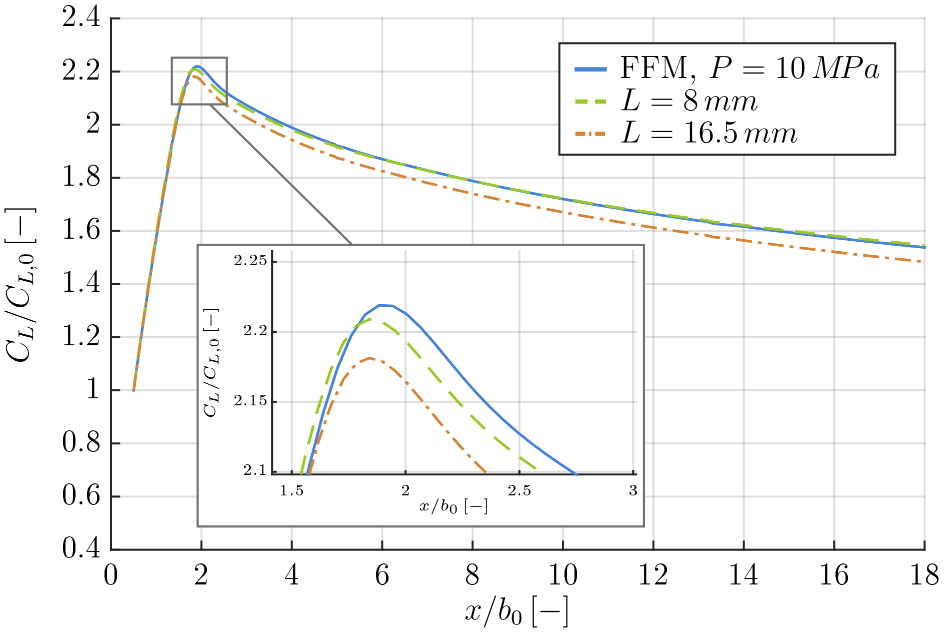

Figure 5.11.: Lattice hydrogen concentration C_L over distance to the crack tip normalized by b_0 for varying domain size L_{SUM} using the surrogate model analogous to a crack length of $1\,mm$ ($K_I = 598\,MPa\sqrt{mm}$, $T = -164\,MPa$) and the FFM reference solution

6. Results

In this chapter, the results of the coupled elasto-plastic model with the transient hydrogen distribution approach are presented. First of all, the hydrogen distribution within the domain of the surrogate model (SUM) is discussed on the basis of a fixed mechanical loading condition. Here, as the focus lies on understanding local hydrogen accumulation in general, the influence of hydrogen on the material properties is not yet considered. In a next step, possible softening approaches, presented in chapter 3.4.2, are evaluated reflecting hydrogen embrittlement in the accordance with the Hydrogen Enhanced Localized Plasticity (HELP) mechanism. Afterwards, the impact of crack length and thus the general mechanical load level on hydrogen embrittlement is investigated.

6.1. Hydrogen movement and accumulation due to mechanical loads

In order to investigate the effect of the mechanical stress and plastic strain field on the hydrogen concentration, a representative pipeline tube of the natural gas pipeline system with an internal pressure of $10\,MPa$ and a radial crack of the length of $1\,mm$ is assumed. The analogous loading conditions for the SUM were determined to $K_I = 598\,MPa\sqrt{mm}$ and $T = -164\,MPa$ in a preceding simulation in chapter 5.2.1. The initial hydrogen concentration at the surface is $C_{L,0} = 2.07\ 10^{13}\,\frac{atoms}{mm^2}$, according to Sieverts' law. As mentioned above, this chapter focuses solely on the hydrogen distribution according to the mechanical input variables and no effect on the yield stress is considered.

The hydrogen concentration in lattice sites C_L essentially depends on the hydrostatic stress p. The hydrostatic stress strains the lattice of the steel dilatationally and thus increases the spacing among the molecular lattice. As a consequence of the occurring higher spacing between the molecular grid of the steel, the hydrogen can accumulate more easily at places of high hydrostatic stress fields. Inside the material lattice, the hydrogen moves into the direction of higher molecular spacing and thus drifts along the gradient of the hydrostatic stress. In a continuum mechanics context, the gradient of the hydrostatic stress can be mathematically interpreted as an advective driving force (compare chapter 3.4.1). Thus, the hydrogen moves inside the material into the direction of the gradient of the hydrostatic stress and accumulates at hydrostatic stress peaks.

In Figure 6.1, the hydrostatic pressure p is depicted. Figure 6.2 gives the resulting lattice hydrogen concentration C_L. It is noticed that the distributions in both graphs show a good agreement. The localized peak of the hydrostatic stress agrees well with the maximal lattice hydrogen concentration.

Besides the lattice hydrogen concentration C_L also the hydrogen concentration in trapping sites C_T needs to be determined.

This trapped hydrogen concentration is mainly governed by the available trapping sites. These trapping sites, such as dislocations, are in a continuum mechanics view considered

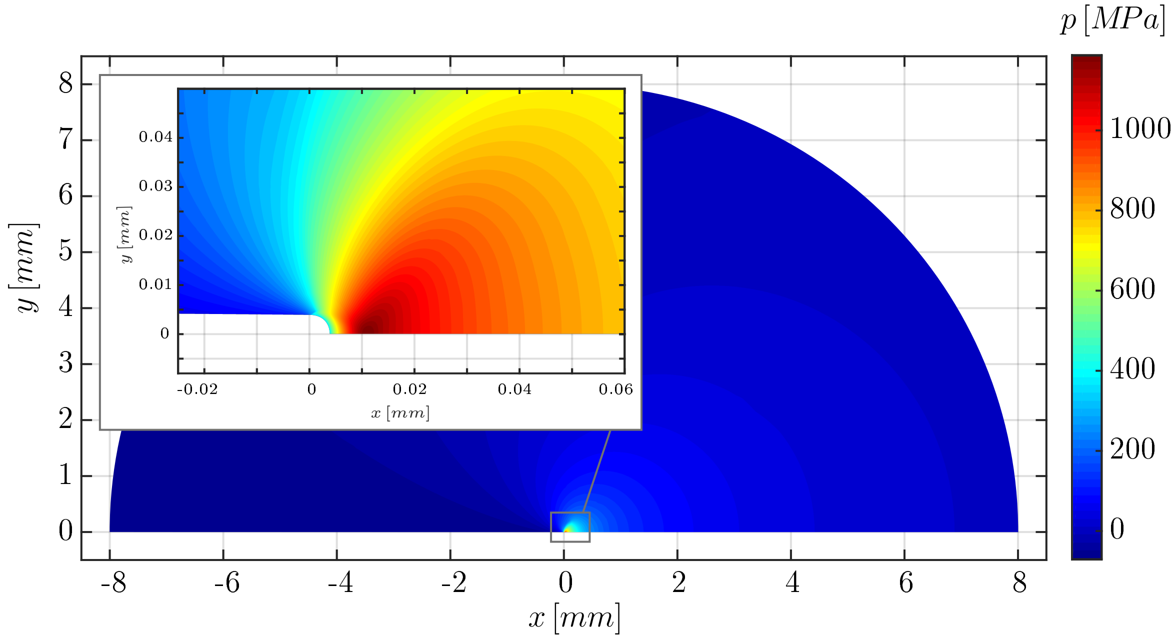

Figure 6.1.: Hydrostatic pressure p using the surrogate model analogous to a crack length of $1\,mm$ and $P = 10\,MPa$ ($K_I = 598\,MPa\sqrt{mm}$, $T = -164\,MPa$)

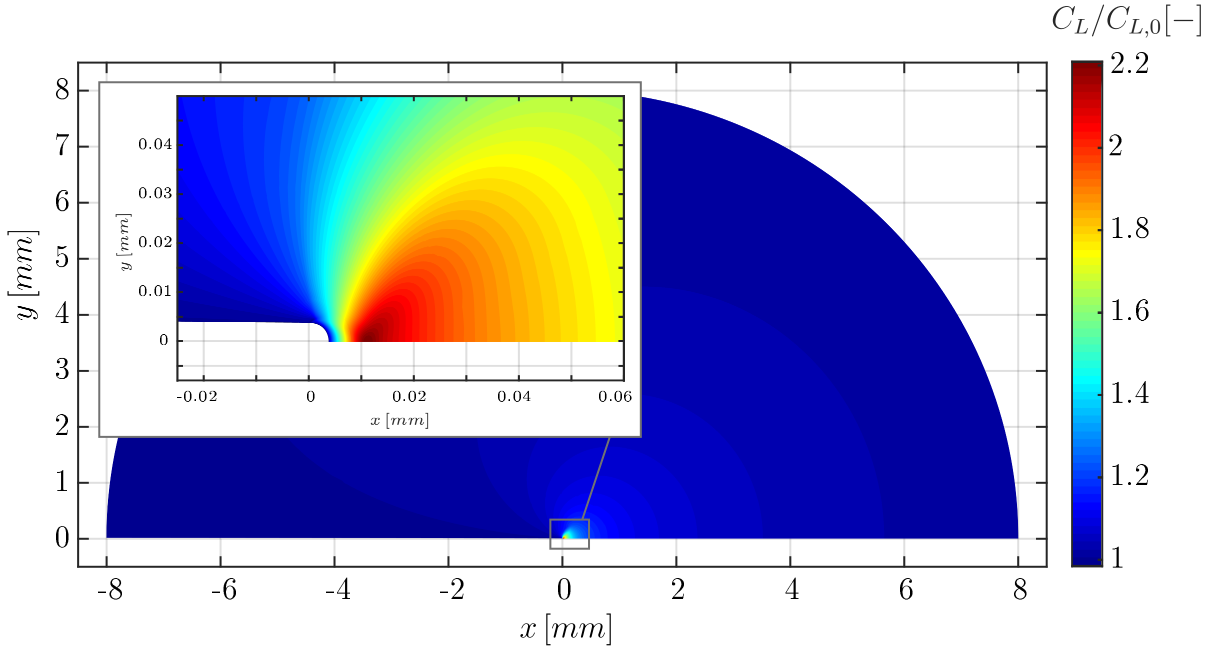

Figure 6.2.: Lattice hydrogen concentration C_L normed with the boundary concentration $C_{L,0}$ at steady state conditions using the surrogate model analogous to a crack length of $1\,mm$ and $P = 10\,MPa$ ($K_I = 598\,MPa\sqrt{mm}$, $T = -164\,MPa$)

as the plastic strain (compare chapter 2.2). Thus, at high plastic strains more dislocations accumulate and consequently also an increasing trapped hydrogen population can be found. Here, the available traps are formulated in the dependency on the equivalent plastic strain. A very localized plastic deformation can be found directly at the blunted crack tip where the equivalent plastic strain $\bar{\varepsilon}^p$ reaches its maximum (compare Figure 6.3). This maximum of plastic deformations rapidly decreases with distance to the crack tip. Since the hydrogen accumulates at the trapping sites created by plastic deformations, the same localized effect is noticed for the trapped hydrogen concentration C_T in Figure 6.4.

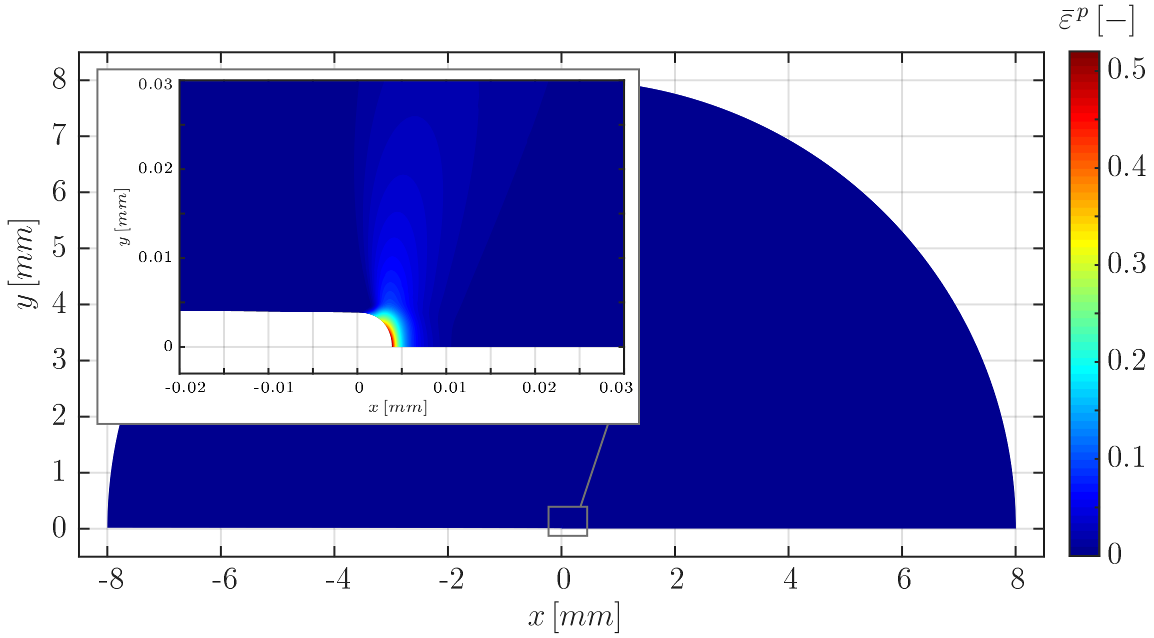

Figure 6.3.: Equivalent plastic strain $\bar{\varepsilon}^p$ using the surrogate model analogous to a crack length of $1\,mm$ and $P = 10\,MPa$ ($K_I = 598\,MPa\sqrt{mm}$, $T = -164\,MPa$)

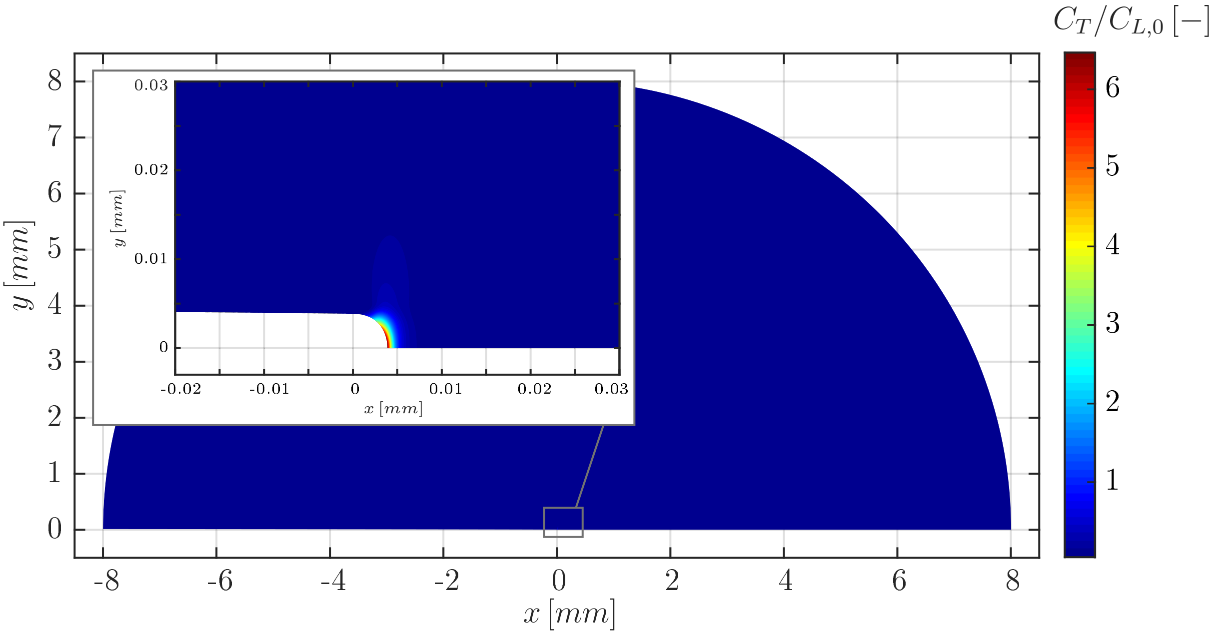

Figure 6.4.: Trapped hydrogen concentration at steady state conditions using the surrogate model analogous to a crack length of $1\,mm$ and $P = 10\,MPa$ ($K_I = 598\,MPa\sqrt{mm}$, $T = -164\,MPa$)

The concentration of the trapped hydrogen C_T with its maximum at the surface of the blunted crack tip is roughly three times higher than the hydrogen accumulated in lattice sites C_L with its maximum closely in front of the crack tip. Still, since both hydrogen populations show generally comparable peak levels, it consequently has to be assumed that both populations directly influence the material properties. The described trends agree well with results available in literature [21, 94]. As a next step, the effects of the proposed softening approaches considering the HELP mechanism presented in chapter 3.4.2 are investigated.

6.2. Effect of hydrogen on material properties and stress states

In this thesis, the HELP mechanism was identified to be the dominant hydrogen embrittlement mechanism. Therefore, a localized enhanced plastic behaviour in dependency of the hydrogen concentration needs to be considered within the continuum model. Three approaches to enhance the plasticity in the presence of hydrogen were presented in chapter 3.4.2 by introducing hydrogen dependent reductions of the initial material yield stress σ_{y0}. An overview of these three approaches is given in Table 6.1. In the following, the effects of these softening approaches on the material stress and strain fields are discussed at the example of the same surrogate model as in the previous chapter 6.1, again with a loading scheme analogous to a $1\,mm$ crack in a pressurized pipeline of $10\,MPa$.

Table 6.1.: Summary of the three softening approaches discussed in chapter 3.4.2

	Equation	**Applied factor [-]**	**Author**
S1	$\sigma_{y0}(c) = [(\xi - 1)c + 1]\,\sigma_{y0}$	$\xi = 0$	Sofronis et al. [78]
S2	$\sigma_{y0}(c) = (\zeta\,c + 1)\,\sigma_{y0}$	$\zeta = -10000$ $\zeta = -20000$	Kotake et al. [13]
S3	$\sigma_{y0}(c) = [(\xi - 1)c_{T,r} + 1]\,\sigma_{y0}$	$\xi = 0$	Dadfarnia et al. [26]

The parameter c is used in the softening approaches S1 and S2 to control the yield stress reduction (compare Table 6.1). As mentioned in chapter 3.4.2, c relates the total hydrogen concentration, C_L and C_T, to the available trapping sites N_L and can therefore be interpreted as the theoretical amount of lattice sites occupied with hydrogen.

Softening approach S1

When it comes to softening approach S1, the value of c scales directly with the initial yield stress σ_{y0} as ξ is restricted to the interval $[0, 1]$. To get a better understanding of the dimension of this parameter, the distribution in the domain is calculated using the results of the previous chapter where no softening approach was applied. In case of $\xi = 0$ the material is assumed to be maximally susceptible to hydrogen and the reduction of the yield stress scales directly with the value of c. The resulting distribution of the parameter c is depicted in Figure 6.5. Clearly, the maximum peak of the trapped hydrogen concentration can be observed at the crack tip as well as a local increase of c in a certain distance to the crack tip, caused by a peak of the lattice hydrogen concentration. The contribution of the trapped hydrogen concentration slightly dominates the reduction of the yield stress compared to the effect of the lattice hydrogen concentration. Nevertheless, the determined values of c are of the order of 10^{-6} which leads to a $10^{-4}\,\%$ reduction of the initial material yield stress σ_{y0}. Thus, no practical reduction of the yield stress is determined when applying softening approach S1. Only in case of an unrealisticly high hydrogen surface concentration, this softening approach shows a local softening effect as demonstrated by Möhle et al. [95].

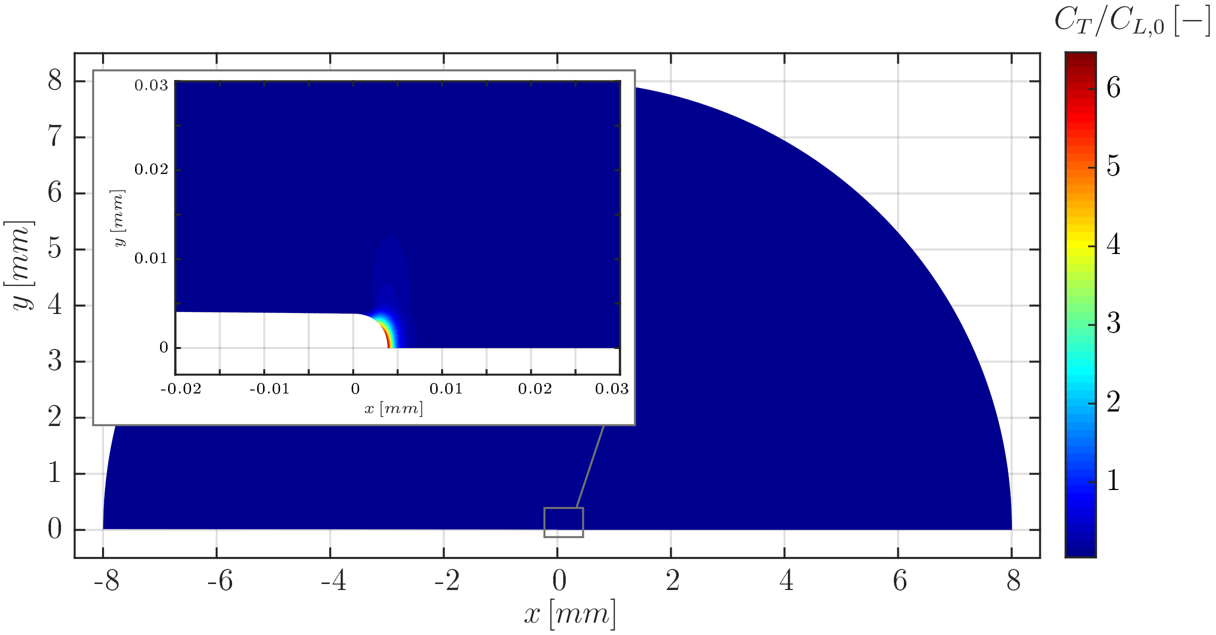

Figure 6.5.: Distribution of factor c using the softening approach S1 at steady state conditions. The loading conditions of the surrogate model is chosen to be analogous to a crack length of $1\,mm$ exposed to a pressure of $10\,MPa$ ($K_I = 598\,MPa\sqrt{mm}$, $T = -164\,MPa$).

There are two possibilities to interpret this result. On the one hand, it could be concluded that hydrogen does not embrittle the material. As discussed in the following, this has to be judged as highly unlikely. On the other hand, it could be questioned whether the modelling approach S1 is suited at all to depict the influence of hydrogen on material properties.

In order to classify the numerical results, the stress-strain curve for the investigated pipeline material (already given in Figure 5.1) shall be discussed. Based on the experimental findings presented in chapter 3.2.1, hydrogen affects the material properties macroscopically when reaching the ultimate tensile strength (UTS). Since the applied material model does not properly capture the nonlinear material behaviour after yielding, the UTS cannot be used for evaluation of hydrogen influence. However, interpreting the according plastic deformations in the vicinity of the experimentally obtained ultimate tensile stress might give a hint, whether hydrogen influences the material properties or not. From Figure 5.1, the critical value of the plastic strain can be identified to 0.052. Nevertheless, this macroscopically determined value cannot depict the more localized effects of the coexisting surface crack formation during necking.

Since no uniaxial loading conditions are present in front of the crack tip, the equivalent plastic strain $\bar{\varepsilon}^p$ is taken as a comparative value. Here, it has to be kept in mind that the macroscopic plastic strain of a uniaxial tensile test is compared to a numerically determined local equivalent plastic strain. Furthermore, the assumed ideally plastic material behaviour leads to a conservative estimation of the plastic straining. Nevertheless, the value of the uniaxial tensile test can at least give a hint at which plastic straining level the hydrogen starts to influence the material properties, even when the highly localized softening effect cannot be depicted in detail.

The numerically calculated equivalent plastic strain with its maximum at about 0.51 is roughly one order of magnitude larger than the experimental determined critical macroscopic plastic strain (compare Figure 6.3). Obviously, parity of these two plastic strains cannot be expected since the brittle effect of hydrogen coexists with surface crack formation and thus highly localized embrittlement effects, as described above. Nevertheless, since the numerically determined plastic strain extensively exceeds the experimentally determined initiation strain, it is highly likely that hydrogen has an influence on the material properties in the prevalent case.

However, when observing such high plastic strain values, it has to be checked whether mechanical crack propagation could take place. As in this thesis, the aim is to demonstrate the influence of hydrogen on the material and as the observed plastic strain values agree well with according studies in literature ($\bar{\varepsilon}^p = 0.3$ to $\bar{\varepsilon}^p = 1.7$, [21, 94]), the possibility of crack propagation is not investigated any further at this point.

To conclude this section, it is stated that the softening approach S1 does not properly reflect the hydrogen influence.

Softening approach S2

In a next step, the softening approach S2 shall be investigated. Here, also the variable c serves as a primal parameter for the reduction of the yield stress. In contrast to approach S1 with the parameter ξ, here a material dependent parameter ζ is applied which is not restricted to the interval $[0, 1]$. The material factor ζ directly scales the parameter c to account for the level of material softening (compare Table 6.1). However, since no suitable experimental data is available, the factor ζ is exemplarily set to -10000 and -20000 for better comparability with literature [13]. Here, the parameter ζ is chosen such that the yield stress is reduced in the vicinity of the crack tip while having a negligible effect in the rest of the domain. The negative sign indicates that the material is softening, implying a yield stress reduction. It has to be noted that due to academic reasoning of choice of values for ζ, the following results can only be interpreted qualitatively.

In Figure 6.6, left, the factor c is plotted at the symmetry plane of the SUM over the distance to the crack tip for $\zeta = -10000$ and $\zeta = -20000$ as well as for a reference solution with $\zeta = 0$, where hydrogen does not affect the initial yield stress σ_{y0}. The factor c shows the same trend as discussed above. A maximal value can be observed at the crack tip, followed by a steep decline resulting from the trapped hydrogen concentration C_T. In further distance from the crack tip, a minor local peak is noticed, reflecting the local peak of the lattice hydrogen concentration C_L. The difference to approach S1 lies in the scaling of c with the material dependent parameter ζ. These two parameters together govern the percental reduction of the initial material yield strength σ_{y0}. As the factor c almost remains the same for the different values of ζ, the amount of percental reduction of the initial yield stress is dominated by the parameter ζ.

The hydrogen driven reduction of the yield stress can well be evaluated using the von Mises stress distribution, since an ideally plastic material and a von Mises flow criterion

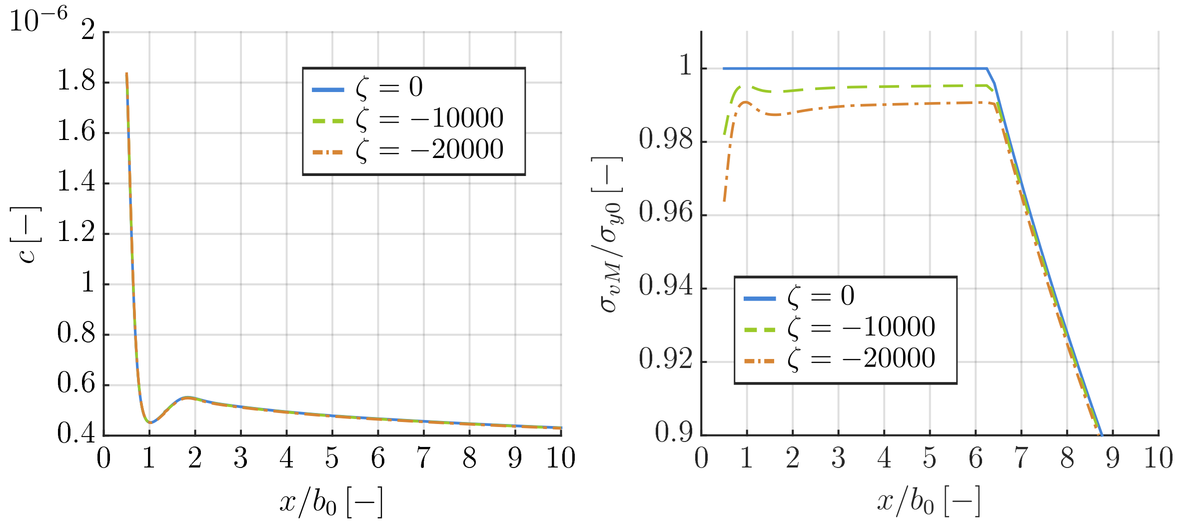

Figure 6.6.: Factor c, left, and the von Mises stress σ_{vM} normalized by the initial yield stress σ_{y0}, right, is plotted with distance to the crack tip using the softening approach S2 at steady state conditions. The surrogate model is chosen to be analogous to a crack length of $1\,mm$ and $P = 10\,MPa$ ($K_I = 598\,MPa\sqrt{mm}$, $T = -164\,MPa$).

is applied in this thesis. In Figure 6.6, right, the von Mises stress σ_{vM} normalized by the initial yield stress σ_{y0} is depicted over the symmetry plane. With decreasing ζ, a decrease of the von Mises stress can be observed which implies a reduction of the yield stress. The general trend of the curve with local minima and maxima mirrors the reverse of the distribution of factor c. At the blunted crack tip, the maximum value of factor c is noticed, correlating to the maximum reduction of the yield stress σ_{y0}. Here, a reduction of two percent and four percent can be observed correlating to $\zeta = -10000$ and $\zeta = -20000$, respectively. Accordingly, the second peak of c can be related to the second local reduction of the yield stress. The plastic zone size rises slightly with decreasing ζ.

The localized reduction of the yield stress, especially at the blunted crack tip, reflects the idea of an enhanced localized plasticity effect in the presence of hydrogen which is in agreement with the HELP mechanism.

As discussed previously, hydrogen embrittlement reduces the yield stress according to the HELP mechanism. This in turn influences the mechanical stress and strain fields and since these quantities are again coupled to the hydrogen distribution itself, the latter should also be altered. However, since the parameter c depends on the lattice and trapped hydrogen concentration and does not change noticeably with an increasing softening effect, also the change of the distribution of hydrogen in the domain will be rather minor in the prevalent case. Nevertheless, albeit quantitatively small in this exemplary study, a general trend can be clearly identified and will therefore be discussed in the following.

As a consequence of the reduction of the initial material yield stress, the material cannot bear the same stress states as before and these stresses need to be dissipated by plastic deformations. Thus, it is not surprising that the equivalent plastic strain $\bar{\varepsilon}^p$ increases with decreasing ζ as shown in Figure 6.7, left. Since the maximum bearable stresses are locally reduced, the actual stress level decreases. As a consequence, the hydrostatic stress field p decreases with decreasing ζ as depicted in Figure 6.7, right.

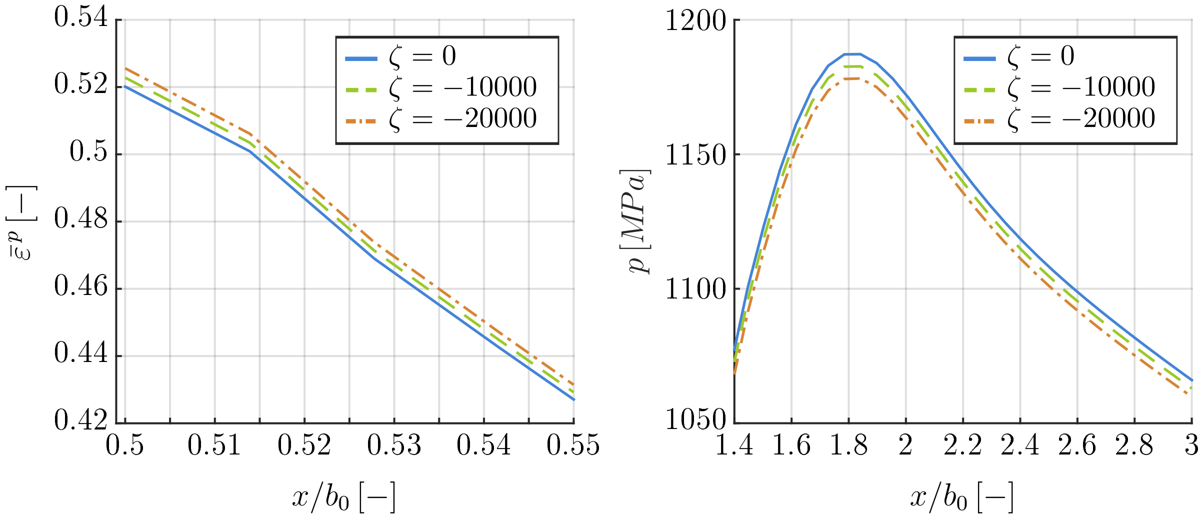

Figure 6.7.: The equivalent plastic strain $\bar{\varepsilon}^p$ (left) and the hydrostatic stress p (right) plotted with distance to the crack tip using the softening approach S2 with varying ζ at steady state conditions. The surrogate model is chosen to be analogous to a crack length of $1\,mm$ and $P = 10\,MPa$ ($K_I = 598\,MPa\sqrt{mm}$, $T = -164\,MPa$).

As discussed above, a two-way coupling of material properties and hydrogen concentration is implemented. Therefore, the steady state solutions for the trapped and lattice hydrogen concentration C_L and C_T also vary with the material dependent softening parameter ζ.
The increase of the equivalent plastic strain $\bar{\varepsilon}^p$ is micromechanically interpreted as the formation of new dislocations and thus the creation of new trapping sites. Therefore, the increasing equivalent plastic strain in turn leads to a raised trapped hydrogen concentration C_T. In consequence, the trapped hydrogen concentration increases with decreasing ζ (compare Figure 6.8).
The lattice hydrogen distribution is prevalently affected by the hydrostatic stress field. If the hydrostatic stress decreases, a reduction of the straining of the molecular grid is implied. Thus, also the lattice hydrogen concentration decreases with decreasing ζ as shown in Figure 6.8.
To summarize the findings, a local reduction of the yield stress according to the softening approach S2 and thus an increase of local plasticity could be shown, being in agreement with the assumptions of the HELP mechanism. In turn, the steady state results of the hydrogen concentrations C_L and C_T changed with the changing mechanical stress and strain fields. Given steady state conditions, the trapped hydrogen concentration C_T increases while the lattice hydrogen concentration C_L decreases for decreasing ζ. Nevertheless, the observed changes are quantitatively rather small and directly scale with the parameter ζ. Here, when choosing lower values of ζ, the observed trends will get more pronounced and will lead to a further localization of plastic straining at the blunted crack tip. However, a reasonable quantification of the amount of softening (and thus the parameter ζ) has to be performed by the means of experiments.

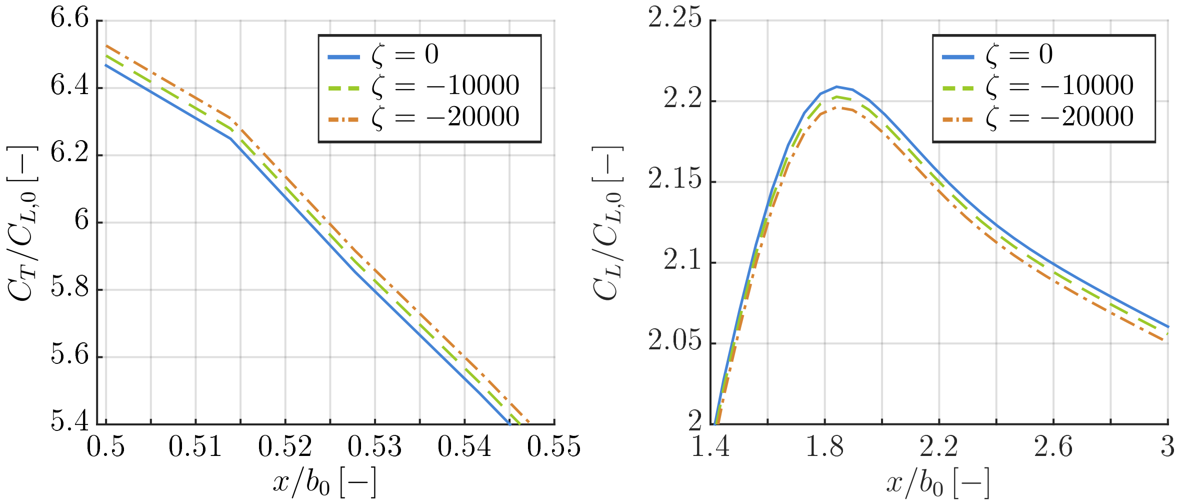

Figure 6.8.: Trapped hydrogen concentration C_T (left) and lattice hydrogen concentration C_L (right) plotted over the distance to the crack tip using the softening approach S2 with varying ζ at steady state conditions. The surrogate model is chosen to be analogous to a crack length of $1\,mm$ and $P = 10\,MPa$ ($K_I = 598\,MPa\sqrt{mm}$, $T = -164\,MPa$).

Softening approach S3

Unfortunately, a general disadvantage of softening approach S2 is that the material parameter ζ actually cannot be straight-forwardly measured in experiments. At this point, the underlying idea of approach S3 seems attractive where the factor $c_{T,r}$ relates a numerically determined hydrogen concentration to a defined reference hydrogen concentration for quantifying the amount of softening. In case the reference concentration would be interpreted as a critical hydrogen concentration at which the material embrittles, this would be a more depictive parameter. Still, to experimentally specify such a critical material dependent hydrogen concentration is difficult since no proper testing schemes exist to determine the hydrogen distribution within the material domain. Here, further investigations could prove to be promising. In literature, consequently no critical hydrogen concentration could be determined when the approach was first presented [26]. Instead, the softening effect was numerically investigated using a reference hydrogen concentration chosen to be equal to the applied boundary value concentration $C_{L,0}$.

In the following, the softening approach S3 shall be briefly discussed. The main difference to the prior approaches is that solely the trapped hydrogen concentration C_T is assumed to embrittle the material. Similar to softening approach S1, a parameter ξ, scaling from zero to one, is used to specify the amount of embrittlement. The ratio $c_{T,r} = C_T/C_{L,0}$ results in a scalar physically representing how many times the trapped hydrogen concentration C_T exceeds the boundary value concentration $C_{L,0}$. In case the trapped hydrogen concentration C_T is equal to the reference hydrogen concentration, here $C_{L,0}$, the factor $c_{T,r} = 1$. This implies that the parameter ξ governs the amount of softening. Thus, choosing $\xi = 0.97$ would result in a 3% reduction of the yield stress. To estimate the amount of embrittlement in the prevalent case, the maximum value of the trapped hydrogen concentration determined in chapter 6.1, where no softening approach was applied, is exemplarily chosen. According to Figure 6.4, the trapped hydrogen concentration C_T normalized with

$C_{L,0}$, which, as stated above, is assumed to be equal to $c_{T,r}$, can be identified to be $c_{T,r} \approx 6$ at the blunted crack tip. With $c_{T,r} = 6$, the reduction of the initial yield stress is determined to be six times the ξ-driven 3% modification, resulting in a total yield stress reduction of 18%.
This approach is just presented exemplarily, since the two parameters C_r and ξ cannot be straight forwardly tied to experimental data. Since softening approach S3 introduces an additional and rather arbitrary parameter (the choice of C_r) compared to the softening approach S2, approach S3 is discarded. Furthermore, as stated above, approach S3 assumes that only the trapped hydrogen concentration is considered to embrittle the material. As shown previously, also the lattice hydrogen concentration C_L contributes a non-negligible part to the total hydrogen concentration, even though C_L decreases with increasing material softening. In a further study however, the lattice hydrogen concentration could be easily added to the approach in the form of $(C_L + C_T)/C_r$.

In this chapter, three different softening approaches were presented.
The first softening approach S1 was shown to not alter the material properties notably. Since the experimental data hinted that an effect of hydrogen on the material properties should be present at the actual loading conditions, an alternative approach was discussed. For the second approach S2, different values for the material dependent parameter ζ were chosen exemplarily such that a local reduction of the yield stress was achieved. The effect of reducing the yield stress on the mechanical properties as well as the hydrogen distribution was discussed. The coupling of hydrogen and material properties could be clearly demonstrated. Trends of the different primal coupling parameters with a locally decreasing yield stress could be identified. However, experiment based material characterization for ζ is still lacking.
In a third step, softening approach S3 was discussed, being based on a reference hydrogen concentration to specify the amount of local softening as a descriptive way of formulating hydrogen embrittlement. As again no experimental data are available to specify the material dependent softening parameter, the second approach is favoured since only one material dependent parameter needs to be specified.
In the next chapter, softening approach 2 is applied to investigate the effect of higher crack lengths and therefore an increase in general loading on the amount of local softening.

6.3. Influence of pre-existing defect size on hydrogen embrittlement

In this chapter the crack length is varied to identify the sensitivity of the amount of local softening to different structural load levels. Here, the softening approach S2, as discussed in chapter 6.2, is adopted using a softening parameter of $\zeta = -20000$. As already discussed above, all results can only be interpreted qualitatively since the material parameter ζ could not be determined from experimental investigations (compare chapter 6.2).
The boundary conditions of the SUM are determined analogously to the ones in chapter 5.2.1 for a pipeline under a $10\,MPa$ hydrogen atmosphere. The relationship of the pressure P and the according boundary conditions are depicted in Figure A.1. For all models a domain size of $L_{SUM} = 8\,mm$ is applied.
In order to investigate the influence of the crack length a_c on the yield stress reduction, once more the von Mises stress σ_{vM} is examined. Thus, the von Mises stress normalized

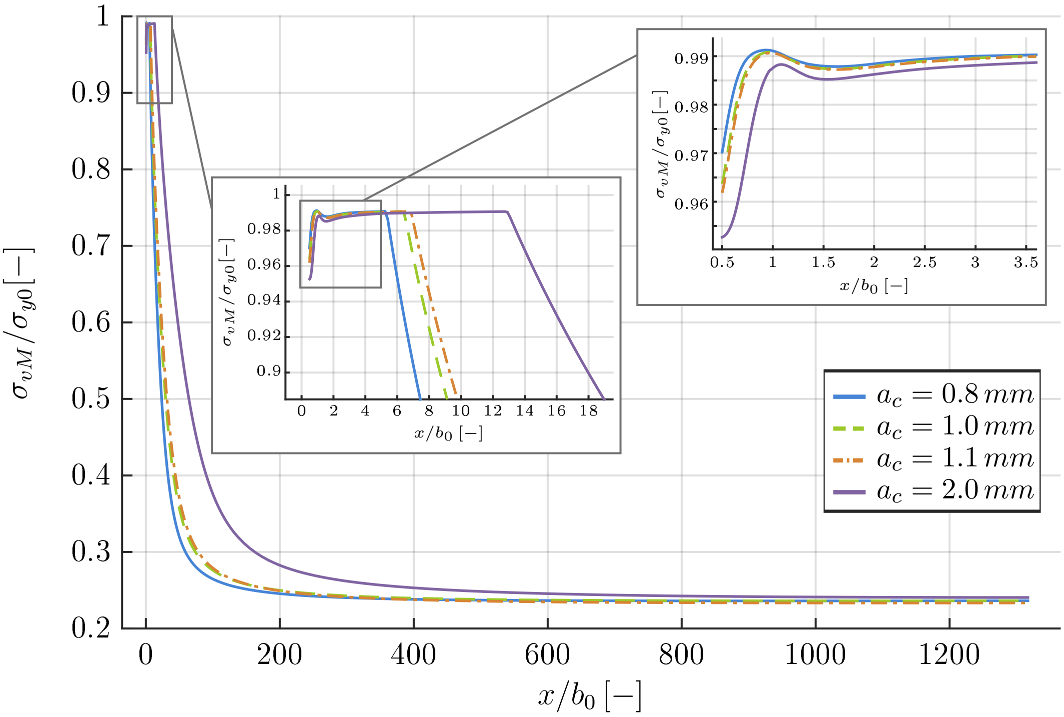

Figure 6.9.: Von Mises stress σ_{vM}, normalized by the initial yield stress σ_{y0}, plotted over the distance to the crack tip for varying crack lengths using the softening approach S2 with $\zeta = 20000$ at steady state condition

by the yield stress σ_{y0} is plotted over the symmetry plane in Figure 6.9, relating to the amount of reduction of the yield stress.

When comparing the curves for the different crack lengths, generally the same trend is noticed. A maximum reduction of the yield stress is identified at the crack tip due to the localized peak of the trapped hydrogen concentration C_T, followed by increasing stress levels when reaching further into the material. Again, a second localized decrease of the yield stress is spotted at the position of the comparatively smaller minimum of the lattice hydrogen concentration C_L (compare Figure 6.9 with general trends of Figure 6.8).

With increasing crack length a_c, the stress at the crack tip rises since the total load level is carried by a reduced pipeline wall cross-section. As a consequence, also the plastic material processes increase in front of the crack tip which can be clearly noticed by the widening of the plastic zone size in Figure 6.9. Here, the border of the plastic zone corresponds to the end of the distinctive plateau. According to these higher stress and strain states in front of the crack tip, also the hydrogen concentration increases. This additionally accumulated hydrogen further reduces the yield stress with increasing crack length.

As noticed in Figure 6.9, the yield stress of the whole plastic zone is reduced for all crack lengths. Since the plastic zone size increases with increasing crack length, also the size of the area generally influenced by hydrogen increases. Therefore, the impact of the reduction of yield stress and thus the local softening gets more pronounced. According to the HELP mechanism, this increased local softening of the material leads to a sudden failure and to the macroscopically observed brittle crack propagation.

The increasing amount of hydrogen embrittlement and the observed increase of the affected zone size with increasing crack length involve an alarming observation. As a consequence of crack propagation, the increased loading state in front of the crack will be altered by a further reduced material resistance in the presence of hydrogen. Thus, the crack can propagate through the pipeline wall rather rapidly which shows that the effect of hydrogen needs to be carefully investigated. However, simulating brittle crack propagation exceeds the scope of this study as the aim of using the applied continuum approach is to qualitatively characterize the changes of the material properties in the presence of hydrogen. Furthermore, the definition of an appropriate softening parameter ζ for the applied X70 pipeline steel shall be the topic of a further investigation.

All in all, it can be concluded that the hydrogen effect on the material properties gets more pronounced with increasing crack length. Especially in the case of localized pre-existing defects, these findings underline the fundamental importance of adequately accounting for hydrogen embrittlement in numerical models for design and inspection of natural gas pipelines.

7. Conclusion and Outlook

Within this thesis, the effect of hydrogen on a representative member of the natural gas pipeline was investigated. In a first step, the conditions of the natural gas pipeline system were described and a pipeline which is damaged during its service time was identified to be critical in case hydrogen is ducted through. Due to the stress localization at defects and cracks, hydrogen showed to accumulate at these locations and can cause a brittle collapse of the respective pipeline segments. Therefore, a pipeline with a pre-existing radial crack was investigated within this thesis.

In literature, several mechanisms are proposed to describe the mechanics of hydrogen embrittlement- the HEDE, the AIDE and the HELP mechanism. It is commonly agreed that all three mechanisms act simultaneously while one dominates. Based on experimental findings, the Hydrogen Enhanced Localized Plasticity (HELP) mechanism was identified to be dominant in the prevalent case. This mechanism assumes that brittle crack propagation is caused by a highly localized softening effect in front of the crack tip. This microscale material softening appears as brittle crack propagation on macroscale. In this thesis, this embrittlement mechanism was numerically realized in a continuum sense by reducing the yield stress in dependency of the hydrogen concentration.

To simulate hydrogen embrittlement, a coupled problem of a transient stress driven hydrogen diffusion equation considering trapping effects and an elasto-plastic material model needs to be solved iteratively. First, the mechanical stress and strain fields were calculated using an elasto-plastic finite element approach. With these results, the transient hydrogen distribution was determined based on a coupled finite element approach in space and time using the time discontinuous Galerkin method. Following the idea of the HELP mechanism, the hydrogen concentration itself in turn influences the mechanical stress field by reducing the yield stress.

As stated above, the effect of the numerical realization of the HELP mechanism on the material properties was investigated at the example of a radially cracked pipeline. Instead of simulating the three dimensional pipeline structure, plane strain conditions were assumed and a two dimensional pipeline model, called full-field model (FFM), was derived. Since the investigation of an adequately meshed pipeline tube is numerically expensive, a surrogate model (SUM) was investigated under small scale yielding conditions using a boundary layer approach. It could be shown that the stress and strain fields as well as the determined hydrogen distributions of the SUM agreed well with the respective solutions of the FFM. Nevertheless, the FFM was needed to specify the boundary conditions of the SUM. Still, these purely elastic calculations of the mechanical stress field showed to be far less expensive than a full elasto-plastic analysis including the effect of hydrogen on the large pipeline structure (FFM).

In a first step, the hydrogen distribution in front of the crack tip was investigated without considering an effect on the material properties. It could be demonstrated that the hydrogen accumulates in the vicinity of the crack tip, especially at hydrostatic stress peaks as well as regions under plastic straining.

Then, once the precise coupling of the mechanical properties and the hydrogen distribution was discussed, the influence of hydrogen on the material properties was investigated. Therefore, three softening approaches were considered, accounting for a yield stress reduction which agrees with the HELP mechanism.

For the first softening approach S1, in fact no reduction of the yield stress could be determined. This result contradicts experimental findings and thus the softening approach S1 was discarded.

The second approach S2 includes a material dependent factor which scales the amount of yield stress reduction. Since this parameter could not be determined on the basis of available experimental data, it was chosen based on preceding studies in literature. By doing so, the coherences of how hydrogen influences the material properties could be demonstrated and discussed.

Softening approach S3 describes the hydrogen induced softening by relating the numerically determined hydrogen concentration to a reference hydrogen concentration. This is a more depictive way of formulating the softening approach, especially when interpreting the reference hydrogen concentration as the critical value at which hydrogen starts to embrittle the material. The main disadvantage of this approach is that using this reference hydrogen concentration creates an additional factor which has to be derived, both in fundamental mechanical meaning and concrete quantitative value.

Based on these findings, in a next step, softening approach S2 was used to determine the influence of the crack length on hydrogen embrittlement. With increasing crack length, the loading level in front of the crack tip increases. Since the hydrogen concentration is driven by the local stress and strain field, consequently the hydrogen concentration in front of the crack trip rises and the yield stress is decreased even further.

All in all, it can be concluded that hydrogen indeed negatively affects the material properties of pipeline steel. It could be shown that with increasing crack lengths, the effect gets more and more pronounced. It has to be assumed that the majority of currently installed pipelines contain numerous localized pre-existing defects. As shown in this thesis, even if the defects show to be noncritical in a purely mechanical sense, the exposure of the pipelines to hydrogen gas could invoke local embrittlement processes leading to crack propagation and ultimately structural failure. Therefore, the pronounced hydrogen embrittlement effect has to be implemented in numerical models used for design and inspection of natural gas pipelines.

While in this thesis the hydrogen movement, accumulation as well as its effect on the material properties could be demonstrated, at the same time several directions for further research could be identified.

Firstly, as described above, the HELP mechanism was assumed as a basis for the investigation of a representative pipeline structure where hydrogen was assumed to solely influence the yield stress. In a further study, also straining effects of the induced hydrogen atoms on the host lattice could be considered. Furthermore, an ideal plastic material law was used to prevent overestimation of the stress state at the crack tip due to linear hardening effects. Consequently, a non-linear hardening rule, including global softening effects, could be included to improve the simulation precision of the material behaviour.

However, in order to be able to finally judge if the natural gas in the existing pipeline system could be completely exchanged with hydrogen gas, a further material characterization seems mandatory. Therefore, when applying softening approach S2, the material dependent continuum parameter ζ, governing the amount of softening, needs to be specified. However, the quantitative determination of this factor appears rather difficult since the local plastic deformations in front of a crack tip as well as the local hydrogen distribution cannot be experimentally determined yet. Thus, the amount of hydrogen induced softening, here the parameter ζ, cannot be characterized.

The effect of hydrogen embrittlement is broadly investigated at uniaxial tensile tests. As a consequence, a tensile test could be used to numerically determine the softening parameter ζ. The tensile experiments showed that hydrogen affects the macroscopical material properties after reaching the ultimate tensile stress. While necking, the formation of surface cracks could be observed solely in the presence of hydrogen and thus a highly localized effect of hydrogen is concluded. However, in continuum mechanics, the formation of localized surface cracks cannot be straight forwardly included in numerical simulations. A fitted factor of ζ from continuum mechanical simulations would denote a macroscopically derived parameter and would not reflect the localization effects of the surface crack formation. As a consequence, the applicability of such a factor on the behaviour of a crack tip in the presence of hydrogen needs to be further investigated. For this, the derivation of appropriate testing techniques to determine the softening parameter ζ could prove promising in the future to lay the basis for precise quantitative prediction of the embritteling effect of hydrogen on pipeline material.

A. Appendix

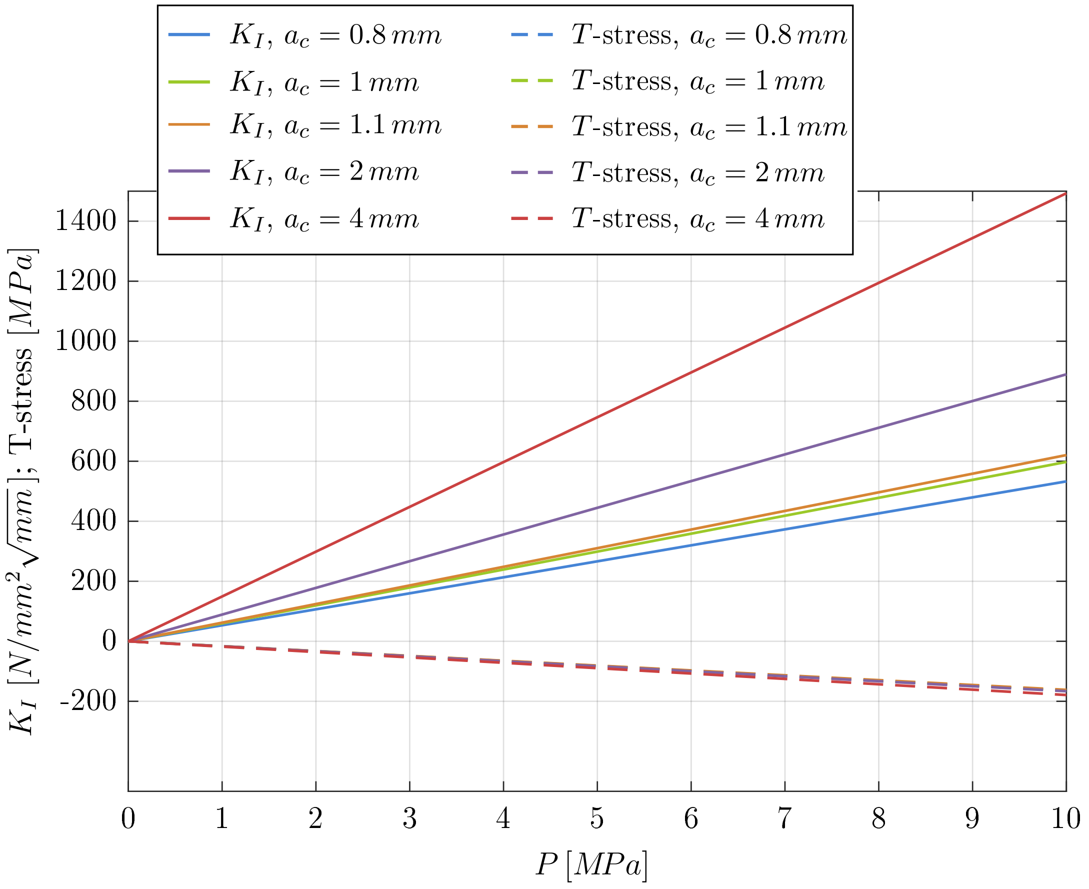

Figure A.1.: Relation of pressure P to the stress intensity factor K_I and the T-stress for various crack lengths a_c

Table A.1.: Chemical composition of low carbon steels discussed in chapter 3

Steel	**C [wt%]**	**Mn [wt%]**	**P [wt%]**	**S [wt%]**	**Si [wt%]**	**Ni [wt%]**	**Cu [wt%]**	**N [wt%]**	**Cr [wt%]**	**V [wt%]**	**Others [wt%]**	**Reference**
S235JR	max 0.17	1.4	max. 0.0045	max. 0.0045	max 0.45						N= 0.012	[57]
S235JR	0.134	0.43	0.013	0.009	0.01	0.03	0.056		0.04		Al=0.0023	[50]
X52	0.06	0.87	0.011	0.006	0.12	0.02			0.03		Nb+V+Ti =0.03	[51]
X65	0.08	1.56	0.011	0.003	0.325	0.21			0.03		Mo=0.006; Nb+V+Ti =0.09	
X100	0.064	1.87	0.009	<0.001	0.099	0.47			0.23		Mo=0.23; Nb+V+Ti =0.036	
X80	0.075	1.86	0.015	<0.003	0.35						Nb=0.05; V<0.01; Cu=0.22	[52]
St.20	0.24	0.48	0.013	0.025	0.28						-	[67]
X60 HIC	0.03	1.14	0.008	0.001	0.18	0.14	0.24		0.16	0.001	Nb=0.084; Al=0.034; Ti=0.014	[53]
X80	0.05	1.52	0.007	0.003	0.12	0.14	0.23	-	0.25	0.001	Nb=0.092; Al=0.036; Ti=0.012	

Table A.2.: Chemical composition of low carbon steels discussed in chapter 3

Steel	C [wt%]	Mn [wt%]	P [wt%]	S [wt%]	Si [wt%]	Ni [wt%]	Cu [wt%]	N [wt%]	Cr [wt%]	V [wt%]	Others [wt%]	Reference
A516-USA	0.21	1.04	0.012	0.02	0.21							[49]
A516-JAP	0.26	0.79	0.013	0.033	0.17							
A106-B	<.3	0.3-1.06	-	-	>0.1							
A14	0.11	1.44	0.013	0.002	0.27					0.09	Cb=0.04; Al=0.037; Cu=0.29; Ni=0.29	
BF 5	0.22	1.23	-	-	0.11						Cb=0.02	
DG 2	0.14	0.98	0.015	0.012	0.29						Cb<0.01; Al<0.012	
AG3	0.26	1.39	0.006	0.022	0.03						V=0.05	
X60	0.1-0.15	1.4-2.0	0.01-0.02	<0.003	0.2-0.5						Al=0.03-0.05	[56]
X80												
X100												

Symbols

Mechanical model

a	scalar isotropic hardening parameter
a_c	crack length
b_0	crack tip opening displacement
B	body of current configuration
B_0	body of reference configuration
$\boldsymbol{b}$	kinematic hardening tensor
$\boldsymbol{b_f}$	body forces
$\boldsymbol{c}$	left Cauchy-Green tensor
$\boldsymbol{C}$	right Cauchy-Green tensor
$\mathbb{C}^e$	elastic material tangent
$\mathbb{C}^{ep}$	elasto-plastic material tangent
d	diameter of pipeline
da	cutting plane in the current configuration
dA	cutting plane in the reference configuration
D_{in}	inner dissipation
E	Young's modulus
$\boldsymbol{e}$	Euler-Almansi strain tensor
$\boldsymbol{E}$	Green-Lagrange strain tensor
f	flow rule
$d\boldsymbol{f}$	agent force
F	force
$\boldsymbol{F}$	deformation gradient
G	shear modulus
H_{iso}	scalar material parameter accounting for the amount of isotropic hardening
H_{kin}	scalar material parameter accounting for the amount of kinematic hardening
$\boldsymbol{I}$	identity matrix
$\mathbb{I}$	fourth order identity tensor
J	Jacobian matrix
K	stress intensity factor
$\boldsymbol{K}$	stiffness matrix
K_I	stress intensity factor with mode I opening condition
$K_{I,a}$	analytical determined stress intensity factor (mode I opening condition)
$K_{I,n}$	numerical determined stress intensity factor (mode I opening condition)
$K_{I,C}$	critical stress intensity factor (mode I opening condition)
L_{FFM}	length of uncracked region of the full-field model
L_{SUM}	length of uncracked region of the surrogate model
m	mass
m_s	number of spatial nodes
m_t	number of nodes in time

$\boldsymbol{M}$	mass matrix
$\boldsymbol{n}$	normal tensor
$\boldsymbol{N}$	normal tensor
$\widetilde{N}$	shape function in time
N	spatial shape function
p	hydrostatic stress
P	pressure
P_m	material point
$\boldsymbol{P}$	first Piola-Kirchhoff tensor
r_p	radius of plastic zone
r_{in}	inner radius
r_{out}	outer radius
$\boldsymbol{R}$	rotation tensor
$\boldsymbol{S}$	second Piola-Kirchhoff tensor
S_0	cross section of uniaxial tensile specimen
t	time
$\boldsymbol{t}$	stress vector in the current configuration
$\boldsymbol{T}$	stress vector in the reference configuration
T	T-stress
$\boldsymbol{u}$	displacement vector
$\boldsymbol{U}$	stretch tensor
$\boldsymbol{v}$	velocity of a material point
$\boldsymbol{V}$	stretch tensor
w	wall thickness
w_p	width of plate
$\boldsymbol{x}$	position vector of a material point in the current configuration
$\boldsymbol{X}$	position vector of a material point in the reference configuration
Z	substitutive function

α	scalar isotropic hardening parameter
$\boldsymbol{\beta}$	kinematic hardening tensor
$\Delta l_u(H_2)$	critical elongation
$\boldsymbol{\varepsilon}$	strain tensor
$\boldsymbol{\varepsilon}_e$	elastic part of strain tensor
$\boldsymbol{\varepsilon}_p$	plastic part of strain tensor
$\bar{\varepsilon}^p$	equivalent plastic strain
$\boldsymbol{\varepsilon}_H$	strain due to hydrogen
ζ	material dependent softening parameter
η	test function in time and space
κ	bulk modulus
λ	Lagrange multiplier
μ	Lamé constant
ν	Poisson's ratio
ξ	material dependent softening parameter
ρ	mass density
σ_u	ultimate tensile stress
σ_{uH}	ultimate tensile stress in presence of hydrogen
σ_{vM}	von Mises stress
σ_{y0}	yield stress
$\boldsymbol{\sigma}$	Cauchy stress tensor

$\boldsymbol{\tau}$	Kirchhoff stress tensor
ψ	free energy function
ψ_e	elastic part of the free energy function
ψ_p	plastic part of the free energy function
Ω	space domain

Hydrogen transport model

b_0	crack tip opening displacement
c	scaling parameter reflecting the occupancy of available lattice sites
$c_{T,r}$	scaling parameter
C_L	lattice hydrogen concentration
$C_{L,0}$	surface lattice hydrogen concentration
C_T	trapped hydrogen concentration
C_r	reference concentration
D	lattice diffusion coefficient
D_{eff}	effective diffusion parameter
f	fugacity
k	solubility
k_0	solubility pre-exponential factor
L_{FFM}	length of uncracked region of the full-field model
L_{SUM}	length of uncracked region of the surrogate model
m_s	number of spatial nodes
m_t	number of nodes in time
$\widetilde{N}$	shape function in time
N	spatial shape function
N_A	Avogadro's number
N_L	number of solvent atoms per unit volume
N_T	trap density
R	universal gas constant
t_n	time step
T	temperature
$\boldsymbol{T_a}$	time matrix
$\boldsymbol{T_b}$	time matrix
$\boldsymbol{T_c}$	time matrix
V_H	partial molar volume of hydrogen
V_M	molar volume of the host lattice
W_B	trap binding energy
z_1	constant
z_2	constant

α	number of available sites per trap where hydrogen can be bound
β	number of normal interstitial lattice sites per host atom
ΔH_S	enthalpy of solution
η	test function in time and space
θ_L	occupancy of available lattice sites
θ_T	occupancy of available trapping sites
τ_n	time domain

Acronyms

AIDE	Adsorption Induced Dislocation Emission
DOF	degrees of freedom
FEM	finite element method
FFM	full-field model
HEDE	Hydrogen Enhanced Decohesion
HELP	Hydrogen Enhanced Localized Plasticity
RA	reduction of fracture area
SUM	surrogate model
TDG	time discontinous Galerkin
UTS	ultimate tensile strength

Bibliography

[1] D. Haeseldonckx and W. D'haeseleer. The use of the natural-gas infrastructure for hydrogen transport in a changing market structure. *International Journal of Hydrogen Energy*, 32:1381–1386, 2007.

[2] V. Olden, A. Alvaro, and O.M. Akselsen. Hydrogen diffusion and hydrogen influenced critical stress intensity in an API X70 pipeline steel welded joint – experiments and FE simulations. *International Journal of Hydrogen Energy*, 37(15):11474 – 11486, 2012. Hydrogen Enriched Methane.

[3] Eurogas. Länge der Erdgas-Pipelines in ausgewählten Ländern Europas im Jahr 2014 (in Kilometer). Statista - Das Statistik-Portal, Statista, https://de.statista.com/statistik/daten/studie/175484/umfrage/laenge-der-pipelines-fuer-erdgas-in-europaeischen-laendern/, 2017. Online; 20. Dezember 2017.

[4] William H. Johnson. On some remarkable changes produced in iron and steel by the action of hydrogen and acids. *Proceedings of the Royal Society of London*, 23:168–179, 1874.

[5] W. Gerberich. Modeling hydrogen induced damage mechanisms in metals. In R.P. Gangloff and B.P. Somerday, editors, *Gaseous Hydrogen Embrittlement of Materials in Energy Technologies, Volume 2: Mechanisms, modelling and future developments*, pages 209–246. Woodhead Publishing Limited, 2012.

[6] C.A. Zapffe and C.E. Sims. Hydrogen embrittlement, internal stress and defects in steel. *Trans. Amer. Inst. Mining Met. Engrs., Iron Steel Div.*, 145:47, 1941.

[7] M. Wen, L. Zhang, B. An, S. Fukuyama, and K. Yokogawa. Hydrogen-enhanced dislocation activity and vacancy formation during nanoindentation of nickel. *Phys. Rev. B*, 80:094113, 2009.

[8] K.A. Nibur, D.F. Bahr, and B.P. Somerday. Hydrogen effects on dislocation activity in austentic stainless steel. *Acta Material*, 54:2677–2684, 2006.

[9] J. Song and W.A. Curtin. A nanoscale mechanism of hydrogen embrittlement in metals. *Acta Materialia*, 59:1557–1569, 2011.

[10] G. Gobbi, C. Colombo, S. Miccoli, and L. Vergani. A numerical model to study the hydrogen embrittlement effect. *Procedia Engineering*, 74(0):460–463, 2014. {XVII} International Colloquium on Mechanical Fatigue of Metals (ICMFM17).

[11] S. Serebrinsky, E.A. Carter, and M. Ortiz. A quantum-mechanically informed continuum model of hydrogen embrittlement. *Journal of the Mechanics and Physics of Solids*, 52:2403–2430, 2004.

[12] W. Bouajila, J. Riccius, and M. Bruchhausen. Simulation of the high cycle fatigue life reduction due to internal hydrogen embrittlement using a commercial finite element program. *AIAA 51th Aerospace Sciences Meeting*, 2013.

[13] H. Kotake, R. Matsumoto, S. Taketomi, and N. Miyazaki. Transient hydrogen diffusion analyses coupled with crack-tip plasticity under cyclic loading. *International Journal of Pressure Vessels and Piping*, 85(8):540–549, 2008.

[14] H. Kitagawa and Y. Kojima. Diffusion of hydrogen near an elasto-plastically deformed crack tip. In R. M. Latanision and J. R. Pickens, editors, *Atomistics of Fracture*, pages 799–811. Springer US, Boston, MA, 1983.

[15] P. Sofronis and R.M. McMeeking. Numerical analysis of hydrogen transport near a blunting crack tip. *Journal of the Mechanics and Physics of Solids*, 37(3):317–350, 1989.

[16] A.H.M. Krom, R.W.J. Koers, and A. Bakker. Hydrogen transport near a blunting crack tip. *Journal of the Mechanics and Physics of Solids*, 47(4):971 – 992, 1999.

[17] E. Martínez-Pañeda, S. del Busto, C.F. Niordson, and C. Betegón. Strain gradient plasticity modeling of hydrogen diffusion to the crack tip. *International Journal of Hydrogen Energy*, 41(24):10265 – 10274, 2016.

[18] J. Lufrano and P. Sofronis. Enhanced hydrogen concentrations ahead of rounded notches and cracks—competition between plastic strain and hydrostatic stress. *Acta Materialia*, 46(5):1519 – 1526, 1998.

[19] H. Peisl. Lattice strains due to hydrogen in metals. In *Hydrogen in metals I*, pages 53–74. Springer, 1978.

[20] Y. Liang and P. Sofronis. Micromechanics and numerical modeling of the hydrogen–particle–matrix interactions in nickel-base alloys. *Modelling and Simulation in Materials Science and Engineering*, 11(4):523, 2003.

[21] M. Dadfarnia, B.P. Somerday, P. Sofronis, I.M. Robertson, and D. Stalheim. Interaction of hydrogen transport and material elastoplasticity in pipeline steels. *J. Pressure Vessel Technol.*, 131(4):041404–1 –041404–13, 2009.

[22] Y. Liang, P. Sofronis, and R.H. Dodds Jr. Interaction of hydrogen with crack-tip plasticity: effects of constraint on void growth. *Materials Science and Engineering: A*, 366(2):397–411, 2004.

[23] M. Dadfarnia, P. Sofronis, B.P. Somerday, and I.M. Robertson. Hydrogen/plasticity interactions at an axial crack in pipeline steel. *Journal of ASTM International*, 5(6):1–16, 2008.

[24] M. Dadfarnia, P. Sofronis, B.P. Somerday, and I.M. Robertson. Effect of remote hydrogen boundary conditions on the near crack-tip hydrogen concentration profiles in a cracked pipeline: Fracture toughness assessment. *Ceramic Transactions*, 202:187–199, 2009. cited By 3.

[25] K. Takayama, R. Matsumoto, S. Taketomi, and N. Miyazaki. Hydrogen diffusion analyses of a cracked steel pipe under internal pressure. *International Journal of Hydrogen Energy*, 36(1):1037–1045, 2011.

[26] M. Dadfarnia, P. Sofronis, B.P. Somerday, and I.M Robertson. On the small scale character of the stress and hydrogen concentration fields at the tip of an axial crack in steel pipeline: effect of hydrogen-induced softening on void growth. *International Journal of Materials Research*, 99:557–570, 2008.

[27] E.A. de Souza Neto, D. Peric, and D.R.J. Owen. *Computational Methods for Plasticity: Theory and Applications.* John Wiley and Sons, Ltd, 2008.

[28] G.A. Holzapfel. *Nonlinear Solid Mechanics: A Continuum Approach for Engineering.* John Wiley and Sons, LTD, 2000.

[29] K. Fietz. *Towards a Finite Element Model for Fluid Flow in the Human Hip Joint.* PhD thesis, Leibniz Universität Hannover, 2013.

[30] R. Hill. A theory of the yielding and plastic flow of anisotropic metals. *Proceedings of the Royal Society of London A: Mathematical, Physical and Engineering Sciences*, 193(1033):281–297, 1948.

[31] W. Bergmann. *Werkstofftechnik, Teil 1: Grundlagen.* Carl Hanser Verlag München. 6. aktualisierte Auflage, 2008.

[32] H.L. Ewalds and R.J.H. Wanhill. *Fracture Mechanics.* Edward Arnold Ltd and Delftse Uitgevers Maatschaooij, 1986.

[33] D. Gross and T. Seelig. *Bruchmechanik: mit einer Einführung in die Mikromechanik.* Springer-Verlag, 5. erweiterte Auflage edition, 2016.

[34] M. Gupta, R.C. Alderliesten, and R. Benedictus. A review of T-stress and its effects in fracture mechanics. *Engineering Fracture Mechanics*, 134(Supplement C):218 – 241, 2015.

[35] G.R. Irwin. Fracture. In S. Flügge, editor, *Elasticity and Plasticity / Elastizität und Plastizität*, pages 551–590. Springer Berlin Heidelberg, Berlin, Heidelberg, 1958.

[36] H. Westergaard. Bearing pressure and cracks. *J. Applied Mech.*, 6:A49–53, 1939.

[37] M.L. Williams. Stress distribution at the base of a stationary crack. *J. appl. Mech.*, 79:109–114, 1957.

[38] Q. Han, Y. Wang, Y. Yin, and D. Wang. Determination of stress intensity factor for mode i fatigue crack based on finite element analysis. *Engineering Fracture Mechanics*, 138(Supplement C):118 – 126, 2015.

[39] J. Bjornmose, F. Roca, T. Turgot, and D.S. Hansen. An assessment of the gas and oil pipelines in europe; an extensive briefing note. In *Policy Department, economic and Scientific Policy A*. European Parliament, Brüssel, 2009.

[40] FNB Gas. Gas transmission. http://www.fnb-gas.de/en/transmission-systems/gas-transmission/gas-transmission.html, 2017. Online; accessed 11 May 2017.

[41] Salzgitter Mannesmann Großrohr GmbH. Referenzliste - Ausgewählte Projekte seit 2000. http://www.smgr.com/de/download/referenzliste.html, 2017. Online; accessed 11 May 2017.

[42] F. Grimpe, S. Meimeth, H. Meuser, and A. Liessem. Entwicklung, Produktion und Anwendung thermomechanisch gewalzter hoch- und ultrahochfester Grobbleche. *STAHL*, 4, 2007.

[43] Enercity Netzgesellschaft mbH. Netzgebiet für die Gasversorgung. https://www.enercity-netz.de/netze/gas/netzgebiet/index.html, 2016. Online; accessed 11 May 2017.

[44] Enercity Netzgesellschaft mbH. Zahlen und Fakten zum Gasnetz der Grundversorger. https://www.enercity-netz.de/netze/gas/zahlen-fakten/index.html, 2016. Online; accessed 11 May 2017.

[45] M. Veenker. Klassifizierung und Bewertung von Anlagenteilen aus statischer und sicherheitstechnischer Sicht. In K. Hesselbarth, editor, *Gaskochdruckleitung, Sicherheit und Qualität*, volume 23 of *Schriftenreihe aus dem Institut für Rohrleitungsbau Oldenburg*, pages 236–238. Essen : Vulkan-Verl., 2001.

[46] R.A. Oriani. The diffusion and trapping of hydrogen in steel. *Acta Metallurgica*, 18(1):147–157, 1970.

[47] P.S. Lam, R.L. Sindelar, A.J. Duncan, and T.M. Adams. Literature survey of gaseous hydrogen effects on the mechanical properties of carbon and low alloy steels. *Journal of pressure vessel technology*, 131(4), 2009.

[48] B.P. Somerday. Technical reference on hydrogen compatibility of materials, plain carbon ferritic steels: C - mn alloys (code 1100). Technical report, Sandia National Laboratories, Livermore CA, 2012.

[49] W.R. Hoover, J.J. Iannucci, S.L. Robinson, J.R. Spingarn, and R.E. Stoltz. Hydrogen compatibility of structural materials for energy storage and transmission. *NASA STI/Recon Technical Report N*, 81, May 1981.

[50] E. Merson, A. Vinogradov, and D.L. Merson. Application of acoustic emission method for investigation of hydrogen embrittlement mechanism in the low-carbon steel. *Journal of Alloys and Compounds*, 645, Supplement 1:S460–S463, 2015. Supplement Issue: Proceedings from the 14th International Symposium on Metal-Hydrogen Systems: Fundamentals and Applications, 2014 (MH2014).

[51] N.E. Nanninga, Y.S. Levy, E.S. Drexler, R.T. Condon, A.E. Stevenson, and A.J. Slifka. Comparison of hydrogen embrittlement in three pipeline steels in high pressure gaseous hydrogen environments. *Corrosion Science*, 59:1–9, 2012.

[52] I. Moro, L. Briottet, P. Lemoine, E. Andrieu, C. Blanc, and G. Odemer. Hydrogen embrittlement susceptibility of a high strength steel X80. *Materials Science and Engineering: A*, 527(27–28):7252–7260, 2010.

[53] M.L. Martin, I.M. Robertson, and P. Sofronis. Interpreting hydrogen-induced fracture surfaces in terms of deformation processes: A new approach. *Acta Materialia*, 59:3680–3687, 2011.

[54] D.J. Christenson, I.M. Berstein, A.W. Thompson, E.J. Danielson, M. Elices, and F. Gutierrez-Solana. Hydrogen compatibility of a line pipe steel. *Hydrogen Effects in Metals*, pages 997–1004, 1980.

[55] K. XU. Hydrogen embrittlement of carbon steels and their welds. In R.P. Gangloff and B.P. Somerday, editors, *Gaseous Hydrogen Embrittlement of Materials in Energy Technologies, Volume 1: The problem, its characterisation and effects on particular alloy classes*, pages 526–561. Woodhead Publishing Limited, 2012.

[56] D. Hardie, E.A. Charles, and A.H. Lopez. Hydrogen embrittlement of high strength pipeline steels. *Corrosion Science*, 48(12):4378–4385, 2006.

[57] C.S. Parfene, G. Solomon, and C. Babis. The effect of diffusible hydrogen in weld seams on the mechanical and corrosion behaviour of S235JR steel parts in 3.5% NaCl. *Rev. Chim.*, 65(6), 2014.

[58] I.M. Robertson, P. Sofronis, A. Nagao, M.L. Martin, S. Wang, D.W. Gross, and K.E. Nygren. Hydrogen embrittlement understood. *Metallurgical and Materials Transactions B*, 46(3):1085–1103, 2015.

[59] I.M. Robertson, M.L. Martin, and J.A. Fenske. Influence of hydrogen on the behavior of dislocations. In R.P. Gangloff and B.P. Somerday, editors, *Gaseous Hydrogen Embrittlement of Materials in Energy Technologies, Volume 2: Mechanisms, modelling and future developments*, pages 166–206. Woodhead Publishing Limited, 2012.

[60] L.P. Mikkelsen and S. Goutianos. Suppressed plastic deformation at blunt crack-tips due to strain gradient effects. *International Journal of Solids and Structures*, 46(25):4430–4436, 2009.

[61] S.P. Lynch. Methallographic and fractographic techniques for characterising and unterstanding hydrogen-assisted cracking of metals. In R.P. Gangloff and B.P. Somerday, editors, *Gaseous Hydrogen Embrittlement of Materials in Energy Technologies, Volume 1: The problem, its characterisation and effects on particular alloy classes*, pages 274–346. Commonwealth of Australia, 2012.

[62] D.F. Teter, I.M. Robertson, and H.K. Birnbaum. The effects of hydrogen on the deformation and fracture of beta titanium. *Acta Mater.*, 49:4313–4323, 2001.

[63] I.M. Robertson and D. Teter. Controlled environment transmission electron microscopy. *J. Microsc. Res. Tech.*, 42:260, 1998.

[64] S.P. Lynch. Hydrogen embrittlement phenomena and mechanisms. *Corrosion Reviews*, 30:105–123, 2012.

[65] A. Barnoush. *Hydrogen embrittlement, revisited by in situ electrochemical nanoindentation.* PhD thesis, Universität des Saarlandes, 2007.

[66] J.P. Hirth. Effects of hydrogen on the properties of iron and steel. *Metallurgical Transactions A*, 11(6):861–890, 1980.

[67] M.B. Djukic, V. Sijacki Zeravcic, G. Bakic, A. Sedmak, and B. Rajicic. Hydrogen embrittlement of low carbon structural steel. *Procedia Materials Science*, 3(0):1167–1172, 2014. 20th European Conference on Fracture.

[68] J.K. Tien, S.V. Nair, and R.R. Jensen. Dislocation sweeping of hydrogen and hydrogen embrittlement. *Hydrogen effects in metals, Metallurgian Society of AIME*, pages 38–56, 1981.

[69] J. Tien, A.W. Thompson., I.M. Bernstein, and R.J. Richards. Hydrogen transport by dislocations. *Metallurgical Transactions A*, 7(6):821–829, 1976.

[70] S.P. Lynch. Interpreting hydrogen-induced fracture surfaces in terms of deformation processes: A new approach. *Procedia Materials Science 3*, 65:851–854, 2011.

[71] Y. Takahashi, H. Nishikawa, Y. Oda, and H. Noguchi. Microscopic characterization of hydrogen-induced quasi-brittle fatigue fracture in low-strength carbon steel. *Materials Letters*, 64(22):2416–2419, 2010.

[72] Y. Takahashi, M. Tanaka, K. Higashida, and H. Noguchi. Hydrogen-induced slip localization around a quasi-brittle fatigue crack observed by high-voltage electron microscopy. *Scripta Materialia*, 61(2):145–148, 2009.

[73] Y. Takahashi, M. Tanaka, K. Higashida, K. Yamaguchi, and H. Noguchi. An intrinsic effect of hydrogen on cyclic slip deformation around a 110 fatigue crack in fe–3.2wt. *Acta Materialia*, 58(6):1972–1981, 2010.

[74] J.P. Chateau, D. Delafosse, and T. Magnin. Numerical simulations of hydrogen-dislocation interactions in fcc stainless steels. part i: hydrogen-dislocation interactions in bulk crystals. *Acta Materialia*, 2001.

[75] A. Taha and P. Sofronis. A micromechanics approach to the study of hydrogen transport and embrittlement. *Engineering Fracture Mechanics*, 68(6):803 – 837, 2001.

[76] A.J. Kumnick and H.H. Johnson. Deep trapping states for hydrogen in deformed iron. *Acta Metallurgica*, 28(1):33–39, 1980.

[77] T. Tabata and H.K. Birnbaum. Direct observations of the effect of hydrogen on the behavior of dislocations in iron. *Scripta Metallurgica*, 17(7):947 – 950, 1983.

[78] P. Sofronis, Y. Liang, and N. Aravas. Hydrogen induced shear localization of the plastic flow in metals and alloys. *European Journal of Mechanics, A-Solids*, 20(6):857–872, 11 2001.

[79] I.M. Robertson. The effect of hydrogen on dislocation dynamics. *Engineering Fracture Mechanics*, 68(6):671 – 692, 2001.

[80] T.J.R. Hughes and G.M. Hulbert. Space-time finite element methods for elastodynamics: Formulations and error estimates. *Computer Methods in Applied Mechanics and Engineering*, 66(3):339 – 363, 1988.

[81] A. Sapotnick. *On a Finite Element Approach for the Solution of a mechanically Stimulated Biochemical Fracture Healing Model.* dissertation, Institute of Mechanics and Computational Mechanics, Leibniz Universität Hannover, 2015.

[82] W.H. Reed and T.R. Hill. Triangular mesh methods for the neutron transport equation. *Los Almo Report*, LA-UR-73-479, 1973.

[83] P. Lesaint and P.A. Raviart. On a finite element method for solving the neutron transport equation. *Publications mathématiques et informatique de Rennes*, pages 1–40, 1974.

[84] M. Ziefle. *Numerische Konzepte zur Behandlung inelastischer Effekte beim reibungsbehafteten Rollkontakt.* dissertation, Institute of Mechanics and Computational Mechanics, Leibniz Universität Hannover, 2007.

[85] D. Feng. *Numerical Modeling of Oral Biofilm Growth Using Finite Element Method.* dissertation, Institute of Fluid Mechanics and Environmental Physics in Civil Engineering, Leibniz Universität Hannover, 2017.

[86] R. Taylor O. Zienkiewicz and J.Zhu. *The finite elemenet method: Its basis and Fundamentals.* Elsevier Ltd., 2005.

[87] P. Wriggers. *Nichtlineare finite element methode.* Springer, 2001.

[88] U. Baek, H. Lee, S. Baek, and S. Nahm. Hydrogen embrittlement for X-70 pipeline steel in high pressure hydrogen gas. *Proceedings of the ASME Pressure Vessels and Piping Conference: Materials and Fabrication*, 6B, 2015.

[89] G.R Irwin. Fracture mechanics. In J.N. Goodier and N.J. Hoff, editors, *Structural Mechanics, Proceedings of the First Symposium of Naval Structural Mechanics*, pages 557–594. Standford University, 1960.

[90] J.R. Rice. Mathematical analysis in the mechanics of fracture. In H. Liebowitz, editor, *Fracture: An Advanced Treatise*, volume 2 of *Mathematical Fundamentals*, pages 191–311. Academic Press, N.Y., 1968.

[91] A. Sieverts and W. Krumbhaar. Über die Löslichkeit von Gasen in Metallen und Legierungen. *Berichte der deutschen chemischen Gesellschaft*, 43:893–900, 1910.

[92] H.H. Johnson. Hydrogen gas embrittlement. In I.M Bernstein and A.W. Thompson, editors, *Hydrogen in metals*, pages 35–49. American Society for Metals (ASM), 1974. Supplement Issue: Proceedings of an international conference on the effects of hydrogen on metarials properties and selection and structural design.

[93] A.H.M. Krom, A. Bakker, and R.W.J. Koers. Modelling hydrogen-induced cracking in steel using a coupled diffusion stress finite element analysis. *International Journal of Pressure Vessels and Piping*, 72(2):139 – 147, 1997.

[94] O. Aslan. Numerical modeling of hydrogen diffusion in metals accounting for large deformations. *International Journal of Hydrogen Energy*, 40(44):15227–15235, 2015. The 4th International Conference on Nuclear and Renewable Energy Resources (NURER2014), 26-29 October 2014, Antalya, Turkey.

[95] M. Möhle, U. Nackenhorst, and O. Allix. Numerical simulation of hydrogen embrittlement at the example of a cracked pipeline. In P. Wriggers J. Soric, O. Allix, editor, *Multiscale Modeling of Heterogeneous Structures, 'Lecture Notes in Applied and Computational Mechanics'. 1st ed.* Springer-Verlag GmbH, 2018.

Curriculum Vitae

Personal Information

Name:	Milena Möhle
Date of Birth:	18.07.1987 in Minden

Education

08 / 1998 – 06 / 2007	Stätisches Gymnasium Porta Westfalica
02 / 2013 – 05 / 2013	Semester abroad at the University of Canberra, Australia
10 / 2008 – 12 / 2013	Studies in civil engineering at the Leibniz Universität Hannover Degree: Diplom-Ingenieur (Dipl.-Ing.)

Professional Life

01 / 2014 – 06 / 2017	Research assistant at the Institute of Mechanics and Computational Mechanics (IBNM), Leibniz Universität Hannover
02 / 2015 – 07 / 2015	Research stay at the ENS Cachan, Paris

Research Reports, IBNM

Institut für Baumechanik und Numerische Mechanik
Gottfried Wilhelm Leibniz Universität Hannover

Published reports:

S 73/1 Seminar über Thermodynamik und Kontinuumsmechanik, Hannover 1973

F 75/1 “Die Spannungsberechnung im Rahmen der Finite–Element–Methode”,
R. Ahmad, Dissertation, April 1975

F 76/1 “Zur Theorie und Anwendung der Stoffgleichungen elastisch–plastisch–viskoser Werkstoffe”,
H. Mentlein, Dissertation, April 1976

S 77/1 Seminar über lineare und geometrisch nichtlineare Schalentheorie einschließlich Stabilitätstheorie, Hannover 1977

F 77/2 “Beitrag zur Berechnung von Gründungsplatten mit Hilfe der Finite–Element–Methode”,
H. Meyer, Dissertation, Juli 1977

F 77/3 “Zur Berechnung der Eigenfrequenzen und Eigenschwingungsformen räumlich vorgekrümmter und vorverwundener Stäbe”,
J. Möhlenkamp, Dissertation, Dezember 1977

F 77/4 “Zur Theorie und Berechnung geometrisch und physikalisch nichtlinearer Kontinua mit Anwendung der Methode der finiten Elemente”,
J. Paulun, Dissertation, Dezember 1977

S 78/1 2. Seminar über Thermodynamik und Kontinuumsmechanik,
Hannover 1978

F 79/1 “Theoretische und numerische Behandlung geometrisch nichtlinearer viskoplastischer Kontinua”,
K.–D. Klee, Dissertation, Februar 1979

F 79/2 “Zur Konstruierbarkeit von Variationsfunktionalen für nichtlineare Probleme der Kontinuumsmechanik”,
J. Siefer, Dissertation, Oktober 1979

F 80/1 “Theoretische und numerische Behandlung gerader Stäbe mit endlichen Drehungen”,
M. Kessel, Dissertation, Februar 1980

F 81/1 “Zur Berechnung von Kontakt– und Stoßproblemen elastischer Körper mit Hilfe der Finite–Element–Methode”,
P. Wriggers, Dissertation, Januar 1981

F 81/2 “Stoffgleichungen für Steinsalze unter mechanischer und thermischer Beanspruchung”,
J. Olschewski, E. Stein, W. Wagner, D. Wetjen, geänderte Fassung eines Zwischenberichtes zum BMFT–Forschungsvorhaben KWA 1608/5

F 82/1 “Konvergenz und Fehlerabschätzung bei der Methode der Finiten Elemente”,
R. Rohrbach, E. Stein, Abschlußbericht eines VW–Forschungsvorhabens, Februar 1982

F 82/2 “Alternative Spannungsberechnung in Finite–Element–Verschiebungsmodellen”,
C. Klöhn, Dissertation, November 1982

F 83/1 Seminar über nichtlineare Stabtheorie, Hannover 1983

F 83/2 “Beiträge zur nichtlinearen Theorie und inkrementellen Finite–Element– Berechnung dünner elastischer Schalen”,
A. Berg, Dissertation, Juli 1983

F 83/3 “Elastoplastische Plattenbiegung bei kleinen Verzerrungen und großen Drehungen”,
J. Paulun, Habilitation, September 1983

F 83/4 “Geometrisch nichtlineare FE–Berechnung von Faltwerken mit plastisch / viskoplastischem Deformationsverhalten”,
M. Krog, Dissertation, Dezember 1983

F 85/1 Verleihung der Ehrendoktorwürde des Fachbereichs Bauingenieur– und Vermessungswesen der Universität Hannover an die Herren Prof. Dr. Drs. h.c. J.H. Argyris, Dr.–Ing. H.Wittmeyer

F 85/2 “Eine geometrisch nichtlineare Theorie schubelastischer Schalen mit Anwendung auf Finite–Element–Berechnungen von Durchschlag– und Kontaktproblemen”,
W. Wagner, Dissertation, März 1985

F 85/3 “Geometrisch/physikalisch nichtlineare Probleme — Struktur und Algorithmen — ”, GAMM–Seminar im Februar 1985 in Hannover

F 87/1 “Finite–Elemente–Berechnungen ebener Stabtragwerke mit Fließgelenken und großen Verschiebungen”,
R.Kahn, Dissertation, Oktober 1987

F 88/1 “Theorie und Numerik schubelastischer Schalen mit endlichen Drehungen unter Verwendung der Biot–Spannungen”,
F. Gruttmann, Dissertation, Juni 1988

F 88/2 “Optimale Formgebung von Stabtragwerken mit Nichtlinearitäten in der Zielfunktion und in den Restriktionen unter Verwendung der Finite-Element-Methode”,
V. Berkhahn, Dissertation, Oktober 1988

F 88/3 “Beiträge zur Theorie und Numerik großer plastischer und kleiner elastischer Deformationen mit Schädigungseinfluß”,
R. Lammering, Dissertation, November 1988

F 88/4 “Konsistente Linearisierungen in der Kontinuumsmechanik und ihrer Anwendung auf die Finite–Elemente–Methode”,
P. Wriggers, Habilitation, November 1988

F 88/5 “Mathematische Formulierung und numerische Methoden für Kontaktprobleme auf der Grundlage von Extremalprinzipien”,
D. Bischoff, Habilitation, Dezember 1988

F 88/6 “Zur numerischen Behandlung thermomechanischer Prozesse”,
C. Miehe, Dissertation, Dezember 1988

F 89/1 “Zur Stabilität und Konvergenz gemischter finiter Elemente in der linearen Elastizitätstheorie”,
R. Rolfes, Dissertation, Juni 1989

F 89/2 “Traglastberechnungen von Faltwerken mit elastoplastischen Deformationen”,
K.-H. Lambertz, Dissertation, Oktober 1989

F 89/3 “Transientes Kriechen und Kriechbruch im Steinsalz”,
U. Heemann, Dissertation, November 1989

F 89/4 “Materialgesetze zum Verhalten von Betonkonstruktionen bei harten Stößen”,
E. Stein, P. Wriggers, T. Vu Van & T. Wedemeier, Dezember 1989

F 89/5 “Lineare Konstruktion und Anwendungen von Begleitmatrizen”,
C. Carstensen, Dissertation, Dezember 1989

F 90/1 “Zur Berechnung prismatischer Stahlbetonbalken mit verschiedenen Querschnittsformen für allgemeine Beanspruchungen”,
H. N. Lucero–Cimas, Dissertation, April 1990

F 90/2 “Zur Behandlung von Stoß- Kontaktproblemen mit Reibung unter Verwendung der Finite–Element–Methode”,
T. Vu Van, Dissertation, Juni 1990

F 90/3 “Netzadaption und Mehrgitterverfahren für die numerische Behandlung von Faltwerken”,
L. Plank, Dissertation, September 1990

F 90/4 “Beiträge zur Theorie und Numerik finiter inelastischer Deformationen”,
N. Müller–Hoeppe, Dissertation, Oktober 1990

F 90/5 “Beiträge zur Theorie und Numerik von Materialien mit innerer
Reibung am Beispiel des Werkstoffes Beton”,
T. Wedemeier, Dissertation, Oktober 1990

F 91/1 “Zur Behandlung von Stabilitätsproblemen der Elastostatik mit der Methode der Finiten Elemente”,
W. Wagner, Habilitation, April 1991

F 91/2 “Mehrgitterverfahren und Netzadaption für lineare und nichtlineare statische Finite–Elemente–Berechnungen von Flächentragwerken”,
W. Rust, Dissertation, Oktober 1991

F 91/3 “Finite Elemente Formulierungen im Trefftzschen Sinne für dreidimensionale anisotrop–elastische Faserverbundstrukturen”,
K. Peters, Dissertation, Dezember 1991

F 92/1 “Einspielen und dessen numerische Behandlung von Flächentragwerken aus ideal plastischem bzw. kinematisch verfestigendem Material”,
G. Zhang, Dissertation, Februar 1992

F 92/2 “Strukturoptimierung stabilitätsgefährdeter Systeme mittels analytischer Gradientenermittlung”,
A. Becker, Dissertation, April 1992

F 92/3 “Duale Methoden für nichtlineare Optimierungsprobleme in der Strukturmechanik”,
R. Mahnken, Dissertation, April 1992

F 93/1 “Kanonische Modelle multiplikativer Elasto–Plastizität. Thermodynamische Formulierung und numerische Implementation”,
C. Miehe, Habilitation, Dezember 1993

F 93/2 “Theorie und Numerik zur Berechnung und Optimierung von Strukturen aus isotropen, hyperelastischen Materialien”,
F.–J. Barthold, Dissertation, Dezember 1993

F 94/1 “Adaptive Verfeinerung von Finite-Element-Netzen für Stabilitätsprobleme von Flächentragwerken”,
E. Stein, B. Seifert, W. Rust, Forschungsbericht, Oktober 1994

F 95/1 “Adaptive Verfahren für die Formoptimierung von Flächentragwerken unter Berücksichtigung der CAD–FEM–Kopplung”,
A. Falk, Dissertation, Juni 1995

F 96/1 “Theorie und Numerik dünnwandiger Faserverbundstrukturen”,
F. Gruttmann, Habilitation, Januar 1996

F 96/2 “Zur Theorie und Numerik finiter elastoplastischer Deformationen von Schalenstrukturen”,
B. Seifert, Dissertation, März 1996

F 96/3 “Theoretische und algorithmische Konzepte zur phänomenologischen Beschreibung anisotropen Materialverhaltens”,
J. Schröder, Dissertation, März 1996

F 96/4 “Statische und dynamische Berechnungen von Schalen endlicher elastischer Deformationen mit gemischten finiten Elementen”,
P. Betsch, Dissertation, März 1996

F 96/5 “Kopplung von Finiten Elementen und Randelementen für ebene Elastoplastizität mit Implementierung auf Parallelrechnern”,
M. Kreienmeyer, Dissertation, März 1996

F 96/6 “Theorie und Numerik dimensions- und modelladaptiver Finite-Elemente-Methoden von Flächentragwerken”,
S. Ohnimus, Dissertation, Juni 1996

F 96/7 “Adaptive Finite Elemente Methoden für MIMD-Parallelrechner zur Behandlung von Strukturproblemen mit Anwendung auf Stabilitätsprobleme”,
O. Klaas, Dissertation, Juli 1996

F 96/8 “Institutsbericht 1971–1996 aus Anlaß des 25-jährigen Dienstjubiläums von Prof. Dr.-Ing. Dr.-Ing. E.h. Dr. h.c. mult. Erwin Stein, Dezember 1996

F 97/1 “Modellierung und Numerik duktiler kristalliner Werkstoffe”,
P. Steinmann, Habilitation, August 1997

F 97/2 “Formoptimierung in der Strukturdynamik”,
L. Meyer, Dissertation, September 1997

F 97/3 “Modellbildung und Numerik für Versagensprozesse in Gründungen von Caisonwellenbrechern”,
M. Lengnick, Dissertation, November 1997

F 98/1 “Adaptive gemischte finite Elemente in der nichtlinearen Elastostatik und deren Kopplung mit Randelementen”,
U. Brink, Dissertation, Februar 1998

F 98/2 “Theoretische und numerische Aspekte zur Parameteridentifikation und Modellierung bei metallischen Werkstoffen”,
R. Mahnken, Habilitation, Juli 1998

F 98/3 “Lokalisierung und Stabilität der Deformation wassergesättigter bindiger und granularer Böden”,
J. M. Panesso, Dissertation, August 1998

F 98/4 “Theoretische und numerische Methoden in der angewandten Mechanik mit Praxisbeispielen”,
R. Mahnken (Hrsg.), Festschrift anlässlich der Emeritierung von Prof. Dr.–Ing. Dr.–Ing. E.h. h.c. mult. Erwin Stein, November 1998

F 99/1 “Eine h-adaptive Finite–Element–Methode für elasto–plastische Schalenprobleme in unilateralem Kontakt”,
C.-S. Han, Dissertation, Juli 1999

F 00/1 “Ein diskontinuierliches Finite–Element–Modell für Lokalisierungsversagen in metallischen und granularen Materialien”,
C. Leppin, Dissertation, März 2000

F 00/2 “Untersuchungen von Strömungen in zeitlich veränderlichen Gebieten mit der Methode der Finiten Elemente”,
H. Braess, Dissertation, März 2000

F 00/3 “Theoretische und algorithmische Beiträge zur Berechnung von Faserverbundschalen”,
J. Tessmer, Dissertation, März 2000

F 00/4 “Theorie und Finite-Element-Methode für die Schädigungsbeschreibung in Beton und Stahlbeton”,
D. Tikhomirov, Dissertation, August 2000

F 01/1 “A C1 - continuous formulation for finite deformation contact”,
L. Krstulovic-Opara, Dissertation, Januar 2001

F 01/2 “Strain Localisation Analysis for Fully and Partially Saturated Geomaterials”,
H. Zhang, Dissertation, Januar 2001

F 01/3 “Meso-makromechanische Modellierung von Faserverbundwerkstoffen mit Schädigung”,
C. Döbert, Dissertation, April 2001

F 01/4 “Thermomechanische Modellierung gummiartiger Polymerstrukturen”,
S. Reese, Habilitation, April 2001

F 01/5 “Thermomechanisches Verhalten von Gummimaterialien während der Vulkanisation – Theorie und Numerik –”,
M. André, Dissertation, April 2001

F 01/6 “Adaptive FEM für elastoplastische Deformationen – Algorithmen und Visualisierung”,
M. Schmidt, Dissertation, Juni 2001

F 01/7 “Verteilte Algorithmen für h-, p- und d-adaptive Berechnungen in der nichtlinearen Strukturmechanik ”,
R. Niekamp, Dissertation, Juni 2001

F 01/8 “Theorie und Numerik zur Berechnung und Optimierung von Strukturen mit elastoplastischen Deformationen”,
K. Wiechmann, Dissertation, Juli 2001

F 01/9 “Direct Computation of Instability Points with Inequality Contraints using the Finite Element Method”,
H. Tschöpe, Dissertation, September 2001

F 01/10 “Theorie und Numerik residualer Fehlerschätzer für die Finite-Elemente-Methode unter Verwendung äquilibrierter Randspannungen”,
S. Ohnimus, Habilitation, September 2001

F 02/1 “Adaptive Algorithmen für thermo-mechanisch gekoppelte Kontaktprobleme”,
A. Rieger, Dissertation, August 2002

F 02/2 “Consistent coupling of shell- and beam-models for thermo-elastic problems”,
K. Chavan, Dissertation, September 2002

F 03/1 “Error-controlled adaptive finite element methods in large strain hyperelasticity and fracture mechanics”,
M. Rüter, Dissertation, Mai 2003

F 03/2 “Formulierung und Simulation der Kontaktvorgänge in der Baugrund-Tragwerks-Interaktion”,
A. Haraldsson, Dissertation, Juni 2003

F 03/3 “Concepts for Nonlinear Orthotropic Material Modeling with Applications to Membrane Structures”,
T. Raible, Dissertation, Juni 2003

F 04/1 “On Single- and Multi-Material arbitrary Lagrangian-Eulerian Approaches with Application to Micromechanical Problems at Finite Deformations”,
D. Freßmann, Dissertation, Oktober 2004

F 04/2 “Computational Homogenization of Microheterogeneous Materials at Finite Strains Including Damage”,
S. Löhnert, Dissertation, Oktober 2004

F 05/1 “Numerical Micro-Meso Modeling of Mechanosensation driven Osteonal Remodeling in Cortical Bone”,
C. Lenz, Dissertation, Juli 2005

F 05/2 “Mortar Type Methods Applied to Nonlinear Contact Mechanics”,
K.A. Fischer, Dissertation, Juli 2005

F 05/3 “Models, Algorithms and Software Concepts for Contact and Fragmentation in Computational Solid Mechanics”,
C. Hahn, Dissertation, November 2005

F 06/1 “Computational Homogenization of Concrete”,
S. Moftah, Dissertation, Januar 2006

F 06/2 “Reduction Methods in Finite Element Analysis of Nonlinear Structural Dynamics”,
H. Spiess, Dissertation, Februar 2006

F 06/3 “Theoretische und algorithmische Konzepte zur Beschreibung des beanspruchungsadaptiven Knochenwachstums”,
B. Ebbecke, Dissertation, März 2006

F 06/4 “Experimentelle Untersuchungen an elastomeren Werkstoffen”,
M. Dämgen, Dissertation, Dezember 2006

F 07/1 “Numerische Konzepte zur Behandlung inelastischer Effekte beim reibungsbehafteten Rollkontakt”,
M. Ziefle, Dissertation, Februar 2007

F 07/2 “Begleitbuch zur Leibniz-Ausstellung”,
Hrsg: E. Stein, P. Wriggers, 2007

F 07/3 “Modellierung und Simulation der hochfrequenten Dynamik rollender Reifen”,
M. Brinkmeier, Dissertation, Juni 2007

F 07/4 “Computational Homogenization of micro-structural Damage due to Frost in Hardened Cement Paste”,
M. Hain, Dissertation, Juli 2007

F 07/5 “Elektromechanisch gekoppelte Kontaktmodellierung auf Mikroebene”,
T. Helmich, Dissertation, August 2007

F 07/6 “Dreidimensionales Diskrete Elemente Modell für Superellipsoide”,
C. Lillie, Dissertation, Oktober 2007

F 07/7 “Adaptive Methods for Continuous and Discontinuous Damage Modeling in Fracturing Solids”,
S.H. Reese, Dissertation, Oktober 2007

F 08/1 “Student Projects of Micromechanics”,
Hrsg: U. Nackenhorst, August 2008

F 09/1 “Theory and Computation of Mono- and Poly- crystalline Cyclic Martensitic Phase Transformations”,
G. Sagar, Dissertation, August 2009

F 09/2 “Student projects of Micromechanics”,
D. Balzani and U. Nackenhorst, Course Volume, October 2009

F 09/3 “Multiscale Coupling based on the Quasicontinuum Framework, with Application to Contact Problems”,
W. Shan, Dissertation, November 2009

F 10/1 “A Multiscale Computational Approach for Microcrack Evolution in Cortical Bone and Related Mechanical Stimulation of Bone Cells”,
D. Kardas, Dissertation, September 2010

F 11/1 “Ein integrales Modellierungskonzept zur numerischen Simulation der Osseointegration und Langzeitstabilität von Endoprothesen”,
A. Lutz, Dissertation, Oktober 2011

F 12/1 “Ein physikalisch motiviertes Reifen-Fahrbahnmodell für die Gesamtfahrzeugsimulation”,
R. Chiarello, Dissertation, Februar 2012

F 13/1 “Thermomechanical Analysis of Tire Rubber Compounds in Rolling Contact”,
A. Suwannachit, Dissertation, September 2012

F 13/2 “Towards a Finite Element Model for Fluid Flow in the Human Hip Joint”,
K. Fietz, Dissertation, September 2013

F 14/1 “Micro-Mechanically Based Damage Analysis of Ultra High Performance Fibre Reinforced Concrete Structures with Uncertainties”,
A. Hürkamp, Dissertation, Dezember 2013

F 14/2 “Numerical Solution of High-Dimensional Fokker-Planck Equations with Discontinuous Galerkin Methods”,
F. Loerke, Dissertation, Dezember 2013

F 14/3 “Numerische Simulation probabilistischer Schädigungsmodelle mit der Stochastischen Finite Elemente Methode”,
P.-P. Jablonski, Dissertation, September 2014

F 15/1 “On a Finite Element Approach for the Solution of a mechanically Stimulated Biochemical Fracture Healing Model”,
A. Sapotnick, Dissertation, Februar 2015

F 15/2 “Stimulation of Elastic-Plastic Material Behavior with Uncertain Material Parameters. A Spectral Stochastic Finite Element method Approach”,
S. Fink, Dissertation, Februar 2015

F 15/3 “A Fully Micro-mechanically Motivated Material Law for Filled Elastome”,
O. Stegen, Dissertation, März 2015

F 16/1 “A modified adaptive harmony search algorithm approach on structural identification and damage detection”,
M. Jahjouh, Dissertation, Januar 2016

F 17/1 “Computational Simulation of Piezo-electrically Stimulated Bone Adaption Surrounding Activated Teeth Implants”,
A. Shirazibeheshtiha, Dissertation, Januar 2017

F 17/2 “A Constitutive Contact Model for Homogenized Tread-Road Interaction in Rolling Resistance Computations”,
R. Beyer, Dissertation, Februar 2017

F 17/3 “A Posteriori Error Estimates for Advanced Galerkin Methods”,
M.O. Rüter, Habilitation, November 2017

F 17/4 “Probabilistische Finite Element Modellierung des mechanischen Materialverhaltens von Salzgestein”,
M. Grehn, Dissertation, Dezember 2017

F 18/1 “Modeling and numerical simulation for the prediction of the fatigue strength of airsprings”,
N.K. Jha, Dissertation, März 2018

F 18/2 “A model reduction approach in space and time for fatigue damage simulation”,
M. Bhattacharyya, Dissertation, Mai 2018